ABSTRACT

Title of Thesis: ADVANCED OVERMODED CIRCUITS

FOR GYRO-AMPLIFIERS

Degree candidate: Yingyu Miao

Degree and year: Doctor of Philosophy, 2004

Dissertation directed by: Victor L. Granatstein
Professor
Institute for Research in Electronics and Applied Physics
Department of Electrical and Computer Engineering

Thomas M. Antonsen
Professor
Institute for Research in Electronics and Applied Physics
Department of Electrical and Computer Engineering
Department of Physics

To solve the narrow-bandwidth problem associated with cavity-related gyro-amplifiers, a new interaction circuit, containing clustered cavities is considered. In particular, the use of a cluster of cavities in frequency multiplying gyro-amplifiers is described. An analytical theory of a simple frequency multiplying device has been developed, and compared with numerical simulations using the Maryland Gyrotron Code (MAGY). The analytical results and MAGY code simulations are in good agreement. In the small signal regime, the bandwidth of a cluster-cavity device (with two cavities in the cluster) is twice that of a single cavity device, while both have the

same peak bunching. We also investigate the effect of coupling between the cavities of a cluster, and the performance of a three-cavity cluster.

A four-cavity cluster has been employed as a second harmonic buncher in a new type of Ka band, three-stage, harmonic-multiplying gyro-amplifier, which consists of a fundamental gyro-TWT input and second harmonic gyro-TWT output sections. This amplifier achieved 80 kW output power centered at 33.6 GHz with a bandwidth of 0.3 %, efficiency of 16 % and gain of 36 dB in the high order TE_{04} mode. MAGY simulations have been carried out and compared with the experimental data.

Mode competition is a principal issue in high-power gyrotron research and development. A vaned TE_{0n} mode converter has been proven to be effective in converting one designated TE_{0n} mode into another designated TE_{0m} mode while suppressing unwanted modes. A quasi-analytical theory has been developed to describe the electromagnetic field in the mode converter, and different modes have been calculated. By using a mode matching technique, the nonsymmetric field was incorporated in the MAGY code. This modification is a significant extension of MAGY capabilities. The results of scattering calculations for a vaned mode converter from the modified MAGY agree with the High Frequency Structure Simulator (HFSS) simulation to with 2%.

This thesis consists of the following parts: 1. a review of gyrotron oscillator and amplifier research and development; 2. the concept, theory and experimental study of cluster cavities; and, 3. a study of a vaned TE_{0n} mode converter. It is hoped that this research will improve the understanding of gyro-amplifiers using clustered cavities and/or TE_{0n} mode converter structures, and advance research on gyro-amplifiers.

ADVANCED OVERMODED CIRCUITS FOR GYRO-AMPLIFIERS

by

Yingyu Miao

Dissertation submitted to the Faculty of the Graduate School of the
University of Maryland, College Park in partial fulfillment
of the requirement for the degree of
Doctor of Philosophy
2004

Advisory Committee:

Professor Victor L. Granatstein, Chairman/Advisor
Professor Thomas M. Antonsen, /Co-Advisor
Professor Wes Lawson
Dr. Gregory S. Nusinovich
Professor Richard F. Ellis

ACKNOWLEDGMENTS

There are too many people to thank and acknowledge, so forgive me if I don't remember you all, or have enough space to include you.

Thank you students, faculty and staff of University of Maryland. I have learned so much from so many; these five years was a rewarding experience.

Thank you Dr. Granatstein for giving me the opportunity to continue my education and for your guidance.

Thank you Dr. Antonsen for all of your guidance, help and patience. I appreciate you more than words can say.

Thank you Dr. Guo for being my first co-advisor and introducing me to this field.

Thank you Dr. Vlasov, Dr. Nusinovich and Dr. Rodgers for your great help with my research.

Thank you Dr. Lawson and Ellis for serving on my defense committee.

Thank you my family for your unconditional support and love.

TABLE OF CONTENTS

LIST OF TABLES

LIST OF FIGURES

Chapter 1

Introduction

1.1 Gyrotron Research and Development

1.1.1 Gyrotron interaction mechanism

High power microwave tubes are devices which generate or amplify electromagnetic radiation in the frequency range of 0.3 GHz to 300 GHz (microwave and millimeter wave frequencies) at high peak and high average power level. Their development and technology [1]-[3] have been greatly advanced in the past decades, with parameters such as frequency extending to teraherz, peak power extending to gigawatts and average power extending to megawatts. However, all there parameters are not achieved in a single device. Application of high power microwaves include military radar, satellite, communications, industrial processing and plasma hearing [4].

Among the various kinds of microwave tubes, the conventional linear-beam tubes [5] are the most well known devices used for amplification and generation of energy at high power levels. The most known are klystron and traveling-wave tubes

(TWT's), and there are also several less well known devices, such as the extended interaction klystron and twystron hybrid amplifier. In the microwave frequency range (usually up to 30GHz), the conventional microwave devices (klystrons, traveling wave tubes, backward-oscillators and magnetrons) perform very well. However, as the operating frequency increases into the millimeter wavelength range, the power capability of conventional microwave tubes is severely limited by the scaling law that states the average radiation power P and operating frequency f are related by $P \sim f^{-5/2}$ [6]. Because of the small circuit size in linear-beam devices, thermal loading due to both beam interception and RF heating severely limits the peak and average power that can be achieved at millimeter-wave frequencies [7]. For example, the W-band coupled-cavity TWT amplifier, the conventional amplifier with the highest average power capability at millimeter-wave frequencies, is limited to approximately 5 kW peak and 500 W average output power [8]. Moreover, RF breakdown is a critical issue in conventional microwave tubes because the dimension of the interaction circuit becomes smaller when the operating frequency increases.

Thus, researchers have been vigorously exploring a new mechanism for high power radiation sources that can avoid the above limitations. Gyrotrons, which make use of the electron cyclotron resonance maser (ECRM) instability are one of the best candidates as a high power source in the millimeter wavelength range. In these devices, synchronism occurs between high-order modes of a smooth waveguide or cavity and the motion of electrons that spiral about a strong confining magnetic field. Due to the higher order mode operation, transverse circuit dimensions can be much larger than in fundamental mode circuits, often much larger

than a free-space wavelength. This is contrasted with linear-beam devices, where transverse circuit dimensions are typically 10% of a free-space wavelength for moderate beam voltage ($\leq$ 80 kV) normally used in millimeter-wave radar drivers. Correspondingly, restrictions dictated by the power dissipation in the circuit and by breakdown at the walls are not as severe in gyrotrons as in conventional microwave devices.

The concept of the electron cyclotron maser instability on which gyrotrons are based was first described in 1958-1959 [9]-[11], and was experimentally verified in a number of studies in the 1960's [12]-[14]. In the early 1970's, electron cyclotron maser experiments driven by intense, relativistic electron beams were reported with peak microwave output power as large as 1 GW in a single short pulse (~ 50 ns) [15-17]. A practical cyclotron maser in a microwave tube configuration, the gyrotron oscillator, was invented [18] and first developed in the former U.S.S.R. [19].

In 1972, the first successful development and application of a gyrotron oscillator power tube was made in the U.S.S.R, with a wavelength ~1 cm, output power ~40 kW in a 0.5-ms pulse [20]. The first U.S. gyrotron oscillator was developed at the Naval Research Laboratory (NRL) [21] and applied for the first time to plasma heating in a large tokamak, the ISX-B Tokamak at the Oak Ridge National Laboratory, in 1980 [22].

The name "gyrotron" was originally used by the Russians for a single cavity oscillator, now more specifically referred to as a gyromonotron. The configuration of a gyromonotron is sketched in Fig. 1.1 [19]. A magnetron injection gun produces an annulus of electrons that travel along the circuit spiraling around the lines of the
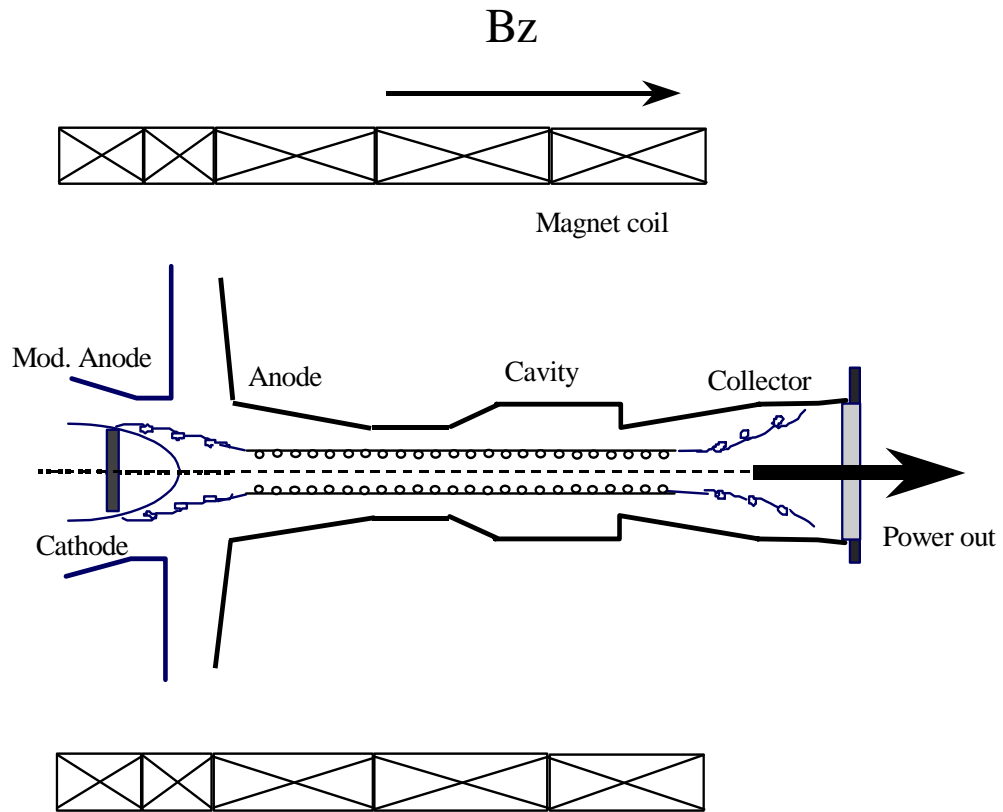
Figure 1. 1 Schematic of a gyrotron oscillator [19].

axial dc magnetic field. An important parameter of such an electron beam is the ratio of perpendicular velocity, $v_\perp$, to axial velocity, v_z. Usually $v_\perp / v_z$ is in the range of 1.0 to 2.0. The lower value gives greater stability against spurious oscillation while the high value gives greater efficiency.

A cross section of the electron beam is shown schematically in Fig. 1.2 [3] where the electrons are seen to initially have random phases in their electron orbits. Also shown in Fig. 1.2 is E_0, the azimuthal electric field of a TE_{0n} mode of the cylindrical gyrotron cavity. An electron such as #1 will be decelerated by the electric field and its mass will decrease (due to relativistic effects) leading to an increase in its cyclotron frequency as

$$\omega_c = \frac{eB_0}{m} = \frac{eB_0}{m_0}\sqrt{1-(v_z^2 + v_\perp^2)/c^2} \tag{1.1}$$

where m_0 is the electron rest mass. Similarly, an electron with a phase such as that of electron #2 will be accelerated by E_0 and its cyclotron frequency will decrease.

The modulation of the cyclotron frequencies can lead to phase bunching in the cyclotron orbits as shown in Fig. 1.3 [23]. If the electromagnetic (EM) wave is propagating axially at the same speed as the electrons and switches its polarity at the cyclotron frequency in the beam frame ($v_z = 0$), it can continuously decelerate the electrons and extract energy from their transverse velocity.

The process of phase bunching and energy extraction may be regarded as an interaction between a fast, transverse electric (TE), EM wave and the fast cyclotron wave of the electron beam. The dispersion curves of these two waves are plotted in

5
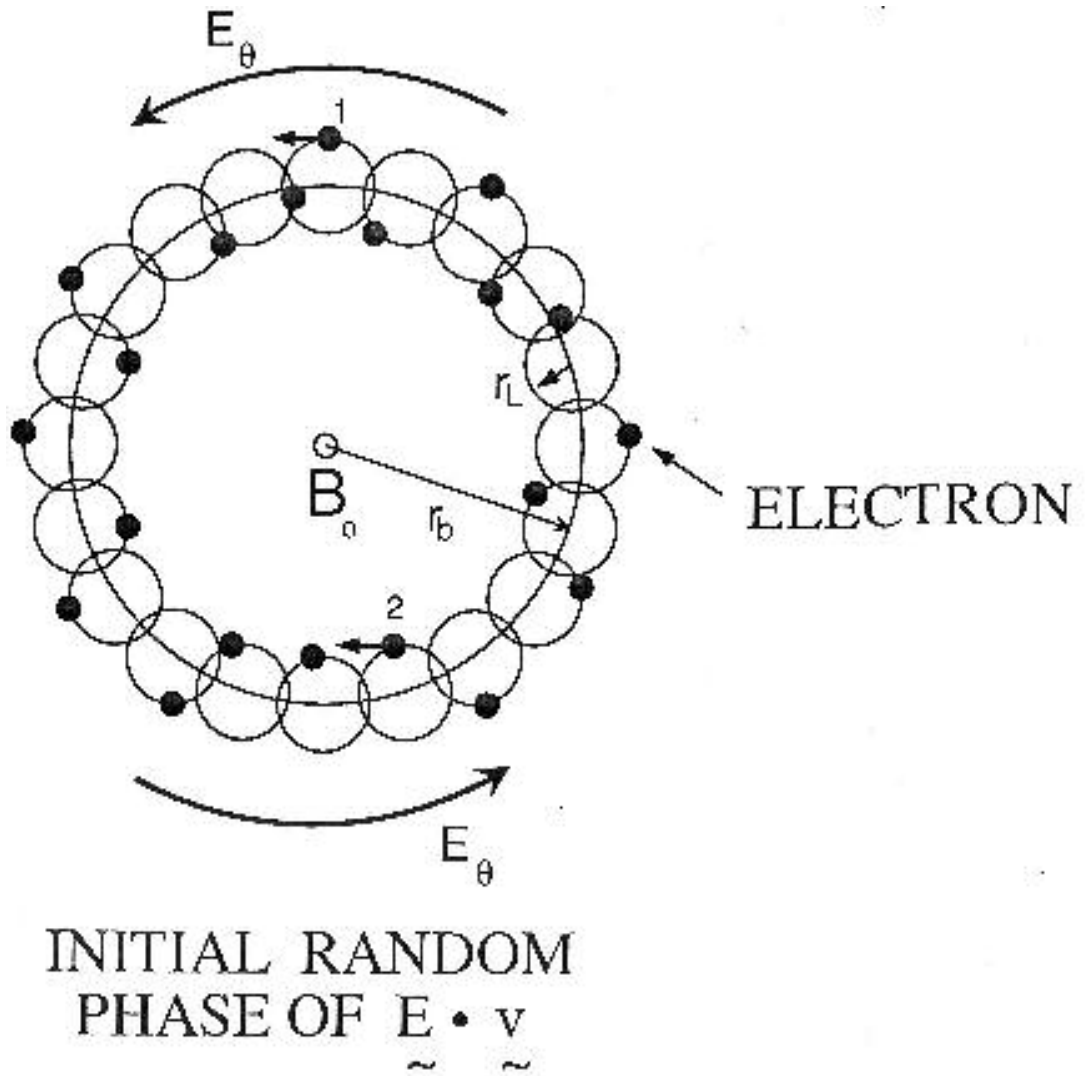
Figure 1. 2 Schematic of a cross section of the electron beam with initial random phase in their electron orbits [3].

(a)

(b)
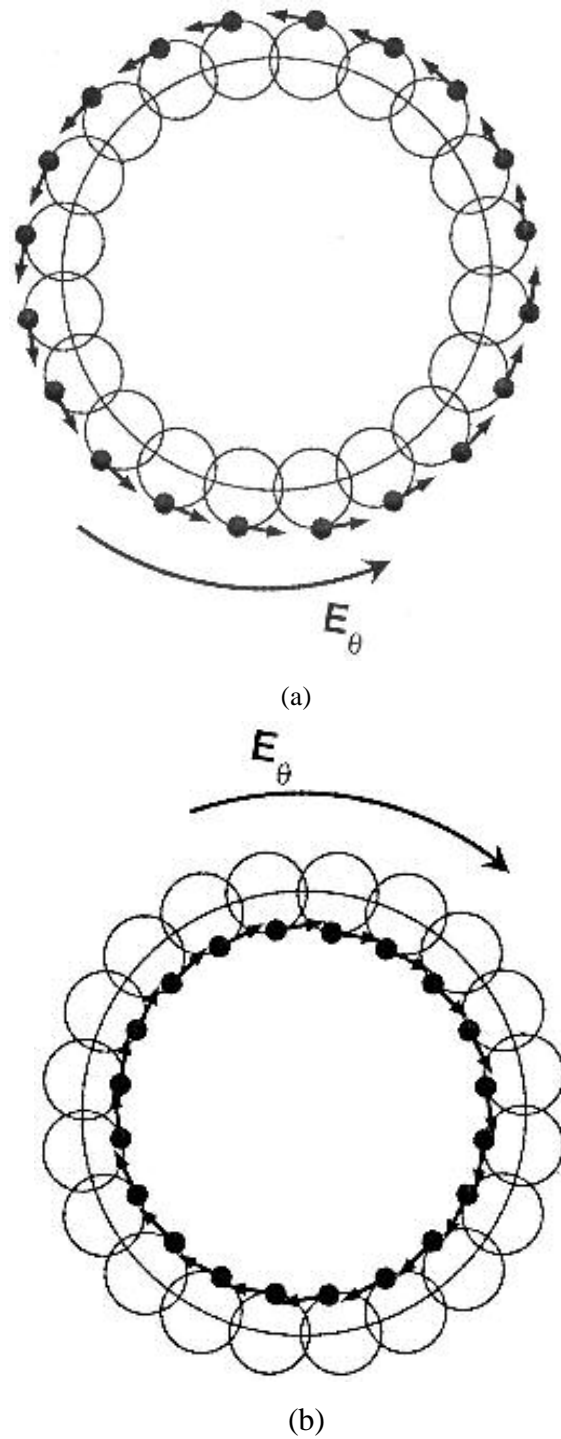
Figure 1. 3 Schematic illustration of electron phase bunching in RF electric field of TE symmetric wave [23].

Fig 1.4 [23]. The microwave frequency of the device and the magnitude of an applied dc magnetic field are intimately related by the synchronism condition

$$\omega \cong s\omega_c \pm k_z v_z \qquad (1.2)$$

The point of grazing interaction, where the two curves just touch, is the usual point of operation.

1.1.2 Development of gyrotron oscillators

Gyrotron oscillators operating near the cutoff frequency of a waveguide are quite efficient in converting the transverse kinetic energy of the spiraling electrons into microwave energy; however, the axial electron energy is not utilized. Overall, the output efficiency of a gyrotron oscillator is typically in the range of 30% to 40%. Gyrotron oscillators have now been applied in dozens of plasma-heating and current drive experiments in magnetic fusion research at frequencies ranging from 28-140 GHz and at power levels >100 kW, either continuous wave or in long pulses [24].

There is a different circuit arrangement known as the gyrotron backward-wave-oscillator, or gyro-BWO, which can provide a continuously tunable signal. The resonant cavity depicted in Fig. 1.1 would be replaced by a smooth wall waveguide, and oscillation would result from interaction between the forward-propagating fast cyclotron beam mode and the negative propagating waveguide mode. Fig. 1.4 shows the dispersion curves and the interaction points for the gyro-BWO.

A gyro-BWO with 7-kW output power and continuous tunability over the range of 27-32 GHz was studied at Naval Research Laboratory (NRL) [25]. A
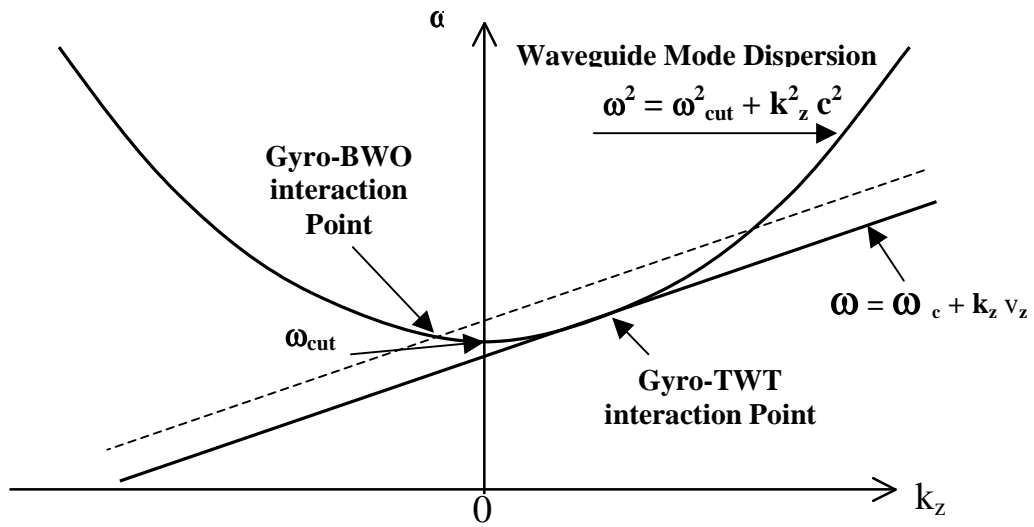
Figure 1. 4 Dispersion curves of waveguide mode and cyclotron beam mode showing point of interaction for gyromonotron oscillator and gyro-BWO [23].

gyro-BWO study, carried out at MIT, produced 1-kW peak output power with a tuning bandwidth of 6.5% [26]. The gyro-BWO study by Chu achieved Maximum power of 113 kW at ~19% efficiency [76]. As it turns out, avoiding gyro-BWO is a major challenge in the design of gyro-amplifiers. It is for this purpose that the mode converter to be studied in this thesis was developed.

1.1.3   Advantages of millimeter wave radar systems

For almost 50 years, it has been said that millimeter wave radar will be the new frontier or that "it is just around the corner," This has not been materialized since the technology at millimeter waves has been seriously lacking (especially high power). Stimulated mainly by radar applications, the interest in the development of high power, wideband millimeter wave source has been increased. Gyrotron amplifiers with peak power exceeding the state-of-the-art in conventional amplifiers have already been deployed in millimeter wave radar, where they provide narrow radiation beamwidth and wide absolute bandwidth permitting many benefits over conventional lower frequency systems [19]. Gyrotron amplifiers which exceed both the conventional peak and average power limits are being developed.

Millimeter wave radars are generally designed to take advantage of the atmospheric windows at frequencies of approximately 35 GHz and 94 GHz. However, these atmospheric windows disappear and there is generally increasing absorption with frequency when even modest levels of humidity are present, such as for propagation at low altitudes [27]. In these radar applications, such as shipboard fire control radar, where the radar is operating close to the horizon, the humidity is

generally high, and high power levels are required to achieve acceptable radar performance. Nevertheless, for ground or ship-based radars operating predominantly at angles close to zenith or for airborne radars, the atmospheric windows are present. In both cases, the higher power levels obtained from gyro-amplifiers provided increased performance over lower power amplifier technologies. For tracking radars, the narrow beamwidth obtained at millimeter-wave frequencies limit the difficulties associated with multipath propagation effects in the tracking of the targets close to the sea surface [28]. Considerable research on cloud physics has been carried out in recent years at millimeter-wave frequencies with extended interaction klystrons as RF source [29]. This work has been motivated by the need for improved heat-transfer models in the earth's atmosphere for the study of global warming. Application of gyro-amplifiers or gyro-oscillators to the study of clouds could have several advantages, including the ability to observe clouds at greater ranges and study of cloud tomography [30]. High-power, millimeter-wave radar is also of interest for ground-based space applications such as space debris detection [31] and asteroid tracking, also known as planetary defense. Additional defense and non-defense missions of importance for high-power, millimeter-wave radar include such missions as space object identification and planetary mapping studies by means of inverse synthetic aperture radar.

The gyro-amplifiers needed for radar applications must typically be capable of high average power operation with duty factors from 5% to 100%, depending on the type of radar. Generally, it is the average power rather than the peak power which is the measure of the capability of a coherent radar [32]. For high performance radar,

the features of high gain, high efficiency, low noise figure, compactness and light weight are also highly desirable in addition to high output and wide operating bandwidth.

1.1.4 Configuration and development of different gyro-amplifiers

The development of overmoded amplifiers is more difficult than in the oscillator case because they must be kept stable in the absence of a drive signal. Also, overmoded input couplers must be developed to inject the drive signal. Furthermore, performance parameters such as bandwidth, gain, phase stability, and noise become vitally important.

The circuits for various gyro-amplifier configurations are sketched in Fig. 1.5 [19]. In Fig. 1.5(a), the circuit for the gyro-TWT is shown as a smooth-wall waveguide. Electron phase bunching and EM wave amplitude both grow exponentially along the tube axis until saturation of the process occurs. Since the traveling waves can interact with an electron beam over a wide range of frequencies, the bandwidth is very large. But the efficiency is lower because of weaker interaction between the electron beam and the wave in the TWT circuit.

The gyro-TWT mechanism was first studied experimentally using an intense relativistic electron beam (IREB) by Granatstein *et al* [16]. Further studies in the cylindrical configuration led to the first operation of the gyro-TWT at the NRL [33]. Performances of these as well as subsequent experiments are summarized in Table 1.1. As remarked in the last column, each experiment represents a significant step toward the realization of the ultimate potential of the gyro-TWT. For comparison,

Sever

P_out_

P_in_

waveguide

(a)

cavity   **cavity**   **cavity**

P_out_

P_in_

(b)

cavity   **cavity**   **waveguide**

P_out_

P_in_

(c)

Extended
interaction cavity

waveguide   **cavity**

P_in_

P_out_

(d)
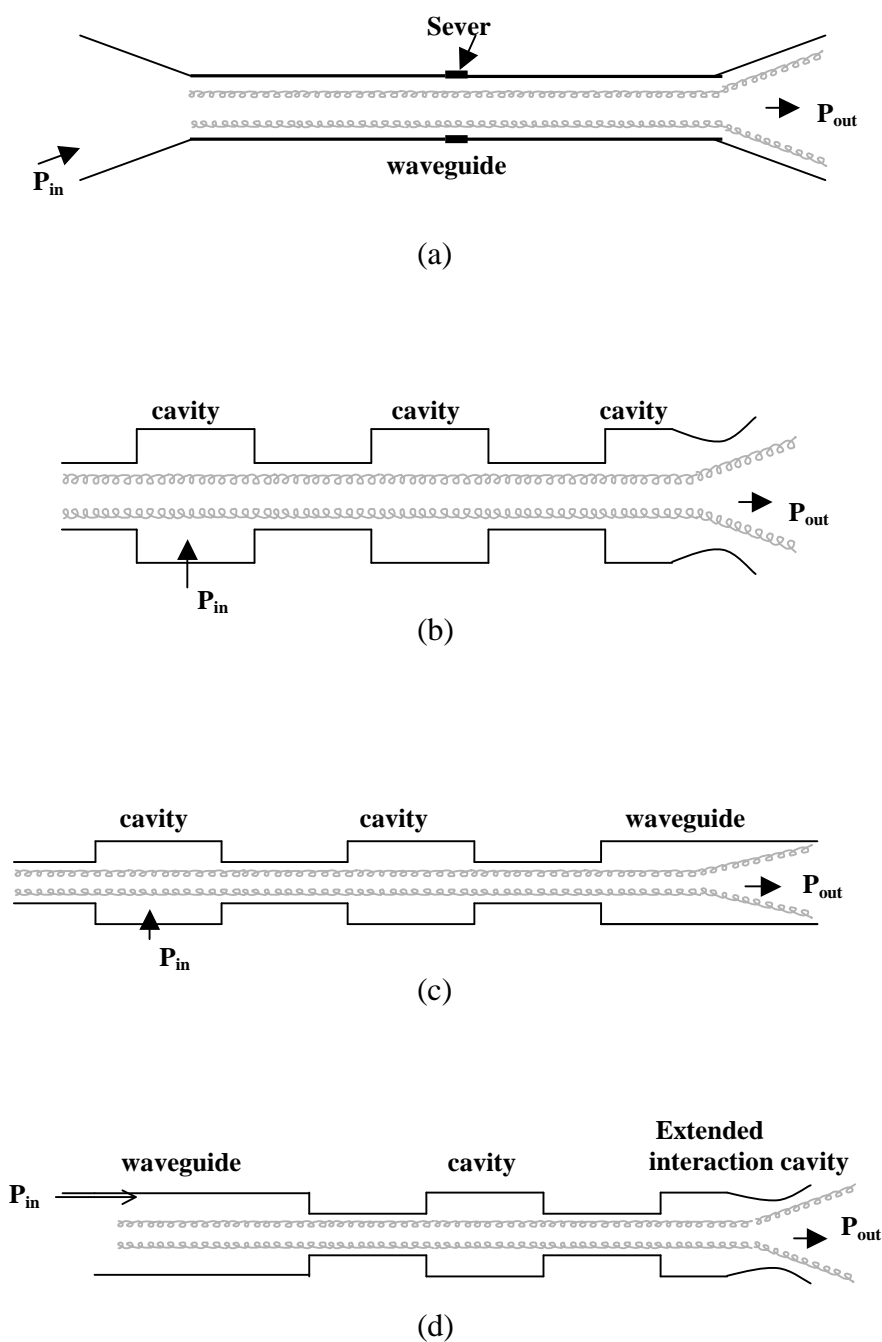
Figure 1. 5 Gyro-amplifier circuits: (a) gyro-TWT. (b) Three-cavity gyroklystron, (c) gyrotwystron, and (d) Phigtron [17].

13

Table 1. 1 Gyro-TWT Amplifier Experimental Results and State-of-the Art Coupled-Cavity TWT for Comparison.

Institute [reference] year	Clyclotron harmonic no/mode	V_b (kV)	Center frequency (GHz)	Peak power (kW)	Max. Duty (%)	Saturated gain (dB)	Saturated efficiency (%)	Saturated bandwidth 3dB (%)	Remarks
Varian/CPI [VTA 5701]	---	50	35	50	10	40	16	6	State-of-the-art Ka-band TWT
NRL [33], [34], 1979	1/ TE_{01}	70	35	16.6	low	20	7.8	1.5	First demonstration of gyro-TWT
NTHU, Taiwan [35],[36], 1998	1/ TE_{11}	100	35	93	low	70	26.5	8.6	Demonstration of an ultra high gain scheme employing distributed wall losses
UCLA and UC Davis [37],[38], 1995	2/ TE_{21}	80	15.7	207	low	16	13	2.1	Demonstration of stability and high power with harmonic interaction
NRL [39], [40],1991	1/ TE_{10} (rectangular)	33	34	---	low	20 (linear)	---	33 (linear)	Record bandwidth achieved with a single-stage tapered circuit
NRL [41], 1995	1/ TE_{10}	33	35	8	low	25	16	20	Broadband two-stage tapered circuit
UMCP [42], 2000	1/ TE_{02} 2/ TE_{03}	50	33	180	low	27	12 (linear)	3.2	First demonstration of harmonic-multiplying Gyro-TWT
NRL [43], 2002	1/ TE_{01}	72	34	137	low	47	17	3.3	Using a new type of ceramic loading

Table 1. 2 Gyroklystron Amplifier Experimental Results and State-of-the Art Coupled-Cavity TWT for Comparison

Institute [reference] year	Clyclotron harmonic no/mode	V_b (kV)	Center frequency (GHz)	Peak power (kW)	Max. Duty (%)	Gain (dB)	Efficiency (%)	Bandwidth 3dB (%)	Remarks
VTW-5795 Coupled Cavity TWT, CPI [44-45]	---	49.5	95	5	10	50	5	1.1	State-of-the-art Ka-band TWT
IAP/Tory, Russia [46]	2 cavities 1/ TE_{021}	75	35	750	0.05	20	24	0.6	Research tube, IAP 100µs pluses, 5 Hz
IAP/Tory, Russia [46]	3 cavities 1/ TE_{011}	55	35	250	---	40	35	1.4	Tory, 100 to 400µs pluses at < 400 Hz
IAP, Russia [47]	2 cavities 2/ TE_{021}	60	35.1	125	0.05	15	15	0.1	Power limited by TE_{011} mode at n=1.
IAP/Istok, Russia [48]	4 cavities 1/ TE_{011}	22	91.6	2.5	100	30	25	0.33	Duty 100%, CW output
NRL [49]	4 cavities 1/ TE_{011}	55	93.2	60	13	28	24	0.69	Applied to NRL WARLOC radar
NRL [50]	4 cavities 1/ TE_{011}	66	93.8	90	11	32	33	0.45	Demonstrate record average output power
NRL [50]	5 cavities 1/ TE_{011}	55	93.8	100	10	33	31	0.75	High average power and improved bandwidth

performance characteristics of a state-of-the-art conventional Ka-band-TWT are also listed in the first row of Table 1.1. The group at the National Tsing Hua University (NTHU), Taiwan, systematically studied the fundamental gyro-TWT issues, such as mode competition and oscillation suppression, which led to the demonstration of an ultra high gain scheme that provided zero-drive stability at 70 dB saturation gain (see Table 1.1) [35],[36]. Gyro-TWT's have also operated at the second harmonic of the cyclotron frequency with 200 kW of peak output power achieved at 15.9 GHz in a study at the University of California, Davis [37].

The NRL launched a research effort studying the tapered gyro-TWT. Operated as a reflection amplifier, a single-stage device produced a record bandwidth of 33% in the small signal regime. A subsequent experiment, which employed an innovative two-stage circuit, improved gain, efficiency, and saturated output power (see Table 1.1) over that single-stage case, but with reduced bandwidth.

The University of Maryland, College Park (UMCP), group has been conducting research on a two-stage frequency-multiplying gyro-TWT, and peak power of 180 kW, gain of 27 dB and bandwidth of 3.2% were achieved. The output power is in the TE_{03} mode, which is the highest obtained mode in any gyro-amplifier. The details of this tube will be discussed in the following section.

Recently, a gyro-TWT experiment with a ceramic loaded interaction region was conducted in NRL [43], and a peak power of 137kW, gain of 47.0 dB and bandwidth of 3.3% were measured. So far, all the gyro-TWT experiments were conducted with low duty cycle.

The circuit for a three-cavity gyroklystron is sketched in Fig. 1.5(b). The gyroklystron consists of resonant cavities separated by drift spaces. In a two-cavity gyroklystron, the electrons are energy modulated by the input EM field in the first cavity; they ballistically bunch in phase in their cyclotron orbits in the drift space; the phase-bunched electrons transfer their transverse energy to an excited EM field in the output cavity. Intermediate cavities and additional drift spaces may be added to enhance gain or, if they are stagger-tuned, to enhance bandwidth. Gyroklystrons are characterized by larger efficiency and higher power at reduced bandwidth compared with gyro-TWTs.

A considerable amount of work on gyroklystron amplifiers was carried out by researchers in the Institute of Applied Physics (IAP) in Russia. Performance of those devices is listed in Table 1.2, as well as the state-of-the-art 95 GHz coupled cavity TWT from Communication & Power Industrials (CPI) for comparison. 35 GHz gyroklystrons were developed and reportedly employed in a radar system in the U.S.S.R; these gyroklystrons have two TE_{02} cavities and provide a gain of 20 dB and peak output power of 750 kW. Another 3-cavity, TE_{01} gyroklystron has a smaller output power (250 kW) but larger gain (20 dB) and bandwidth. In a device operating at the second harmonic in the TE_{02} mode, up to 125 kW was obtained. The performance of a 95 GHz 4-cavity TE_{01} gyroklystron developed at NRL was similar to a Russian 4-cavity gyroklystron [48] except that the bandwidth was increase by a factor of ~2 [49]. Two of these gyroklystrons have been used to drive the NRL WARLOC [51] (W-band Advanced Radar for Low Observable Control) radar, which is being developed as a transportable, land- and sea-based system, using quasi-

optical transmission line and duplexer components, a Cassegrain antenna, and associated receive and signal processor subsysterms. The WARLOC radar is the only radar system driven by gyro-amplifiers in the USA. As previously we mentioned, the capability of a coherent radar is generally measured by the average power rather than the peak power. For this reason, recently, the NRL group focused their development efforts on high-average power gyro-amplifiers. Two high-average power amplifiers were built and tested [50]. The first one achieved 10.1 kW average output power at 33% efficiency in the TE_{01} mode at 93.8 GHz with bandwidth of 420 MHz and gain of 32 dB. The second one was designed for improved bandwidth of 700 MHz. The details of those power amplifiers' performance are listed in Table 1.2.

The gyrotwystron, shown in Fig. 1.5(c), is a combination of a gyroklystron bunching section and a gyro-TWT output section. With this combination, the low gain of the TWT section is offset by the gain response of the stagger-tuned gyroklystron driver section. The overall results can be higher gain than a gyro-TWT and wider bandwidth than a gyroklystron. An initial gyrotwystron experiment [52] at 4.5 GHz extended small signal bandwidth from 0.41% to 1%, compared with a similar gyroklystron [53], while not significantly sacrificing efficiency or gain.

The phigtron [54], [55] in the form of an inverted gyrotwystron, has been studied at UMCP. It uses a gyro-TWT input section, a gyroklystron-like cavity as intermediate buncher, and extended interaction cavity as output section. It achieved 30 dB gain, 0.7% bandwidth and 720 kW peak output power in Ka band. Of special interest was the fact that the phigtron operated with input at the fundamental

cyclotron frequency in the TE_{02} mode and with output at the second harmonic in the TE_{03} mode. Details of the phigtron will be discussed in Section 1.2.

1.2 Frequency-Doubling   Second-Harmonic   Gyro-Amplifiers Developed at UMCP

1.2.1   The advantages of frequency-multiplying gyro-amplifiers

There is considerable interest in enhancing the capabilities of military radars to achieve longer range and finer resolution for such applications as defense against sea-skimming missiles. Enhanced capability could be achieved by extending radar frequencies to the millimeter wave range while maintaining the power at the high levels achieved in radar systems at lower microwave frequencies. Progress along these lines has been made by developing gyroklystron amplifiers to replace the ubiquitous linear beam klystrons for driving high-power radar. For gyrotron amplifiers, it is very attractive to consider the possibility of frequency-multiplying second-harmonic operation for the following reasons:

With any gyrotron operating a higher harmonic of the cyclotron frequency, the required magnetic field can be reduced by the harmonic factor, s, compared with gyrotrons operating at the fundamental cyclotron frequency, making gyro-devices compatible with modern permanent magnet technology up to operating frequencies of approximately s × 15 GHz. So the magnet system can be much more compact.

In addition, frequency multiplication enables a device with input signal at

centimeter wave frequencies and output in the millimeter wave band. The lower frequency drive sources are more ready available and less expensive.

Also, lower order mode operation makes the input couple easier to realize.

It is expected that the above unique features of frequency multiplying gyro-amplifiers will lead to an advance in coherent millimeter wave source capabilities, and will be attractive for such applications as millimeter wave radar, particle accelerators, space communication, and electronic warfare.

1.2.2 Harmonic-multiplying gyro-amplifier research at UMCP

Two frequency-doubling, harmonic-multiplying, gyro-amplifiers with Ka-band output frequency were experimentally and theoretically studied at UMCP. Their performance advances the state-of-the-art of the gyrotron family.

The three-stage phase-coherent harmonic-multiplying phigtron [54], in the form of the inverted gyrotwystron, is sketched in Fig. 1.6. The phigtron, operating in a 1-2-2 harmonic-multiplying mechanism, is composed of a Ku band fundamental (s=1) TE_{02} gyro-TWT followed by a long drift space as input stage and a Ka band extended interaction cavity 2nd harmonic (s=2) TE_{03} gyroklystron as output stage separated by a cavity buncher. It can operate in a wide band state, a high efficiency state, or a high power state. In the wide band state, frequency doubling amplifier peak power of 324kW was achieved in the TE_{03} mode with a bandwidth about 0.6%, gain of 30dB and efficiency of 30% at a frequency of approximately 33.75GHz. In
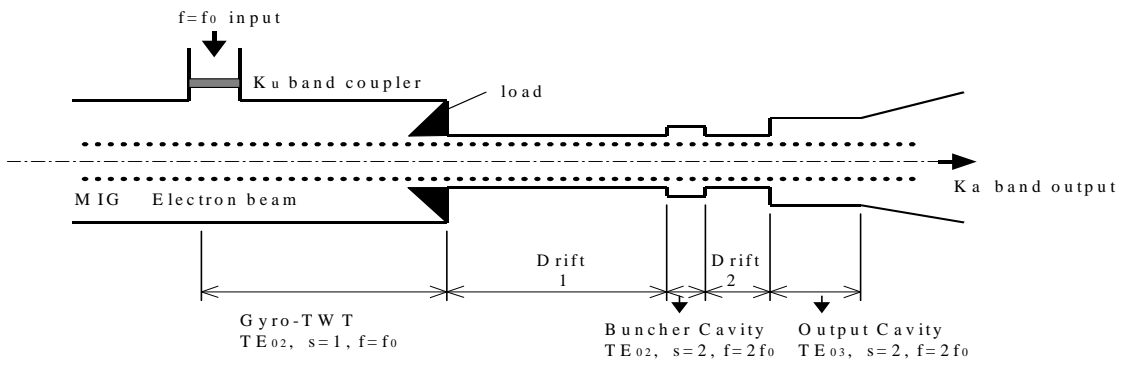
Figure 1. 6 Schematic of a three-stage phigtron.

the high efficiency state, peak power 420 kW was achieved in the TE_{03} mode with a bandwidth about 0.3%, gain of 30dB and efficiency of 35% at frequencies near 33.68 GHz. In the high power state, a stable amplifier operating state with efficiency 30.7% can be achieved at beam voltage 52kV and beam current 45A; peak power of 720kW is measured. The phigtron shows higher gain-bandwidth product and comparable power capacity compared with Ka-band higher-order-mode gyroklystrons.

The second type of device was a multi-stage traveling wave amplifier which allows developers to realize high gain of the total device while keeping the length of each stage shorter than the start-oscillation length of the backward wave instabilities, thus providing stable operation even in the absence of drive power (zero-drive stable regime). A two-stage harmonic multiplying gyro-TWT amplifier [42] has been demonstrated for the first time in UMCP. The schematic of the two-stage, harmonic-doubling gyro-TWT is shown in Fig 1.7. It consists a Ku band fundamental (s=1) TE_{02} gyro-TWT as input stage and Ka band 2nd harmonic (s=2) TE_{03} gyro-TWT as output stage; the input and output stages are separated by a radiation free drift section. It has achieved an output peak power of 126kW and 3 dB bandwidth of 3.2% with the input frequency ranging from 16 GHz to 16.8 GHz, and output frequency ranging from 32 GHz to 33.6 GHz. A gain of 28 dB and 12 % efficiency has also been achieved. The highest output peak power was more than 180 kW. Performance was limited by available input power. Nevertheless, the above figures exceed in some respects the performance of previous second harmonic gyro-TWT amplifiers.

(Gyro-TWT prebunching) (Ballistic Bunching) (Gyro-TWT energy extraction)
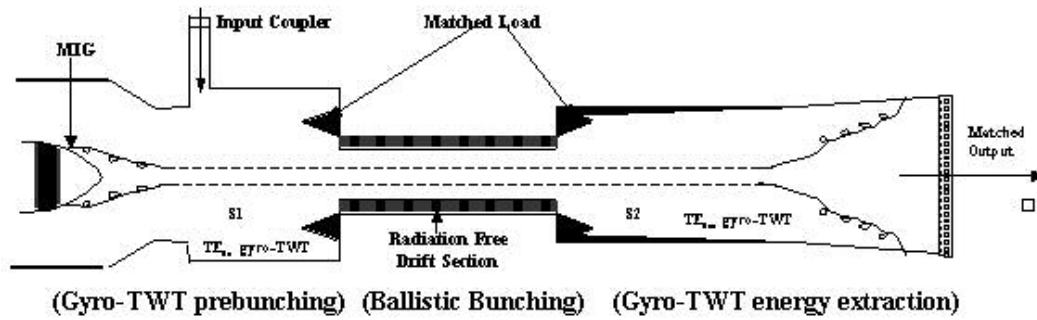
UMCP Gyro-TWT	Frequency	Efficiency	Peak Power	Gain	Band-width	Output Mode	Harmonic Number
Ka output, Ku input	12%	180KW	27dB	3.2%	TE_{03}	2nd

Figure 1. 7 Schematic of a two-stage harmonic-multiplying Gyro-TWT.

Both gyro-amplifiers employ a mode selective input coupler and mode-selctive interaction circuits to effectively suppress spurious mode competition and obtain stable high order mode harmonic operation.

1.3 Motivation and Goals for Development of Advanced Gyrotron Circuit Structures

1.3.1 Cluster-cavity structure

Advanced high-resolution imaging radar applications require a stable, high power (both in peak and average), millimeter-wave, coherent source. Recent radar development has focused on narrowband (< 1 GHz) gyroklystron operating in W-band and generating peak RF powers up to 100 kW. Once this technology is successfully demonstrated, more versatile tubes operating at higher power and bandwidth will be required. This will include sources with large bandwidth up to 1-5 GHz [56]; if a gyrotron is to be fielded as a radar, bandwidth is directly translated into range resolution. For a radar with constant frequency and pulse time T, the range resolution is $\Delta R = cT/2$. A pulse of length T has frequency bandwidth of $\Delta f = T^{-1}$, so the range resolution of the radar can also be expressed as $\Delta R = c/2\Delta f$, the conventional expression relating range to frequency bandwidth. If the radar pulse has bandwidth Δf and pulse time T unrelated to Δf (but of course larger than $1/\Delta f$), for optimum processing of the returned signal, the range resolution is still given

by $\Delta R = c / 2\Delta f$ [30]. The existing gyroklystron amplifiers can only acquire a bandwidth limited to the range of 0.1 ~ 1.4% (see Table 1.1). For gyroklystrons, bandwidth is a synthesized gain-frequency response of beam wave interaction in the input circuit, staggered intermediate cavities and output cavity. To realize 5 % bandwidth, simple cavity gyroklystrons are not suitable because their bandwidth results from two sequential processes (viz. beam bunching and output energy extraction), and each is restricted by cavity Q which must be sufficiently high for good efficiency and gain. Thus, the cavity Q's are ~100, and the bandwidth is less than 1%. Even though, with stagger-tuning, the bandwidth of gyroklystron can be broadened to some extent.

The phigtron achieved 0.7% bandwidth, but further enhancement of the bandwidth is limited by the use of a single gyroklystron-like cavity as buncher.

The two-stage harmonic-multiplying gyro-TWT developed at UMCP provides wider bandwidth of 3.2% but lower peak power of 180 kW. The predicted saturation efficiency is 20%. One reason for this lower efficiency is the lack of optimum bunching at the second harmonic of the electron cyclotron frequency.

Given the above background description of gyrotron research and development, a new gyro-device interaction circuit, the cluster-cavity circuit, is proposed, theoretically studied, modeled and built.

The clustered-cavity concept for gyro-amplifiers was presented by H. Guo *et al* for the first time at the HPM teleconference on Mar. 20, 2000 [57]. It should be noted that the transverse electric (TE) clustered-cavity has a counterpart in conventional high power microwave tubes; viz., Robert Symons' clustered-cavity,

which operates with a transverse magnetic (TM) mode in the clustered-cavity klystron [58]. Also, electron bunching occurs in the azimuthal direction in the TE clustered-cavity gyro-amplifiers rather than in the axial direction as in clustered-cavity klystron. It is anticipated that the cluster-cavity approach would improve the bandwidth of all cavity related gyro-amplifiers such as gyroklystrons, gyrotwystrons, and inverted gyrotwystrons (phigtrons).

1.3.2   The TE_{0n} mode-converter

Mode competition constitutes the principal issue in gyrotron research and development, and methods of controlling wanted modes and suppressing unwanted modes need to be investigated. The electron beam employed in the gyrotron possesses a transverse motion at the electron cyclotron frequency, which allows the beam to selectively interact with a high-order waveguide mode at a high cyclotron harmonic by properly matching the resonance conditions. However, the additional degree of freedom provided by the multitude of cyclotron harmonics can also generate numerous spurious oscillations. Fig. 1.8 [59] plots the ω - k_z diagram of TE_{11} and TE_{21} waveguide modes (for a waveguide radius of 0.27 cm) and the fundamental (s = 1) and second (s = 2) cyclotron harmonic beam-wave resonance lines. As is well understood, interactions in the backward wave region (points 1 and 2) are sources of absolute instabilities (oscillation due to internal feedback), whereas those in the forward wave region (points 3, 4, and 5) are normally, but not always,
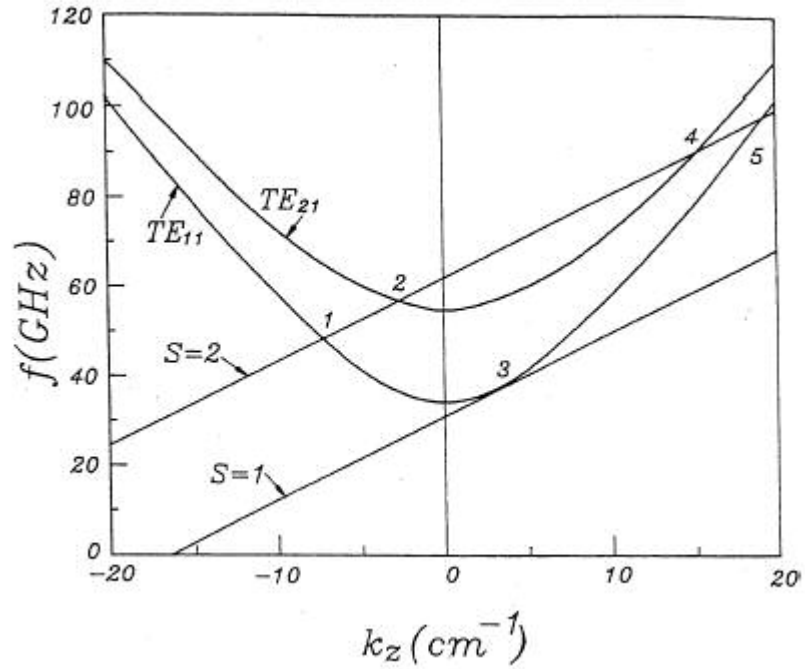
Figure 1. 8 ω- k_z diagram of a fundamental harmonic gyro-TWT operating in the TE$_{11}$ mode (point 3). Other possible convective instabilities (points 4 and 5) and absolute instabilities (points 1 and 2) are also indicated [59].

convective instabilities useful in amplifiers. The gyro-TWT is a complicated case because it exploits a convective instability near the cutoff frequency (e.g. point 3) which can turn into an absolute spectrum extending into the backward wave region. These various absolute instabilities can easily be the dominant sources of oscillations in an unsevered interaction structure. For example, in a fundamental harmonic gyro-TWT operating at the lowest order waveguide mode (points 3 in Fig. 1.8), a second harmonic absolute instability (points 2 in Fig.1.8), has been observed [60] at beam current as low as 0.1 A. The instability was shown to compete with and eventually be suppressed by the amplified wave, but linearity was affected at low drive powers.

Feedback due to reflection at the input-output couplers and structural non-uniformities presents a different source of oscillations (referred to as reflective oscillation) in the high-gain regime. Even when the gain is kept below the oscillation threshold, reflective feedback can still cause ripples in the gain and output power spectra.

However, the advanced millimeter wave radar required high power (both peak and average) gyrotrons as drive sources. Gyrotrons operating at high frequency and power require the use of a high-order cavity mode to allow for an increased circuit size which lowers ohmic losses on the wall to acceptable levels. A gyrotron experiencing severe mode competition may oscillate in an unwanted mode, which might significantly lower the gain and efficiency of the operating mode. Also, for radar application, the presence of spurious modes can result in unnecessary sidelobes of radiated pulses and inadequate duplexer performance.

The harmonic-multiplying gyro-amplifiers [42], [55] developed at UMCP successfully operated in an unprecedented TE_{03} mode in its output circuit, because both gyro-amplifiers employed a mode selective interaction circuits to effectively suppress spurious mode competition and obtain stable high order mode harmonic operation. Specifically, they employ a vaned mode converter/filter structure in the circuits. The vaned TE_{0n} mode-converter has been proved to be effective at converting one designated TE_{0n} mode into another designated TE_{0m} mode while suppressing unwanted modes.

Detailed and accurate simulations of the interaction between the EM fields and the electron beam in vacuum electron devices are essential to predict their performance. The prediction capabilities are critical to the design and development of future devices. In order to meet such requirements, the self-consistent, time-dependent, quasi two and half dimensional gyrotron simulation code MAGY [61] code was developed at UMCP and NRL. In contrast to the finite-difference-time-domain particle-in-cell (PIC) approach, MAGY employs a reduced description approach in which the EM fields are described by superposition of the waveguide TE and TM eigenmodes. Furthermore the temporal evolution of the EM complex field amplitudes and of the electron beam are assumed to be slow relative to the radio frequency period, hence, allowing for averaging over time scales on the order of the RF period. The combination of fast time-scale averaging and the reduced description RF fields substantially reduces the required computational resources compared with that required by PIC codes. However, unlike other reduced description codes, MAGY has not incorporated restricting assumption on the physics involved and,

thus, does not compromise the fidelity of the results. For instance, in MAGY, the RF field profiles, rather than being restricted to a fixed from, freely evolve in response to the interaction with the electron beam. This capability is achieved via a novel formulation of the generalized telegrapher's equations, together with the fast time-scale averaging of the fully relativistic electron equations of motion, which provides for multimode (TE and TM) coupling in arbitrary wall radius profiles, especially at radial step discontinuities. MAGY has been found to be useful in interpreting experiments and designing devices. Results from MAGY simulations provided physical insight into observed performance values of a 140 GHz gyrotron oscillator operating in the $TE_{16,2}$ mode [62]. MAGY is also used to investigate three different issues related to the operation of gyroklystron amplifiers: the effect of window reflection on the properties of the output waves, higher order mode excitation in nonlinear output tapers, and excitation in cutoff drift section [63]. Recently, MAGY has been used to design the W-band high average power gyroklystrons [50] and the ceramic loaded gyro-TWT [43] at NRL, and the detailed performance of those devices are listed in Table 1.1 and 1.2.

The field in MAGY is represented as a superposition of TE and TM modes of a waveguide of circular cross-section. This representation prevented simulation of devices with nonsymmetric structures such as the vaned mode converter/filter structure. Our research here is aimed at modifying MAGY to allow for such simulation, which will help us better understand the EM behavior in the mode converter/filter structure in the presence of an electron beam. It will enable the future design of gyro-amplifiers employing such structures.

Chapter 2

Clustered Cavities for Harmonic-Multiplying Gyro-Amplifiers

2.1 History and Concept

The original cluster-cavity concept was proposed by R. S. Symons in the early 1980s [64]. The conventional cluster-cavity klystron successfully obtained wideband and ultradwideband performance. At that time, the experiment successfully showed doubling of bandwidth from 6.5% to 12.8% [65] in an interaction circuit length of only 70 cm, maintaining the original tube's outside envelope [66]. Later studies focused on designs for an ultralwideband (bandwidth in the range of 30% to 40%) klystron by replacing individual intermediate cavities with triplets, in longer klystrons [67].

The cluster-cavity klystron is shown in Fig 2.1 [65]. In the cluster-cavity klystron, the individual intermediate cavities of a staggered-tuned multicavity klystron are replaced by pairs or triplets. Each cavity in the pair or triplet has, in addition, resistive loading in the cavity, to lower its Q to one-half or one-third respectively of the Q of the single cavity they replace. The cavities in the multiplet are closely adjacent. The ultrawideband clustered-cavity klystron has demonstrated a bandwidth in excess of 30%.

Replacing single cavities with clustered cavities in gyroklystrons (and other cavity-related gyro-amplifier interaction circuits) likely results in similar bandwidth-gain characteristics as cluster-cavity klystrons.
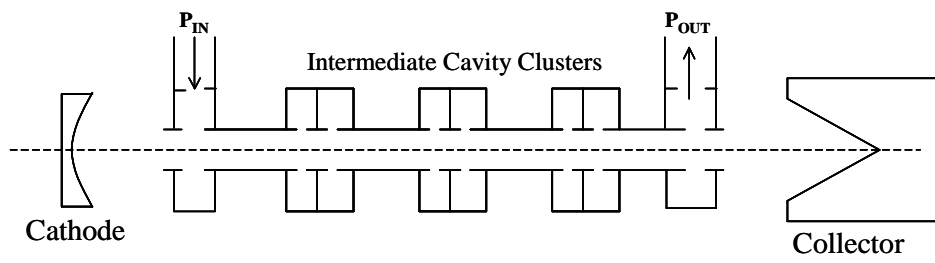
Figure 2. 1 Schematic of a conventional cluster-cavity klystron [65].

The diagram of a cluster-cavity device is shown in Fig. 2.2. Bunching is accomplished by two or more short cavities that are clustered together. The spacing of the gaps of the individual sub-cavities in each cluster is as close as possible without producing significant coupling between adjacent cavities. The resonant frequencies of cavities in a cluster can be the same or different. If they are different, frequency bands of adjacent cavities should overlap.

A simple way of explaining the improved bandwidth is to consider the case where all the cavities in the cluster are tuned to the same frequency and are excited by the same RF current. We can look at this concept from the circuit point of view. In the small signal regime, a single cavity can be represented by the lumped-parameter resonant circuit shown in Fig. 2.3a. The voltage across the circuit V_s is

$$V_s = I \cdot \sqrt{\frac{L}{C}} \cdot \frac{Q_s}{1 - i2Q_s(\omega - \omega_{res})/\omega_{res}}, \qquad (2.1)$$

where Q_s is the circuit Q factor, ω_{res} is the circuit resonant frequency, and $(L/C)^{1/2}$ is an impedance determined by the size and shape of the cavity, the so called R/Q for the cavity. Normally, to increase the bandwidth, we should lower the quality factor, but this also has the effect of reducing the bunching voltage for a given current.

For m clustered cavities (the lumped-parameter resonant circuit diagram is shown in Fig. 2.3b for the case $m = 2$), the cavity voltages add in series, yielding a bunching voltage V_c

$$V_c = I \cdot \sqrt{\frac{L}{C}} \cdot \frac{m \cdot Q_c}{1 - i2Q_c(\omega - \omega_{res})/\omega_{res}}, \qquad (2.2)$$

where Q_c is the circuit Q factor for a single cavity in the cluster.

P_{in}

f_0

(a)

f_1

(b)

f_1 f_2 f_3 f_4

(c)
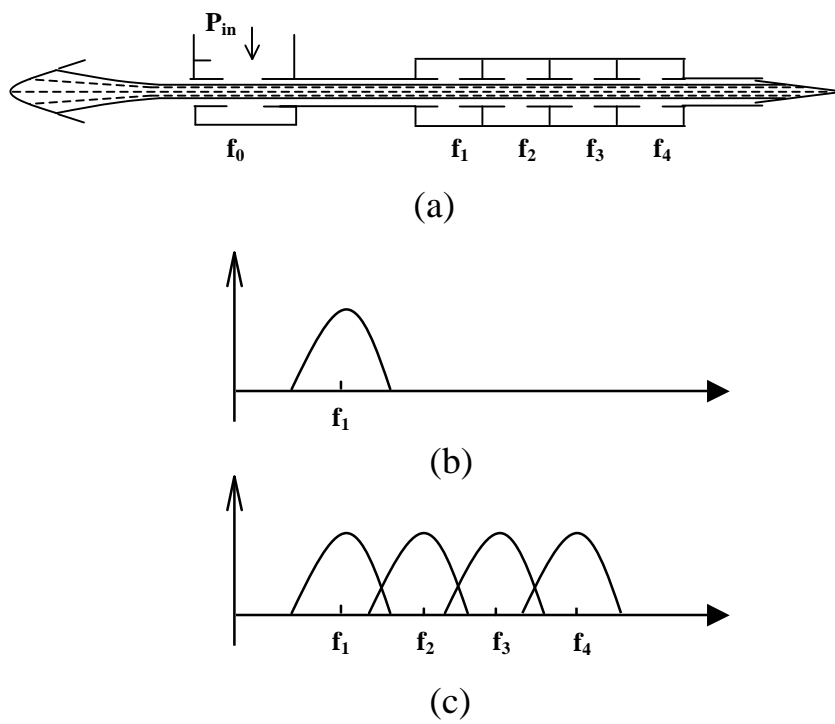
Figure 2. 2 Diagram of (a) a four-cavity cluster, (b) single frequency and (c) overlapped frequency bands.
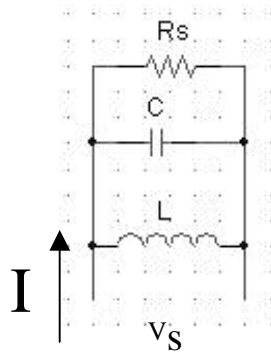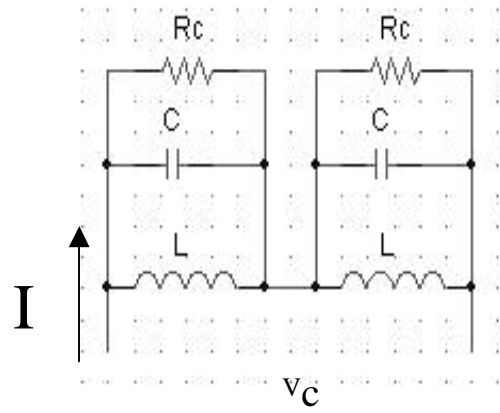
Figure 2. 3 (a) The single cavity lumped-parameter resonant circuit; (b) The cluster-cavity lumped-parameter resonant circuit.

Comparing (2.1) and (2.2), we can achieve the same bunching voltage by letting $mQ_c = Q_s$. This reduction of Q factor in clustered cavities then increases the bandwidth, so that $BW_c = m\ BW_s$; the bandwidth of the cluster-cavity device is m times that of the single cavity device. Thus, for the case of two cavities the bandwidth can be doubled.

2.2 Analytical Theory for Electron Prebunching in Harmonic-Multiplying Cluster-Cavity Gyro-Amplifiers

In this section, we derive analytic formulas that will be used to optimize a harmonic-multiplying cluster-cavity gyro-amplifier with respect to the parameters of the buncher cavities. Generally, we will vary these parameters so as to obtain a maximum in the bunched current at the second harmonic of the drive frequency at the location of the output section.

2.2.1 Analytical theory

The motion of gyrating electrons in electromagnetic waves in a gyro-amplifier can be described by a set of equations as follows [61]:

$$\frac{\partial(\gamma\beta_\perp)}{\partial z} = \frac{(\gamma\beta_\perp)^{s-1}}{\beta_z}\mathrm{Re}\left\{e^{-is\psi}V_s F_{\perp s}\right\}, \tag{2.3}$$

$$\frac{\partial\psi}{\partial z} = \frac{1}{\beta_z}(\frac{k_0}{s} - \frac{\Omega_0}{\gamma c}) + \frac{(\gamma\beta_\perp)^{s-1}}{\gamma\beta_\perp\beta_z}\mathrm{Im}\left\{e^{-is\psi}V_s F_{\perp s}\right\}, \tag{2.4}$$

where $\beta_\perp$, β_z are the transverse and longitudinal velocity divided by the speed of light; γ is the relativistic energy factor; Re and Im indicate the real and imaginary

35

part of a complex vector; s is the index of the interacting harmonic; $\psi = \xi + \omega t + \theta_0$, ξ is the gyro phase, θ_0 is the angle of the guiding center in a polar coordinate system, ω is the injected frequency; $k_0 = \omega/c$ is the wavenumber in vacuum; $\Omega_0 = qB_0/mc$ is the nonrelativistic cyclotron frequency, and B_0 is axial magnetic field. $V_s(z)$ is the complex voltage amplitude for a TE mode at the sth harmonic of the drive frequency ω in the interaction region and is normalized to q/mc^2. The complex TE field is represented as

$$E_T = \text{Re}\{V(z)\hat{\mathbf{e}}(r_T, z)e^{-is\omega t}\}, \tag{2.5}$$

where $\hat{\mathbf{e}}$ is the waveguide eigenvector, which for cylindrical waveguides is given by

$$\hat{\mathbf{e}} = \hat{z} \times \frac{1}{\left[\pi(1 - l^2/j'^2_{\ln})\right]^{1/2} j'_{\ln} J_l(j'_{\ln})} \nabla_T(J_l(j'_{\ln}r/r_w)e^{il\theta}), \tag{2.6}$$

where J_l is the ordinary Bessel function, r_w is the wall radius, and $j'_{\ln}$ is the nth zero of the derivative of the lth order Bessel function with respect to its argument. The quantity $F_{\perp s}$ is a coupling coefficient between the waveguide modes and the electron beam, and is expressed as

$$F_{\perp s} = -\frac{1}{\sqrt{\pi}}(\frac{j'_{\ln}}{r_w(z)})^s \frac{1}{2j'_{\ln}(s-1)!}(\frac{1}{2\Omega_0/c})^{s-1} he^{-is\pi/2}, \tag{2.7}$$

where

$$h = \frac{J_{l+s}(j'_{\ln}R_0/r_w)}{\sqrt{(1 - l^2/j'^2_{\ln})}J_l(j'_{\ln})}, \tag{2.8}$$

with R_0 being the guiding center radius.

The self-consistent amplitude $V_s(z)$ satisfies the following differential equation in the case in which only a single transverse mode of the waveguide is excited

$$\frac{\partial^2 V_s(z)}{\partial z^2} + (\frac{s^2 \omega^2}{c^2} - \frac{j_{\text{ln}}'^2}{r_w^2(z)})V_s = i\frac{s\omega}{c}S_s \qquad (2.9)$$

where S_s is the beam current source, and is defined as the following

$$S_s = \frac{4\pi}{c}\int J_T \cdot \hat{\mathbf{e}}^* \, da \,, \qquad (2.10)$$

where J_T is the electron current density at frequency $s\omega$. The source term is related to the particle trajectories via

$$S_s = 8\pi \frac{I_b}{I_A} F_{\perp s} \left\langle \frac{(\gamma \beta_\perp e^{i\psi})^s}{\gamma \beta_z} \right\rangle \qquad (2.11)$$

where I_b is the current of the beam, and $I_A = mc^3/q$, which corresponds to $1.7 \times 10^4 A$ when expressed in SI units. When ratios of currents such as I/I_A in Eq (2.11) appear, these may be evaluated in either system of units. The brackets imply an average over the electron entrance time or equivalently the initial phase $\psi(z=0)$.

In the analysis that follows we suppose that only a single transverse mode dominates the field distribution. However, the MAGY simulations presented in Chap. 2.2.2 allow for a superposition of transverse modes in the interaction region and account for the axially varying wall radius. We use this form of the equations, Eqs. (2.3)-(2.11), since these are the ones that are solved in the simulation code MAGY [61].

Equation (2.9) describes the self-consistent modification of the field amplitude due to the axial variation of wall radius and beam source current. In the case of

gyroklystrons with short and sharp cavities we can suppose that the field profile is determined primarily by the wall radius variations and we write

$$V_s(z) = f_{cl}(z)A_l \qquad (2.12)$$

where $f_{cl}(z)$ is the "cold cavity" field profile and A_l is a complex mode amplitude of the lth cavity. The cavity amplitude is then determined by multiplying Eq. (2.11) by f_{cl}^*, and integrating over the spatial region corresponding to the cavity

$$\left[1 - 2i\frac{Q_l}{\omega_{cl}}(s\omega - \omega_{cl})\right]A_l \int_{z_l} dz \mid f_{cl}^2 \mid = \frac{cQ_l}{\omega_{cl}} \int_{z_l} dz f_{cl}^* S_k \qquad (2.13)$$

Here ω_{cl} is the resonant frequency, and we have added a loss term to give the cavity a finite Q_l. Equation (2.13) is the analogue to the circuit equation (2.1).

Let us consider part of a gyro-amplifier consisting of a low Q (lower than the Q of the bunching cavities) input cavity, operating at the fundamental cyclotron harmonic, a first drift space, and a buncher consisting of either a single cavity or cluster of cavities at the second harmonic, followed by a second drift space, as shown in Fig. 2.4. In general, the length of each cavity as well as the cluster is small, compared with that of the drift regions. The "point-gap" model [68] is the limiting case of a very short interaction length in the cavities; it assumes that in the cavity interaction space the electron energy changes, but the phase is constant. In contrast, in the drift regions, the phase changes, and the energy is constant. Consequently the transverse momentum after the lth cavity is given by

$$(\gamma\beta_\perp)_l = (\gamma\beta_\perp)_0 + \frac{(\gamma\beta_{\perp 0})^{s-1}}{\beta_z} \sum_{l'=1}^{l} \text{Re}\left\{v_{l'}e^{-is\psi_{l'}}\right\}. \qquad (2.14)$$
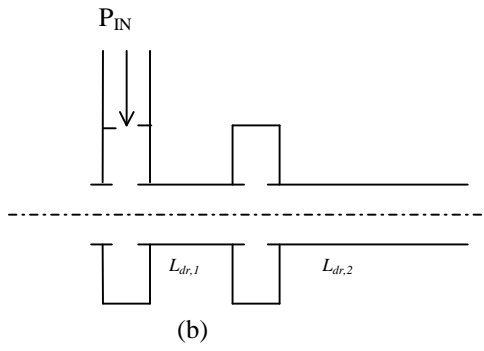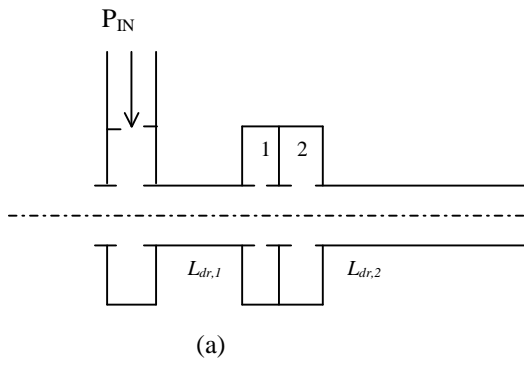
Figure 2. 4 (a) The diagram of the partial cluster-cavity buncher gyro-amplifier; (b) The diagram of the partial single cavity buncher gyro-amplifier.

where

$$v_l = A_l F_{\perp s} \int dz f_{cl}(z) \tag{2.15}$$

gives the change in transverse momentum of an electron on traversing the lth cavity, and ψ_l is the electron phase on entering the lth cavity.

The phase of each particle is modified due to the perturbation of the energy acting through the drift length between adjacent cavities,

$$\psi_{l+1} = \psi_l + L_{dr,l} \frac{\Omega_0 (\gamma \beta_{\perp 0})^s}{c \gamma_0^3 \beta_z^2} \sum_{l'=1}^{l} \mathrm{Re}\left\{ v_{l'} e^{-is\psi_{l'}} \right\} + \Delta_l, \tag{2.16}$$

where

$$\Delta_l = \int_{z_l}^{z_{l+1}} dz \frac{1}{\beta_z} \left(\frac{k_0}{s} - \frac{\Omega_0(z)}{\gamma_0 c} \right).$$

Here we assume that the change in electron energy is small up to the output.

By using the point-gap model, the amplitudes and phases of the fields in all cavities can be determined. In the input cavity, the amplitude of the field at the fundamental is

$$A_1 = k_0 \frac{cQ_1}{\omega_{c1}} \sqrt{\frac{4P_{in}}{P_0 Q_d}} \cdot \frac{1}{1 - i2Q_1(\omega - \omega_{c1} - \delta\omega_{B1})/\omega_{c1}} \tag{2.17}$$

where Q_d is the diffractive quality factor of the input coupler, P_{in} is the input power, $P_0 = (c/8\pi)(mc^2/q)^2$, which corresponds to $3.46 \times 10^8 W$ when expressed in SI units, is the normalization power that originates from the normalization of the amplitudes, and $\delta\omega_{B1}$ is the complex shift in frequency due to the beam loading of

the cavity. We will neglect this quantity in the analysis that follows. At resonance A_1 is real, thus all phases are referred to the phase of the field in the input cavity.

In the bunching cavities, the field amplitude A_l can be expressed in terms of bunched current using (2.11) and (2.13). Expressing the result in terms of the normalized voltage v_l from Eq. (2.15), we have

$$v_l = \frac{Z_{cav}Q_{2.l}}{1 - i2Q_{2,l}(2\omega - \omega_{cl})/\omega_{cl}} \left[\frac{I_b}{I_A} \frac{(\gamma\beta_{\perp0})^2}{\gamma\beta_{z0}} \left\langle e^{2i\psi_2} \right\rangle \right], \qquad (2.18)$$

where

$$Z_{cav} = \frac{8\pi c}{\omega_{cl}} \frac{\left| \int dz f_{cl} F_{\perp s} \right|^2}{\left| \int dz |f_{cl}|^2 \right|} \qquad (2.19)$$

is the normalized cavity impedance. Equation (2.18) now has the same form as the circuit equation (2.1). One can regard the quantity in square brackets as the (normalized) AC current, v_l is the (normalized) voltage and the quantity Z_{cav} defined in Eq. (2.19) plays the role of $\sqrt{L/C}$ in the circuit model.

We now consider the optimization of the second harmonic beam current at the location $z = L_{dr,1} + L_{dr,2} = L_T$, where $L_{dr,1}$ and $L_{dr,2}$ are the lengths of the drift regions between the input cavity and buncher, and the buncher and the output structure, respectively. The quantity we maximize will be the bunching factor

$$X_2 = \left| \left\langle e^{i2\psi_3(L_T)} \right\rangle_{\psi_1} \right| \qquad (2.20)$$

where the phase ψ_3 is obtained from Eq. (2.16) via

$$\psi_2 = \psi_1 + \Delta_1 + \rho \operatorname{Re}\left\{ q_1 e^{-i\psi_1} \right\} \qquad (2.21a)$$

$$\psi_3 = \psi_2 + \Delta_2 + (1-\rho)\,\mathrm{Re}\left\{q_1 e^{-i\psi_1}\right\} + (1-\rho)\sum_{l'=2}^{l}\mathrm{Re}\left\{q_{2,l'}e^{-i2\psi_2}\right\} \qquad (2.21\mathrm{b})$$

In Eqs. (2.21a) and (2.21b), we have introduced the fractional length of drift space number 1,

$$\rho = L_{dr,1}/L_T ,$$

where $L_T = L_{dr,1} + L_{dr,2}$ is the total drift space length. Also, we have introduced complex bunching amplitudes q_1 and q_2, according to

$$q_1 = L_T \frac{\Omega_0 \beta_{\perp 0}}{c\gamma_0^2 \beta_{z0}^2}\nu_1, \qquad (2.22\mathrm{a})$$

and

$$q_{2,l} = L_T \frac{\Omega_0 \beta_{\perp 0}^2}{c\gamma_0 \beta_{z0}^2}\nu_{2,l}. \qquad (2.22\mathrm{b})$$

The subscripts on $q_{2,l}$, $l = 1, 2$ denote the two cavities in a cluster. If only a single bunching cavity is used then the factor is denoted simply as q_2.

The bunching factor is related to the bunched current in a cavity through Eq. (2.18). Specifically,

$$q_{2,l} = \frac{N_{2,l}}{1 - i\delta_{2,l}}\left\langle e^{2i\psi_2}\right\rangle \qquad (2.23\mathrm{a})$$

where

$$\delta_{2,l} = 2Q_{2,l}(2\omega - \omega_{c2,l})/\omega_{c2,l} \qquad (2.23\mathrm{b})$$

is the dimensionless detuning of the buncher cavities and $N_{2,l}$ gives the strength of excitation of the bunching effect for each cavity,

$$N_{2,l} = L_T \frac{\Omega_0 \beta_{\perp 0}^4}{c\beta_{z0}^3}Z_{cav}Q_{2,l}\frac{I_b}{I_A}. \qquad (2.23\mathrm{c})$$

There are several approaches to maximizing the bunching factor depending on what is held fixed and what is allowed to vary. We first note that according to Eqs.

(2.23a)-(2.23c), if we allow for the total length L_T and detuning $\delta_{2,l}$ to be arbitrary, then any complex value of $q_{2,l} = |q_{2,l}| e^{i\phi_{2,l}}$ subject to $|\phi_{2,l} - 2\Delta_2| \le \pi/2$ can be realized. Further, since there is no drift space between cavities in a cluster, the optimization of the individual complex bunching factors $|q_{2,l}| e^{i\phi_{2,l}}$ is equivalent to optimization of the single bunching factor $|q_{2,l}| e^{i\phi_2} = \left| \sum_l q_{2,l} e^{i\phi_{2,l}} \right|$. This approach was taken in [69], where it was shown that optimum bunched current was obtained for $\phi_2 - 2\Delta_2 = \pm\pi/2$. The bunching factor can then be further optimized with respect to $|q_1|$, $|q_2|$ and ρ. The optimum values of these parameters as well as the optimized bunching factor are given in Table 2.1. These represent the best cases for a device with the configuration under consideration.

Table 2. 1 Optimized X_2 with respect to q_1, q_2 and ρ.

$\phi_2 - 2\Delta_2$	X_2	q_1	q_2	ρ
-π/2	0.8	2.4	1.41	0.22
π/2	0.84	2.25	32.0	0.975
No Buncher	0.486	1.53	0	1

Also shown in Table 2.1 is the bunching factor in the case of no bunching cavity (that is, simply, an input cavity). The increase in bunching factor over this value represents the improvement due to the presence of a buncher.

To realize these maximum values of bunching, namely $\phi_2 - 2\Delta_2 = \pm\pi/2$ requires large detuning of the bunching cavities, namely $\delta_{2,l} \to \pm\infty$. The resulting weakening of the bunching effect by the large detuning is offset by considering large

values of the parameter $N_{2,l}$ appearing in Eq. (2.23a). From Eq. (2.23c), we see that this requires large values of current or drift length $L_{dr,2}$, which may not be practical.

Our approach in the optimization will be to consider that current and drift length are limited by other practical effects such as beam stability and beam velocity spread, and to optimize bunching, with respect to detuning $\delta_{2,l}$, input bunching factor q_l and drift length ratio ρ. The device parameters that we consider are listed in Table 2.2 and correspond to those of the harmonic-multiplying amplifiers developed at the University of Maryland. We initially consider three drift lengths, $L_T = 10.0$, 15.5 and 20.0 cm. The length 15.5 cm is the same as that of the second harmonic phigtron [55], developed at the University of Maryland. Using the parameters of Table 2.2 and the three lengths, we find the corresponding excitation strengths $N_{2,l}$ are 2.62, 4.07, and 5.25, respectively.

Table 2. 2 Physical and geometrical parameters of the gyrodevices.

Electron beam	$V = 60$ kV, $I = 5$ A, and $\alpha = v_\perp / v_z = 1.5$
Input Cavity	$s = 1$, TE_{01} mode, $Q = 80$, length = 2.35 cm, radius = 1.127 cm, B = 6.45 kG
Drift section I	radius = 8.75 mm
Single Buncher cavity	$s = 2$, TE_{02}, $Q_{ohm} = 300$, $f_c = 33.82$ GHz, length = 1.4 cm, radius = 1.0 cm, B = 6.7 kG
Clustered Buncher cavities	$s = 2$, TE_{02}, $Q_{ohm} = 150$, $f_c = 33.82$ GHz, length = 1.4 cm, radius = 1.0 cm, B = 6.7 kG
Drift section II	radius = 8.75 cm

The next step is to optimize the bunching factor X_2 over bunching cavity detuning $\delta_{2,l}$ for each value of q_1 and ρ (we assume both bunching cavities have the same detuning). The optimized bunching factor $X_2(r, q_1)$ is then plotted in Figs. 2.5a, 2.6a and 2.7a for the three different lengths. The value of detuning giving the optimized bunching factor is plotted in Figs. 2.5b, 2.6b and 2.7b. The parameters which optimize the bunching factor are listed in Table 2.3. For all three cases, the input bunching parameter $q_1 = 1.55$ and drift length ratio $\rho_{opt} = 0.75$ are nearly the same. The optimized bunching factors are 0.55, 0.59 and 0.63 for the 10.0, 15.5, and 20.0 cm cases. These are intermediate to the values obtained for an infinitely long device $X_2 = 0.84$ and for a device with no buncher, $X_2 = 0.486$.

Table 2. 3 Optimized X_2 with respect to q_1, $\delta_{2,l}$ and ρ.

L_T (cm)	X_2	q_1	$\delta_{2,l}$	ρ
10.0	0.55	1.55	0.45	0.74
15.5	0.59	1.55	0.35	0.75
20.0	0.63	1.55	0.25	0.76

Realization of the "best case" can be approached if we allow longer drift lengths. This is illustrated in Fig. 2.8, where we plot the optimized bunching factor versus drift length for the parameters of Table 2.2. Two local maxima are plotted, which correspond to the positive and negative detuning cases of Table 2.1. The higher maximum corresponds to a drift length ratio $0.75 < \rho_{opt} < 0.9$ and detuning $0.9 < \delta_{2,l} < 0.26$, while the lower maximum corresponds to a lower drift length ratio $0.25 < \rho_{opt} < 0.3$ and detuning $-1.3 < \delta_{2,l} < -3.0$. For an infinite length device the optimized bunching factor for these two local maxima are about the same, $X_2 = 0.8$. However, if the device length is limited, the larger ρ_{opt} maximum is substantially higher. The
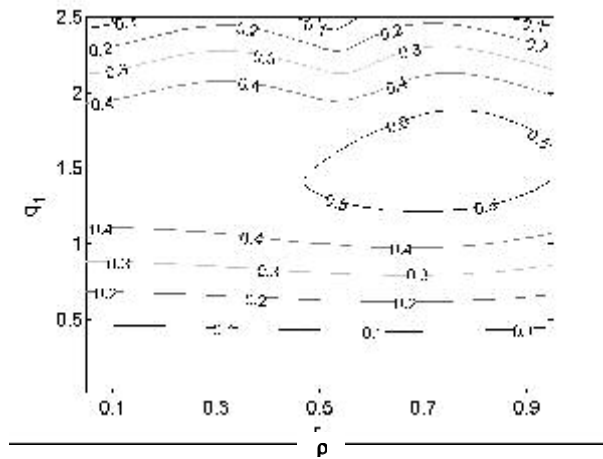
(a)
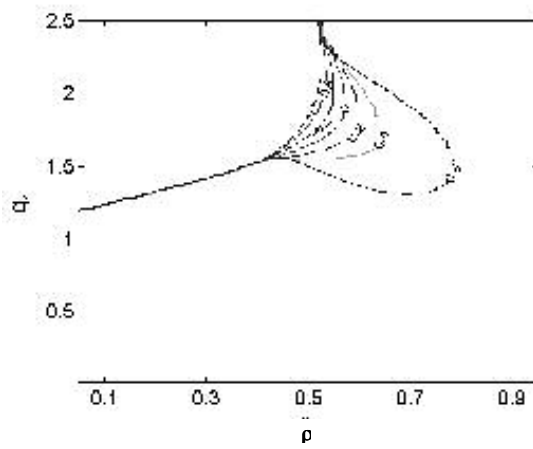
(b)

Figure 2. 5 Optimization for total drift section length $L_t = 10.0cm$; **(a) The second harmonic bunching factor X_2 after the buncher cavity as a function of the input cavity bunching parameter q_1 and the ratio of the first drift section length to the total drift section length ρ; each point is optimized with respect of the detuning $\delta_{2,1}$; (b) the detuning $\delta_{2,1}$ corresponding to the maximized second harmonic bunching factor X_2 in (a).**
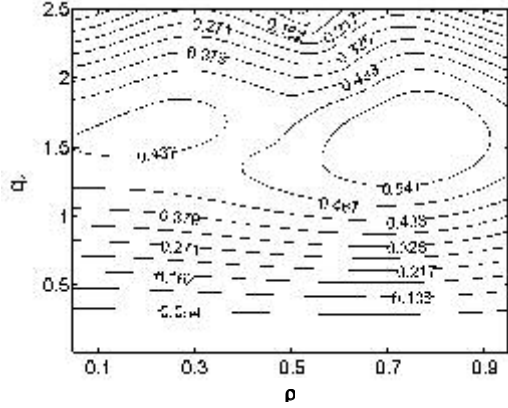
(a)
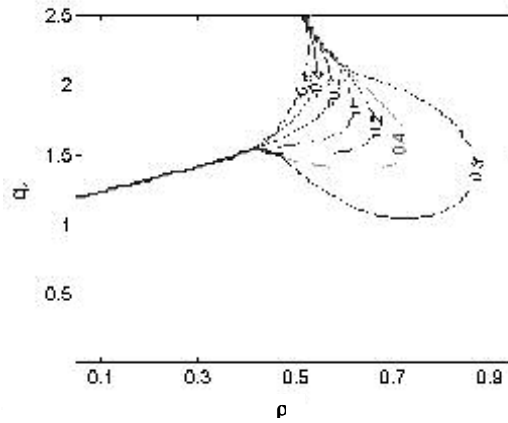
(b)

Figure 2. 6 Optimization for total drift section length $L_t = 15.5cm$; (a) The second harmonic bunching factor X_2 after the buncher cavity as a function of the input cavity bunching parameter q_1 and the ratio of the first drift section length to the total drift section length ρ; each point is optimized with respect of the detuning $\delta_{2,1}$; (b) the detuning $\delta_{2,1}$ corresponding to the maximized second harmonic bunching factor X_2 in (a).

(a)

(b)

Figure 2. 7 Optimization for total drift section length $L_t = 20.0cm$ **; (a) The second harmonic bunching factor** X_2 **after the buncher cavity as a function of the input cavity bunching parameter** q_1 **and the ratio of the first drift section length to the total drift section length** ρ**; each point is optimized with respect of the detuning** $\delta_{2,l}$**; (b) the detuning** $\delta_{2,l}$ **corresponding to the maximized second harmonic bunching factor** X_2 **in (a).**
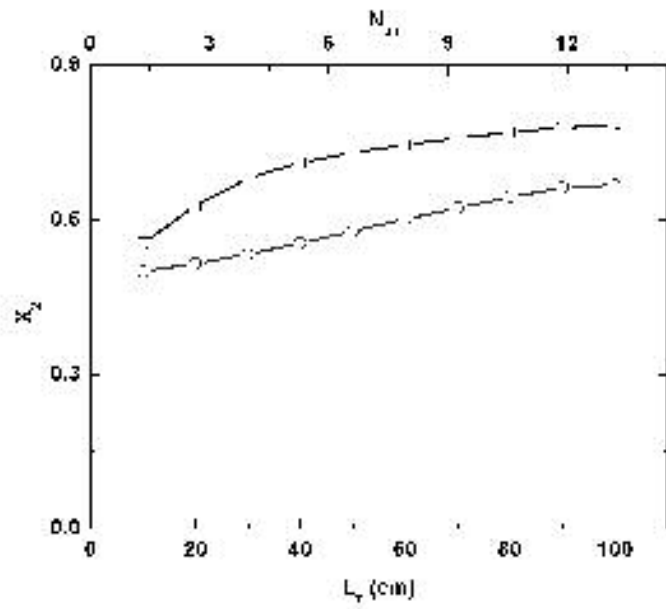
Figure 2. 8 The local maxima of the optimized bunching factor X_2 versus drift length L_T (bottom x-axis) and normalized parameter $N_{2,l}$ (top x-axis).

top horizontal axis is the scaled parameter $N_{2,l}$. As can be seen, one needs an excitation factor $N_{2,l} > 6$ to achieve a bunching factor $|X_2| > 0.75$.

We now explore in more detail the optimized design with the 15.5 *cm* length. Specifically, we consider a low-Q input cavity, $Q_{in} = 80$, with cold cavity resonant frequency $\omega_{c1} = 16.91\ GHz$, and $B = 6.45\ kG$. The maximum X_2 occurs at $P_{in} = 1500\ W$ and is at the second harmonic of the operating frequency $\omega_2 = 33.84\ GHz$ with bunching cavity detuning $\delta_{2,l} = 0.35$. If we replace the bunching cavity with a cluster consisting of a pair of cavities, but $Q_{cluster-cavity} = $ ½ $Q_{singlecavity} = 150$, we get the same maximum X_2 at the same optimized point, except that the operating frequency is $\omega_2 = 33.86\ GHz$ with detuning $\delta_{2,l} = 0.35$ because the cluster-cavity Q factor is half that of single cavity. This yields a device with the same drift section length, maximum gain, and efficiency as the single buncher cavity design. However, the bandwidth is twice as large as that of the single buncher design. This design will be further considered using MAGY simulation in the next section.

2.2.2   MAGY simulation results

Further studies of cluster-cavity devices have been conducted using the MAGY code [61] code. The code includes a time-dependent description of the electromagnetic fields and a self-consistent analysis of the electron motion. The field in MAGY is represented as a superposition of TE and TM modes of a waveguide of circular cross-section, which allows the solution of a relatively small number of coupled one-dimensional partial differential equations for the amplitudes of the modes, instead of the full solution of Maxwell's equations. In addition, the basic time scale for updating the electromagnetic fields is the cavity fill time and not the

period of the high frequency fields. Here, first, we investigate how to provide enough isolation between the cavities in a cluster. Secondly, we compare the simulation results of two partial gyrodevices, one with a single cavity buncher, and the other with a two-cavity cluster buncher to verify our optimizations of bunched current in the previous section. Thirdly, we numerically study how the coupling between cavities in a cluster degrades the performance of the cluster-cavity. Finally, we compare the performance of a single cavity buncher and a three-cavity cluster.

2.2.2.1   Single cavity and clustered cavities

By using the results obtained from analytical analysis, we can input the geometry into MAGY and compare the two cases; one with a cluster-cavity buncher, and the other with a single cavity buncher. The diagram of the two cases is shown in Fig. 2.4. Both have the same beam and cavities parameters as those used in the analytical optimization. The optimum drift space length is $L_{dr,1} = 11.6$ cm, and $L_{dr,2} = 3.9$ cm with total drift section length of 15.5 cm and cavity detuning of 0.35. Other beam, magnetic field and cavity parameters are listed in Table 2.2.

However, before we conduct any MAGY simulations, we have to address an important issue raised when inserting clustered cavities in a gyro-amplifier. This is the presence of a large beam tunnel radius, which makes it difficult to isolate the cavities in a cluster. To minimize the coupling between cavities in a cluster, the diameter of the cavity end is cutoff for the operating mode. Also, absorber is used at each end. In the simulation, a loss of 30 dB/cm is set between two cavities in the cluster. The isolation in the simulation can be determined by comparing the cavity field amplitude in one cavity when a test source is set in the middle of an adjacent cavity. Here, we use a two-cavity cluster as an example. Figure 2.9 shows the simulated isolation between the cavities in the cluster and is more than -30 dB for the
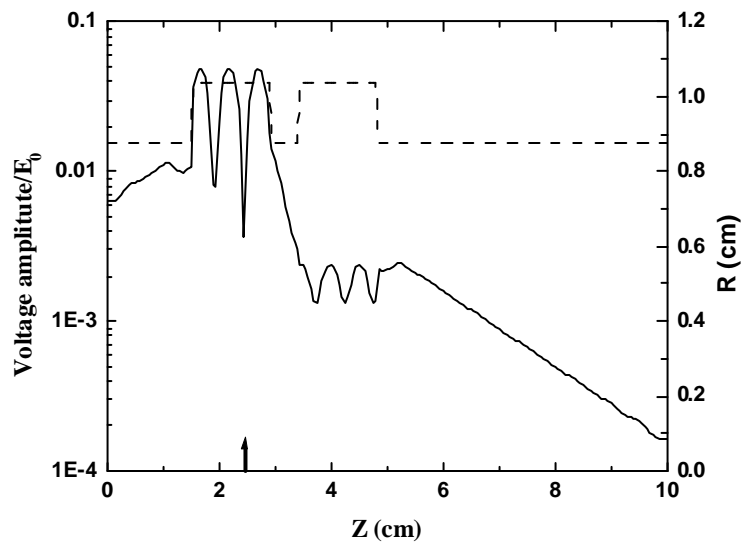
(a)
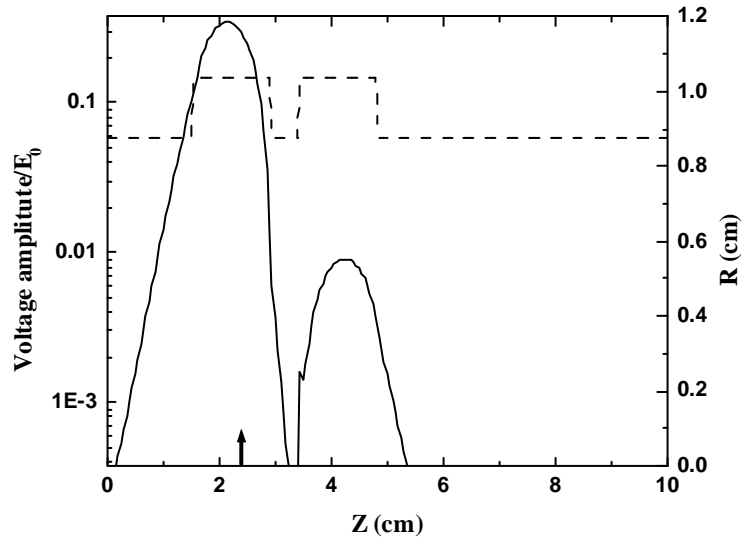
(b)

Figure 2. 9 (a) The isolation for the operating mode TE$_{02}$; (b) the isolation for the low-order TE$_{01}$ mode; in both cases, the test source is in the middle of the first cavity (indicated with an arrow), and the field amplitude is normalized to $E_0 = q/mc^2$.

operating mode TE_{02}, which is consistent with cold test results for similar fabricated cavities, detailed in chap 2. 3.

Figure 2.10 shows the drive curve results from MAGY simulations of a single buncher and a cluster-cavity buncher. Plotted is the source term defined in Eq. (2.10), which is proportional to the bunched current. Both drive curves peak at an input power level 1500 W, but the cluster-cavity buncher current is 2.5% lower that of single cavity buncher's. From the simulations, we find that the source term is maximized for a second drift section length $L_{dr,2} = 4.5$ cm, which is slightly larger than the predicted length $L_{dr,2} = 3.9$ cm. This can be explained by studying the field amplitudes in the bunching cavities. The frequency response of the field voltage amplitude of the dominant TE_{02} mode in the two kinds of bunchers is depicted in Fig. 2.11. The bandwidth of each cavity in the cluster is 0.68%, twice that of a single cavity, 0.34%. Compared with the point-gap model predictions (solid line), the amplitude of the single bunching cavity is 3% lower, while for the cluster buncher, the amplitude in the second cavity agrees with the theory nicely, but that in the first cavity is 8% lower. The differences between the theory and numerical simulation mainly originate from the point-gap assumption, where the length of cavity as well as the gap between cavities is ignored. In the single cavity, the difference is relatively small. However, in the cluster, the phase difference between the adjacent cavities is assumed to be 0°, which does not count the electron phase modulation in the first cavity and the transit angle. Not surprisingly, MAGY computes a value of 11.8° , which explains why the voltage amplitude is higher in the second cavity. To minimize to transit angle between cavities in the cluster, the clustered cavities should be operated close to cutoff.

The frequency response of the source term is shown in Fig. 2.12. In the small signal regime, the MAGY simulation clearly shows that the source term for the

Figure 2. 10 The source term versus input power for the cluster (dashed line) and single cavity (solid line) buncher cases.
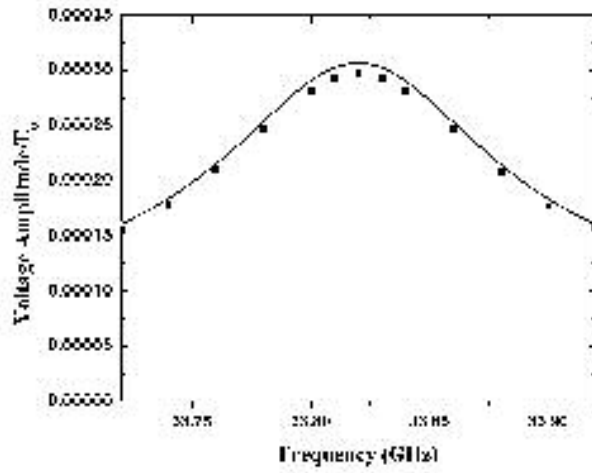
(a)
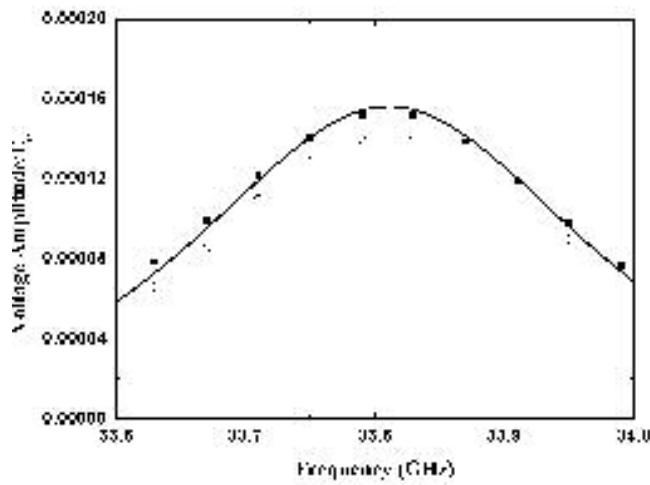
(b)

Figure 2. 11 (a) The normalized voltage amplitude of the dominant TE$_{02}$ mode from the theory (solid line) and simulation (square) in the single bunching cavity; (b) the normalized voltage amplitude of the dominant TE$_{02}$ mode from the theory (solid line) and simulation (circle for the first cavity and square for the second cavity) in the clustered bunching cavities.
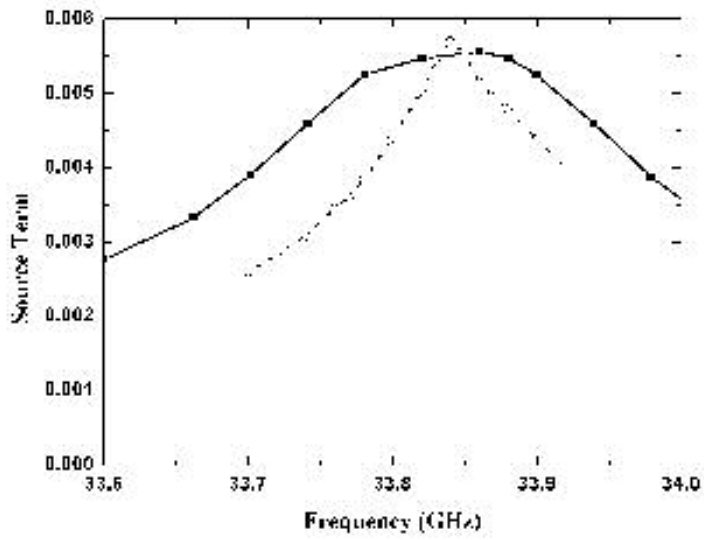
Figure 2. 12 MAGY code simulations of the bandwidth of the cluster-cavity (solid line + square) and single cavity (dash line + circle) cases.

single cavity buncher case has a peak at frequency 33.84 GHz, which is 0.02 GHz off the resonant frequency of the bunching cavities. This agrees with the theory, which predicts an optimum cavity detuning of 0.35. For the cluster-cavity buncher, the source term peaks at 33.855 GHz, again given roughly 0.35 cavity detuning. The bandwidth of the cluster-cavity case, 0.75%, is approximately twice than of the single cavity case, 0.38%.

Further study of efficiency, bandwidth and output power is also conducted using MAGY. A gyro-TWT output, which operates at the second harmonic in the TE_{03} mode with radius 1.45 cm, is added to the two structures discussed above, and the diagram of these two devices is shown in Fig. 2.13. Here, the beam current is 17 A and external magnetic field is 6.5 kG. The efficiency versus bandwidth curves are shown in Fig. 2.14. We note that the saturated bandwidth (fixed input power, swept frequency) is increased to 1.08% compared with the 0.627% bandwidth for the bunched current. The MAGY code simulation shows that for the cluster-cavity case the gain-bandwidth product is 1.1×10^4 dB×MHz, and for the single cavity case the product is 0.6×10^4 dB×MHz. The gain-bandwidth product of a cluster-cavity device approximately doubles that of the single cavity device. Taking the length of the output section into account, the second drift section length has to be shortened in order to have the peak of the bunched second harmonic current occurring in the output section.

Compared with Ka band high order mode gyro-amplifiers, the calculated gyro-amplifier, as shown in Table 2.4, has wider bandwidth than gyroklystron devices and higher efficiency than gyro-TWT type devices.

2.2.2.2   Cluster with coupled cavities
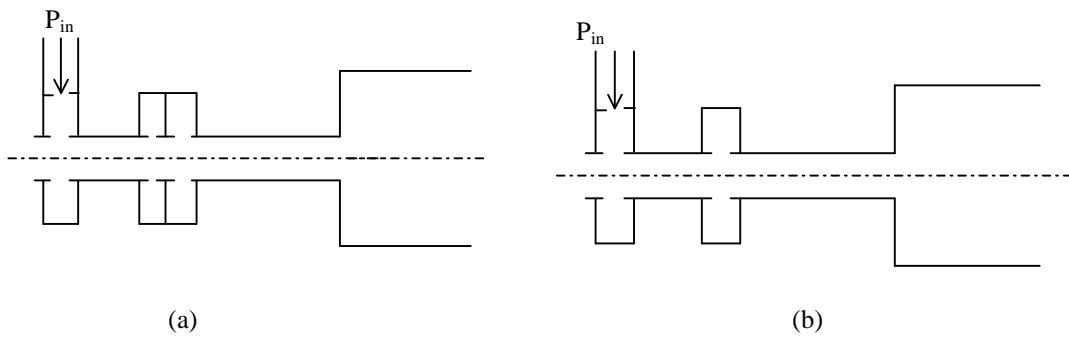
Figure 2. 13 The diagram of the two gyro-amplifiers, (a) with a cluster-cavity buncher, and (b) with a single cavity buncher. Both amplifiers have a fundamental harmonic input cavity, a second harmonic gyro-TWT output, and employ a second harmonic buncher.
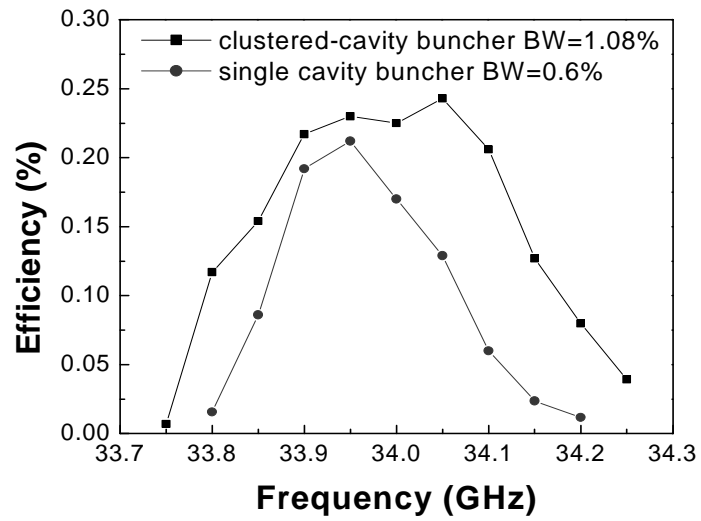
Figure 2. 14 The efficiency versus frequency for the cluster-cavity and single cavity buncher gyro-amplifiers from MAGY simulation.

One of the key points of the cluster-cavity concept is that the cavities in the cluster should be uncoupled. To better understand the coupling effect, the isolation between the cavities in the cluster is decreased to -10 dB/cm, which provides about -10 dB isolation between cavities. We still use a cluster with a pair of cavities as the example. Figure 2.15 is a comparison of the drive curves for a single cavity and a cluster-cavity buncher. The peak of cluster-cavity case is 30% lower than that of the single cavity. Figure 2.16 shows the field amplitudes of the coupled cavities, which are over 26% lower than the theoretical prediction (solid line). With the same cavity loaded Q factor, the coupling between the cavities reduces the field intensity, and further reduces the second harmonic bunching current in the electron beam. In practice, it is thus necessary to minimize coupling as described in part A of this section.

Table 2. 4 The two-cavity cluster buncher gyro-amplifier performance compared to Ka band gyro-amplifiers.

Institute [reference] year	V_b (kV)	Output mode	Peak power (kW)	Gain (dB)	Efficiency (%)	Bandwidth 3dB (%)
Cluster buncher gyro-amplifier	60	TE_{03}	250	30	25	1.1
IAP/Tory [46]	75	TE_{02}	750	20	24	0.6
IAP [47]	60	TE_{02}	125	15	15	0.1
Phigtron [55]	52	TE_{03}	720	30	35	0.7
UMCPgyro-TWT [42]	50	TE_{03}	180	27	12 (linear)	3.2
NRL gyro-TWT [43]	72	TE_{01}	137	47	17	3.3

2.2.2.3   Three-cavity cluster

It is worth investigating the limits on the number of cavities used in the cluster. To make clustered cavities effective, the length of cavities as well as the spacing between cavities have to be very short. From the analysis in Sec. III, one of the
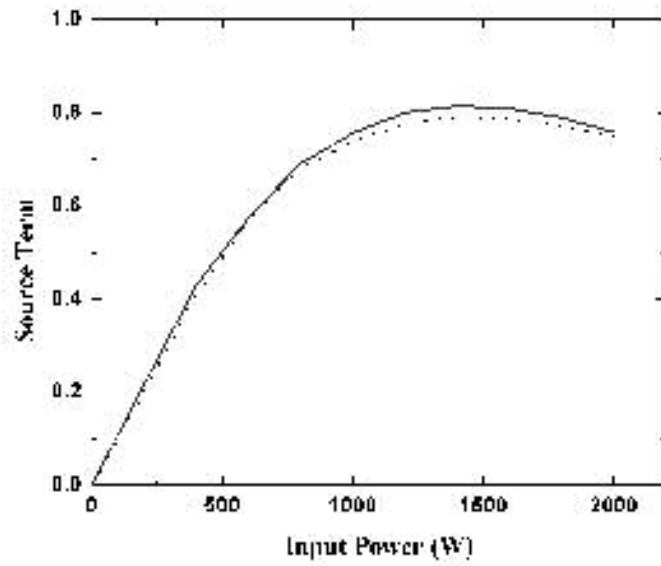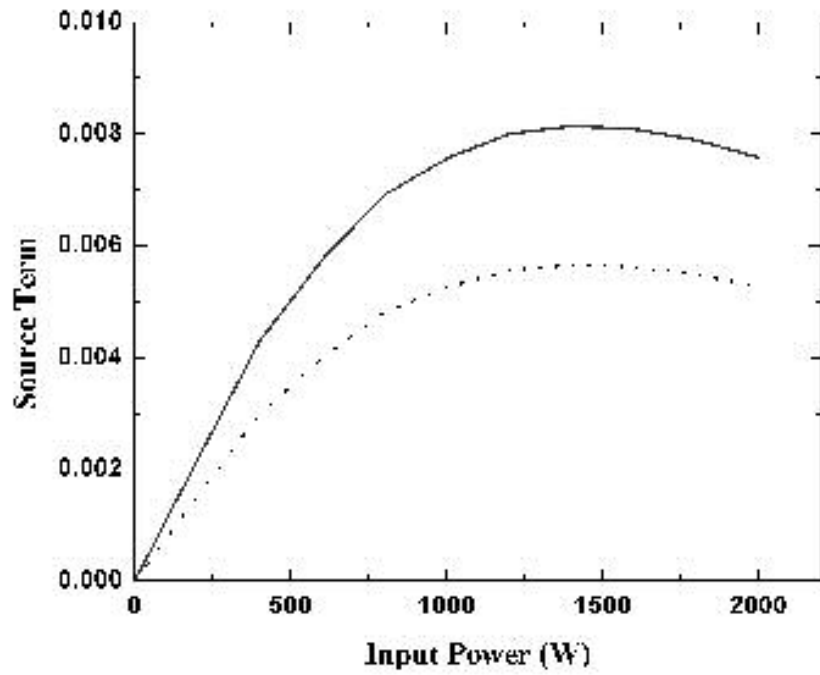
Figure 2. 15 The source term versus input power for the coupled-cavity cluster (dash line) and single cavity (solid line) buncher cases.
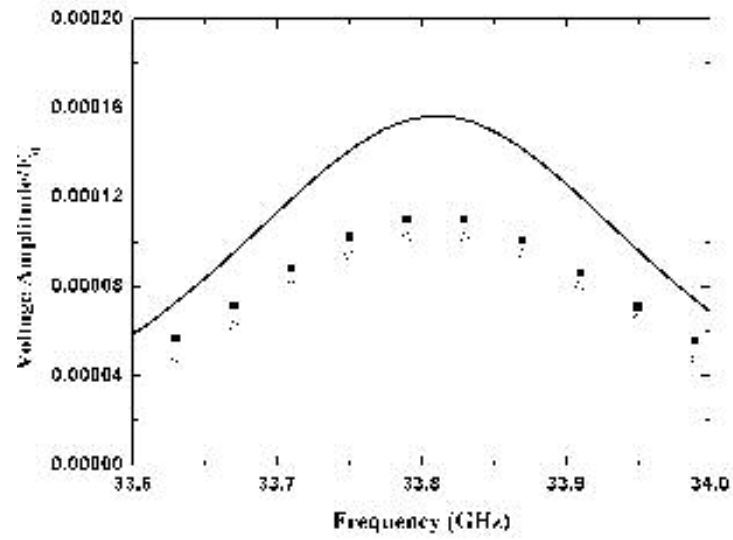
Figure 2. 16 The normalized voltage amplitude of the dominant mode from the theory (solid line) and simulation (circle for the first cavity and square for the second cavity) in the cluster buncher.

dominant control factors of the second harmonic current is the modulation strength in the bunching cavity, which is $q_{2,l} = \sum_l q_{2,l}$, where $q_{2,l}$ is defined in Eq. (2.22b).

To guarantee the performance of clustered cavities, the phase differences between the cavities in a cluster have to be small. However, using the same beam and cavity parameters as in Table 2.2, in the MAGY simulation the phase difference between cavities is 11.8°. When another cavity is added to the cluster in the MAGY simulation, the results (in Fig. 2.17) show that the source term of the three-cavity case is 10% lower than that of the single cavity case. It is expected that with increasing number of cavities in the cluster, we should modify cavity parameters in order to have good performance. The bandwidth of the three-cavity cluster buncher is 1.05%, is about three times of the single cavity buncher 0.38%, as shown in Fig. 2.18.

2.2.3   Summary

An analytical theory of frequency doubling gyroklystrons with cluster-cavity bunchers has been developed to maximize the second harmonic current and optimize the drift section length. MAGY simulations have been conducted to compare with the theory and further study the efficiency, bandwidth and output power. The theory and MAGY simulation largely agree with each other. In the small signal regime, the bandwidth of the cluster-cavity (with a pair of cavities) is twice that of a single cavity, while both have the same peak bunching. For the case of a two-cavity cluster buncher and a gyro-TWT output section, a peak power of 247 kW, efficiency of 24.2% and bandwidth of 1.08% have been calculated. The gain-bandwidth product for this design is 1.1×10^4 dB×MHz, which approximately doubles the single cavity buncher power-bandwidth product.
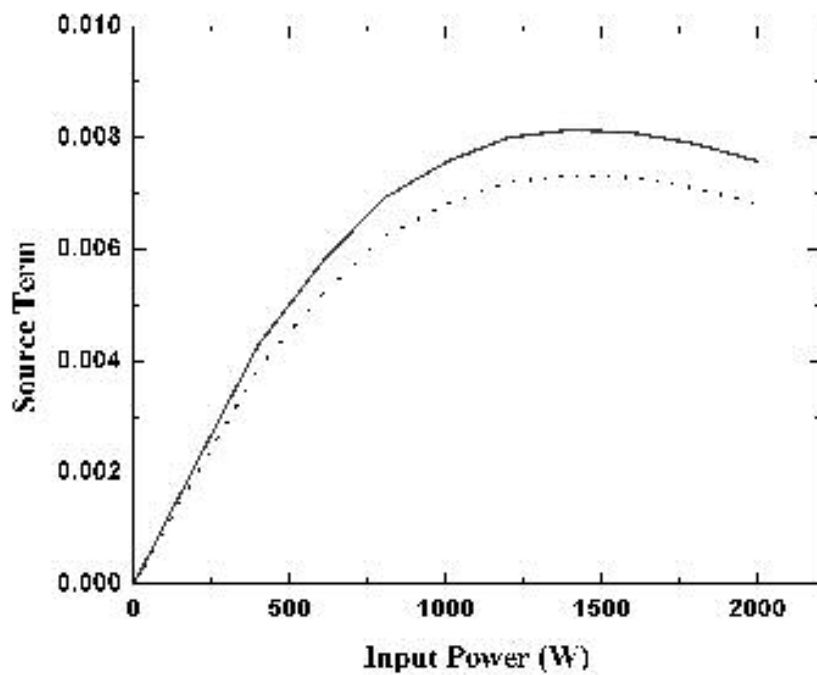
Figure 2. 17 The source term versus input power for the three-cavity cluster (dash line) and single cavity (solid line) buncher cases.
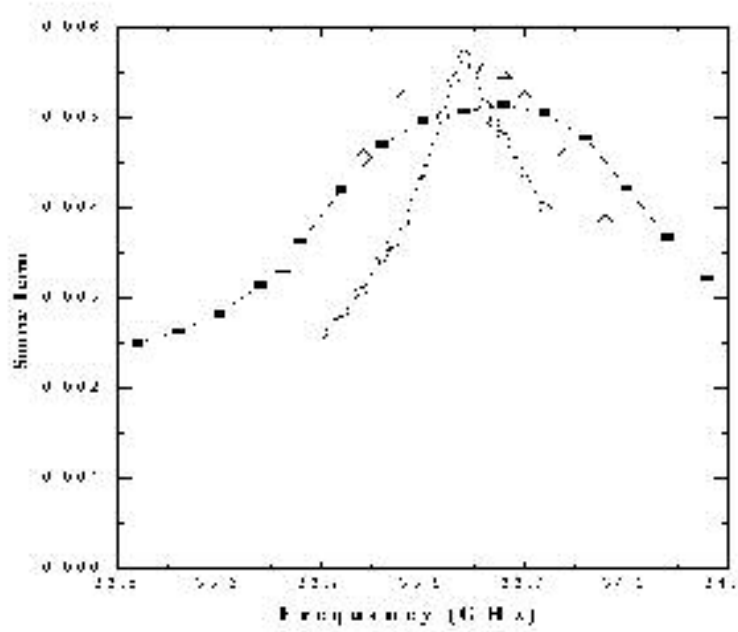
Figure 2. 18 MAGY code simulations of the bandwidth of the three-cavity cluster (solid line + square) and single cavity (dash line + circle) cases. The results are also compared with two-cavity cluster results (shown as triangle).

2.3 Design and Construction of Clustered Cavities

In this section we will discuss the design and experimental testing of four-cavity cluster gyro-TWT that was carried out prior to the optimization described in previous section. The considered device was designed to have stagger tuned cavities so the results of the optimization for common resonant frequency cavities do not apply. The design and cold testing of the cavities were carried out by the present author and will be discussed here while the hot test of the device was carried out and was described by Rodgers et al [71, 76, and 77]. Experimental details will give in section 2.4. Unfortunately, in the hot test, not all design parameters were achieved, in particular, the beam current was below the design value. Consequently, the device did not perform according to expectations. Nevertheless we will simulate the device using MAGY and compare with the experimental data in section 2.4.3.

2.3.1   Simulation results from HFSS code

From the engineering perspective, realizing TE clustered-cavity for gyro-amplifiers application requires attention to many different, and sometimes competing, issues. As is the case in conventional slow-wave amplifiers, stability is an important issue in gyro-amplifiers, which can limit their performance. In a gyrotron using a TE clustered cavity, instability may occur in the sub-cavities and between sub-cavities in a cluster. Successful design of a TE clustered-cavity must address the stability in all these regions. Mode competition is also a very important issue in gyrotron circuit design. For suppression of parasitic modes in the circuit, a variety of methods can be employed, including the addition of structure in the cavities in order to interrupt the electric mode pattern for the competing modes while maintaining the integrity of the operating mode. In a gyrotron, the transverse

dimensions of both the electron beam and circuit are much larger than those in klystrons or slow-wave microwave tubes because gyrotrons operate in fast wave, higher-order, transverse electric modes. This raises another issue in TE clustered-cavity design: the wider beam tunnel makes the radiation-free condition more difficult to realize. But by applying microwave lossy materials in appropriate regions, this problem can be resolved.

Under above the considerations, a high order TE_{0n} mode-selective clustered-cavity was designed using HFSS a finite element electromagnetics code that calculates field distributions and S parameters for passive three-dimensional (3-D) structures.

Figure 2.19 shows the 3D view of a quarter sub-cavity in a multiplet. Basically, it is a cylindrical cavity resonating in the TE_{031} mode with power magnetically coupled to the TE_{021} mode of an inner cavity through four slots spaced 90° apart around the azimuth of the common wall (the part in blue). Absorbers (components in yellow) are used at each cutoff end.

The inner radii of the outer and inner cavities are a and b, respectively. These cavities are designed to operate, respectively, in the TE_{02} and TE_{03} modes. In order to couple these two modes into one normal mode of a complex cavity, the eigenfrequencies of these two modes must be the same. This is accomplished by choosing radii a and b to satisfy the condition

$$\frac{\mu_{02}}{a} = \frac{\mu_{03}}{b} = k_c \qquad (2.25)$$

where eigennumbers μ_{02} and μ_{03} are roots of the equations $J'_0(\mu_{02}) = J'_0(\mu_{03}) = 0$, J_0 is the zero-order Bessel function, and k_c is the cutoff wavenumber, which is the same for both modes. Four evenly spaced slots on the inner cavity are designed to realizethe desired coupling between these two modes.
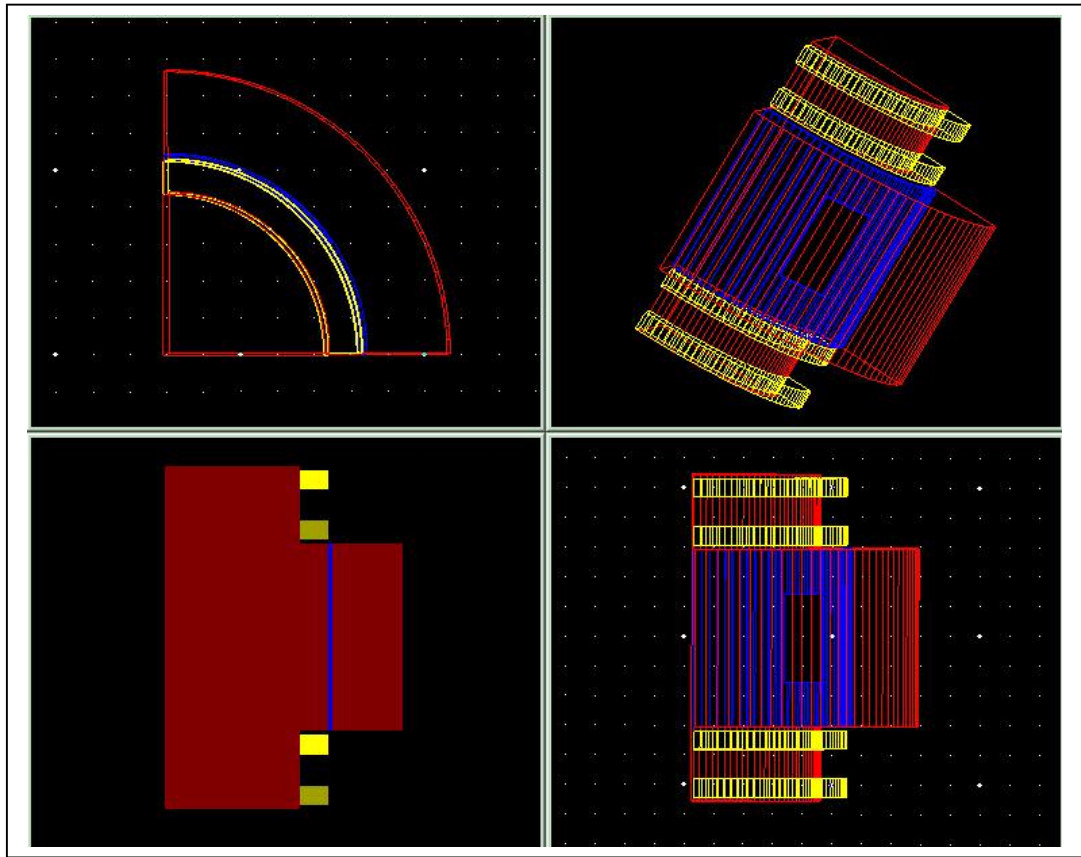
Figure 2. 19 3D view of a quarter cavity in a multiplet, generated with the HFSS.
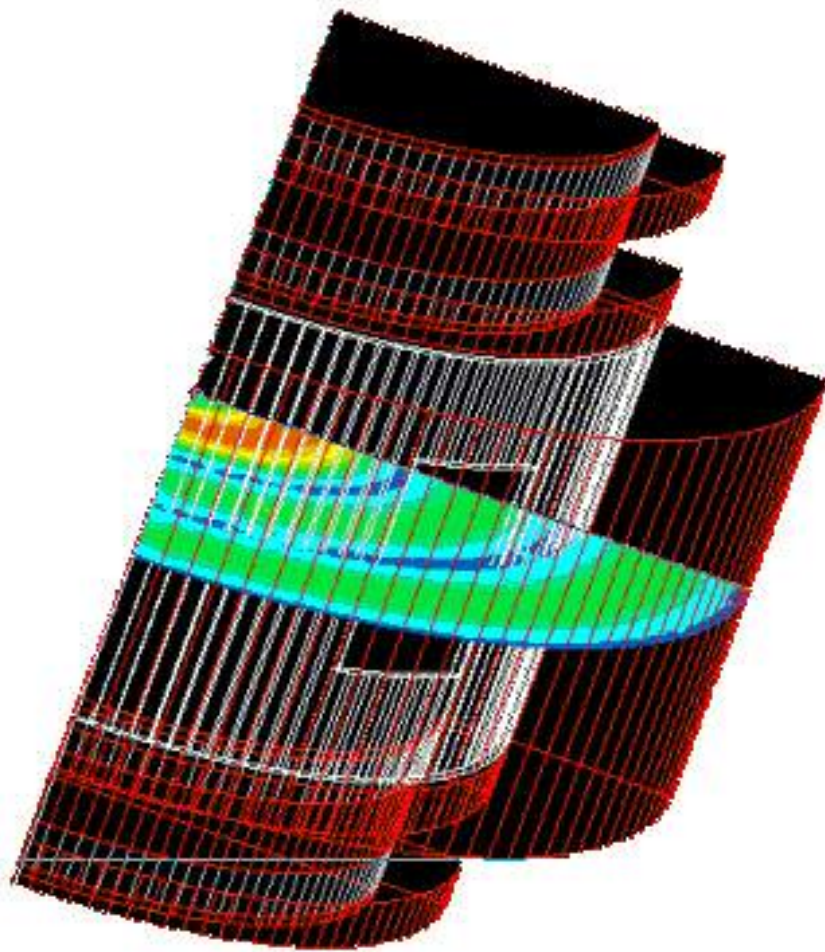
Figure 2. 20 Transverse electric field structure of TE Clustered-cavity subunit.
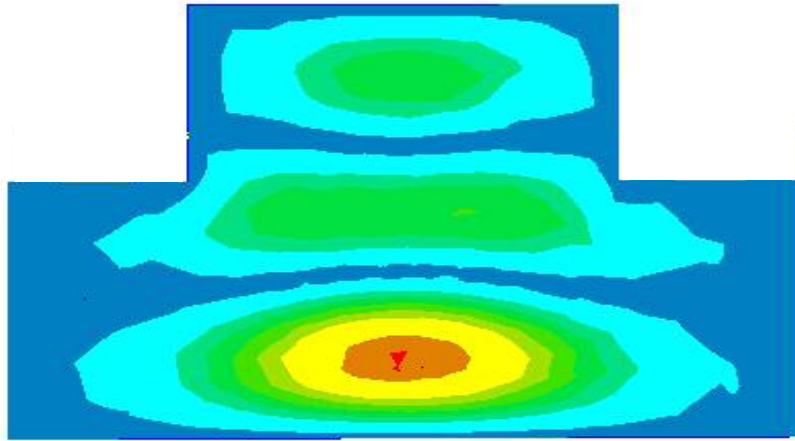
(a)
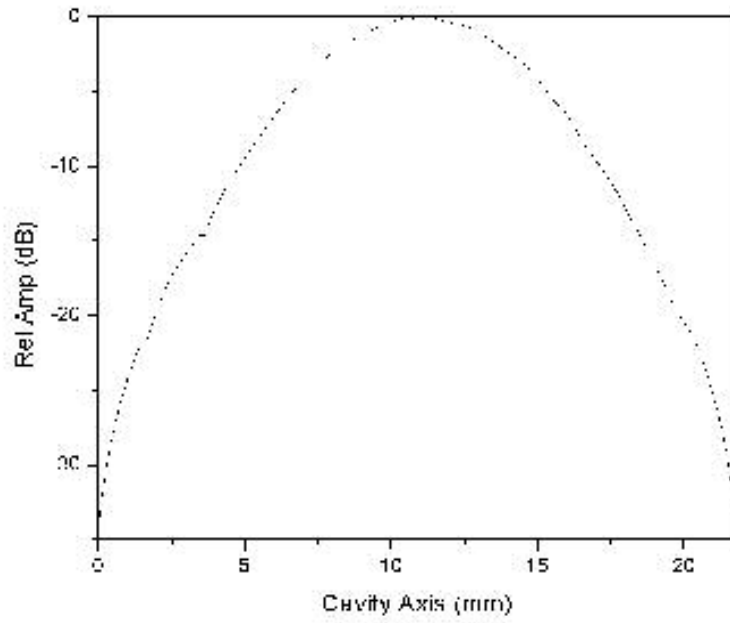
(b)

Figure 2. 21 (a) Azimuthal electric field pattern in a Clustered-cavity subunit. (b) Corresponding relative amplitude of E field along the axial cavity axis. Cavity length is 12mm, and gap between cavities is 6.5mm.

Superior mode selectivity has been demonstrated from the HFSS simulation, the transverse electric field pattern of one sub-cavity in a cluster is shown in Fig. 2.20. Clearly, there is a TE_{03} mode in the whole cavity. Figure 2.21a shows the axially profiled electric field pattern of the first axial mode in a cavity. The relative amplitude of E field along the cavity axis is also shown in Fig. 2.21b. From the center of one sub-cavity to the edge of the adjacent sub-cavity, the field is down by – 33 dB. It should be noted that, to save computation time, only a quarter of the sub-cavity was modeled using HFSS, as shown in figure 2.19. And the two surfaces of the wedge were assigned to be perfect conductor, which may neglect TE_{2n} modes in the process of simulation.

To minimize coupling between sub-cavities, the diameter of the cavity end is cutoff to the operating mode. Also, absorber, which is in the shape of a tube with the same inner diameter as that of the cavity end, is used at each end. In practice, it is constructed by stacking a series of lossy SiC ceramic washers, as well as a unique honeycomb-like structure, which has crossed grooves (sprayed with *TeNiCrCoAl* lossy alloy) inside the housing. Photos of the ceramic rings and the honeycomb structures are shown in Fig. 2.22.

2.3.2   Experimental results

The four-unit clustered-cavity detailed in Table 2.5 was constructed and cold tests were performed with a network analyzer. The design layout of this cavity is shown in Fig. 2.23. In the cold tests, the cavities were excited and sampled through a hole in the side wall, as shown in Fig. 2.24a. Rectangular TE_{10} mode was injected to excite TE_{0n} mode in the cavity and S_{11} parameter was measured.

The values of measured-resonant frequency are detailed in Table 2.5. The differences in the design and measured cavity parameters result from machining tolerances. Also, the cold test measurements were performed in air, not vacuum.

(a)

(b)

Figure 2. 22 (a) Highly lossy ceramic rings and (b) High lossy honeycomb structure used at the ends of a TE clustered-cavity.

7.1*3.6

Rout

L2

L1
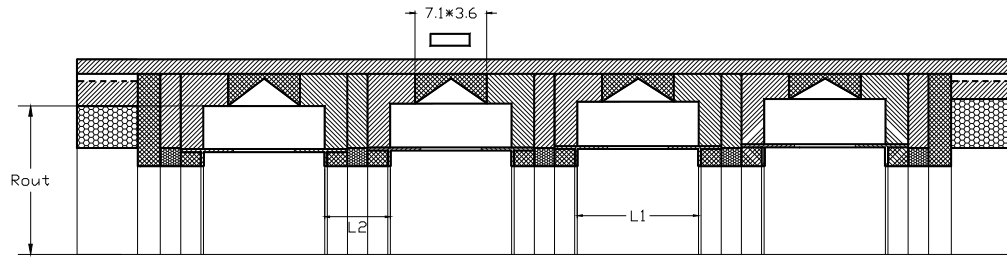
L1 = 12mm
L2 = 6.5mm

Metal
Lossy Ceramic
Lossy Honey-Comb

Figure 2. 23 Design layout of four-unit clustered-cavity.
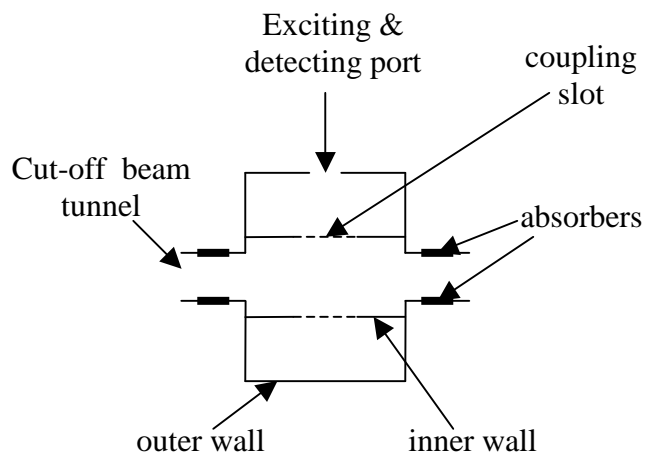
(a)
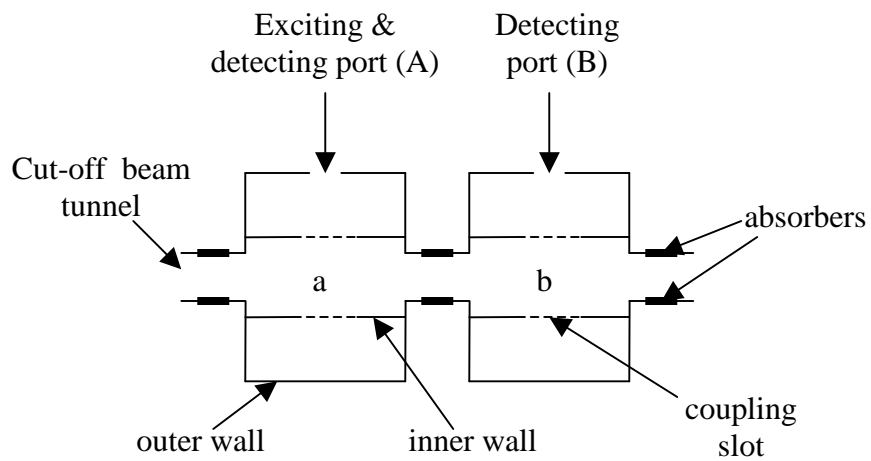
(b)

Figure 2. 24 Schematic of the cavity cold test: (a) Resonant frequency measurement setup; (b) Coupling measurement setup.

Table 2. 5 Design and measured parameters for the four-unit clustered-cavity.

Sub-cavity no.	Design			Cold Test
	outer radii (mm)	f_0 (GHz)	Q	f_0 (GHz)
1	15.33	33.59	88	33.49
2	15.08	34.04	111	33.85
3	14.88	34.40	137	34.30
4	14.65	34.82	195	34.68

Thus, the resonant frequencies under vacuum will be higher than those determined in the cold test; the lower frequencies in the cold test are partially due to the dielectric constant of air at standard temperature and pressure.

Also, a series of experiments were undertaken to investigate the isolation between the adjacent cavities. The experimental setup is shown in Fig. 2.24b. An initial study was conducted using small perturbation technique. The clustered-cavity was excited and sampled through the port A and a dielectric rod was used to perturb the field in the region between the cavities, and in cavity B. No changing of S_{11} parameter was observed. The experiment was further performed by measuring the transmission characteristic, S_{21} of the adjacent cavities by exciting at port A and detecting at port B. From these experiments, more than –30 dB coupling was achieved, thus it was concluded that an acceptably small coupling occurred between the cavities in the cluster.

2.4 A Gyro-Amplifier with Clustered Cavities

2.4.1 Design of a gyro-amplifier with clustered-cavities

Upon completion of the cold test, the TE clustered-cavity was installed in a new type of gyro-amplifier tube as a wideband buncher cavity. The amplifier is sketched
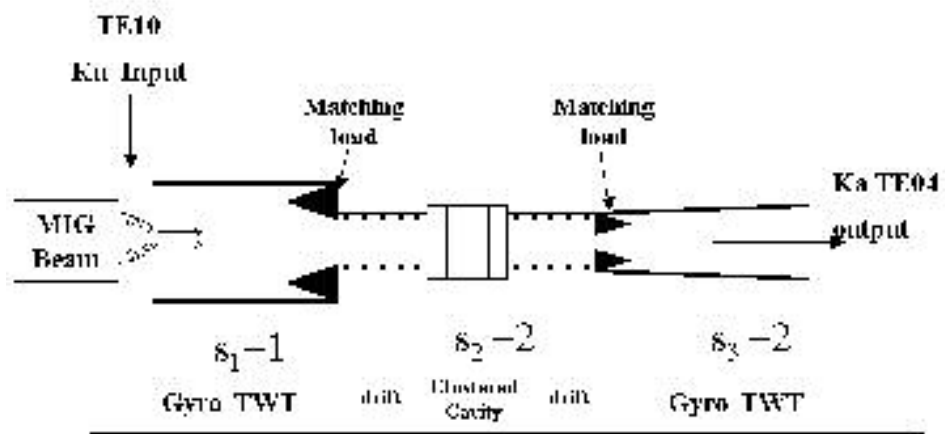
Figure 2. 25 Schematic of the cluster-cavity gyro-amplifier.

in Fig. 2.25. The device consists of a short Ku-band gyro-TWT input stage to modulate the beam at the $s_1=1$ cyclotron harmonic, the four-unit stagger-tuned clustered-cavity as intermediate stage to bunch the beam at the $s_2=2$ cyclotron harmonic and a Ka-band longer gyro-TWT output stage to extract energy from the bunched beam at the $s_3=2$ cyclotron harmonic. The detailed structure is schematically shown in Fig. 2.26.

2.4.1.1 Input coupler

A new input coupler, designed by the HFSS code, is used in the gyro-amplifier, as shown in Fig. 2.27. A rectangular waveguide, which is used to feed the waves into a tube, smoothly changes to a coaxial waveguide by increasing the inner arc and outer arc of coupling slot until a coaxial waveguide is formed. During the transition process, the two arcs are constrained to correspond to the same central angle. The dominant TE_{10} mode in a rectangular waveguide has only one electric field component, which eventually becomes the azimuthal component, which is also the only electrical component of waves in the coaxial structure. So a mode conversion from rectangular TE_{10} to coaxial TE_{02} is realized. The HFSS simulation of the input coupler, shown in Fig. 2.27, verifies the prediction. The cold-test result (conducted with an additional E-H tuner) is shown in Fig 2.28, and it shows broad bandwidth from 16.6 GHz to 18 GHz with –4 dB reflections, which implies that 60% of the input power is converted into coaxial *TE* mode.

2.4.1.2 Input gyro-TWT section

The coaxial TE_{02} mode at the end of the coupler feeds into the vaned mode-converter/filter structure where it converts to the circular TE_{02} mode. Most non-

axisymmetric circular modes are filtered out because their transverse wavenumbers keep change along the z axis, so no stable interaction can be realized.

The circular mode TE_{02} is excited in the interaction waveguide. Back-to-back TE_{02} to TE_{01} mode-converters are placed downstream to insure a high mode purity, thus the mode competition can be minimized and parasitic oscillation can be eliminated. The radial dimension satisfies the following equation:

$$\frac{\mu_{01}}{\mu_{02}} = \frac{a_{01}}{a_{02}}$$

where a_{01} and a_{02} are the inside diameters of the smooth sections at the right and left ends of the structure, μ_{01} and μ_{02} are the first and second zeroes of $J_0^{'}(\mu) = 0$ and equal to 3.832, and 7.016, respectively. In our new gyro-amplifier, the values of a_{01} and a_{02} are chosen as 22.34 mm and 40.88 mm, respectively. So the cutoff frequencies of TE_{01} and TE_{02} modes are made equal and thus are strongly coupled, which guarantees effective mode conversion. The details of this type of mode converter/filter will be discussed in next chapter. Figure 2.27 shows the HFSS simulation of mode pattern for the input section.

2.4.1.3   Radiation-free drift section

The input gyro-TWT, cluster-cavity buncher, and output gyro-TWT are separated by radiation-free sections, which are   designed to suppress the electromagnetic radiation that is produced in the previous waveguide section and provide significant ballistic bunching of the electron beam. In order to realize the radiation-free condition, the structure is constructed with a series of non-periodically stacked lossy metallic and ceramic washers and two honeycomb absorbers. The grooves are sprayed with *TeNiCrCoAl* alloy. 6.0 mm thick SiC ceramic disks with varied inner
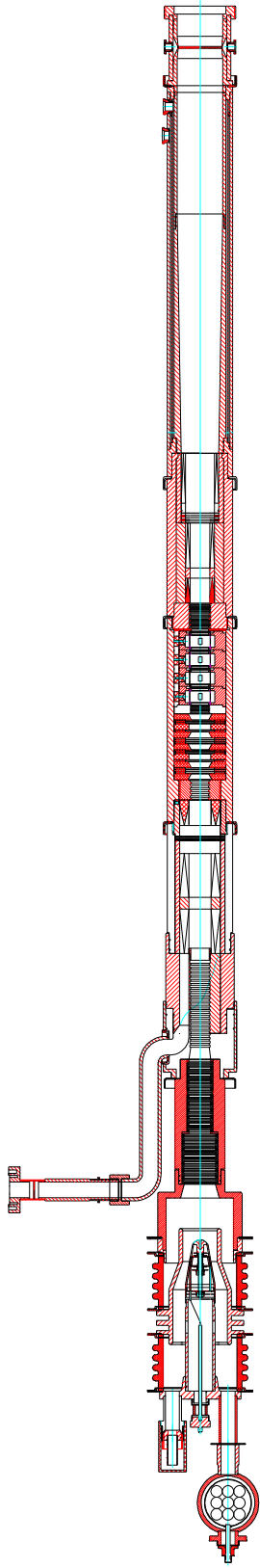
Figure 2. 26 The detailed structure of the new gyro-amplifier.

79
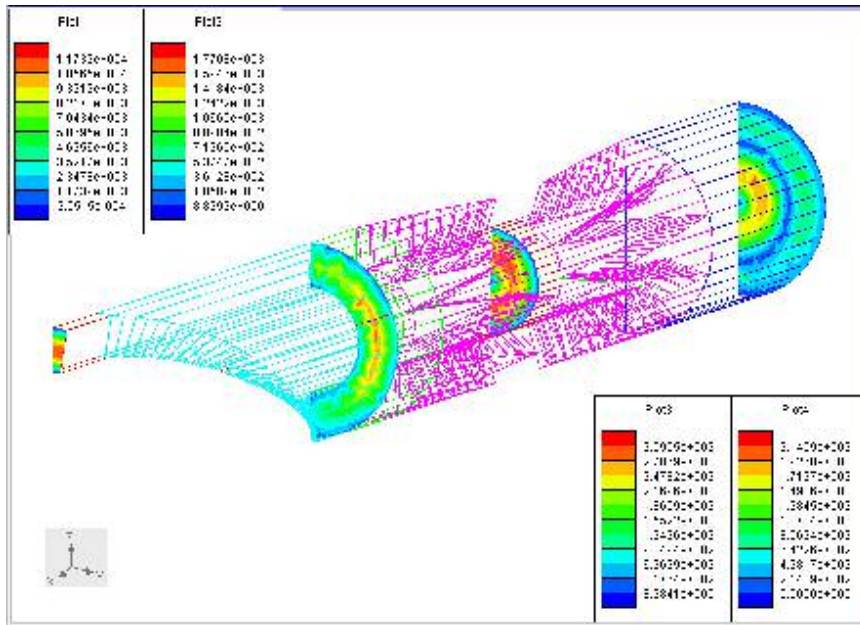
Figure 2. 27 HFSS simulation of the input coupler and gyro-TWT input section.
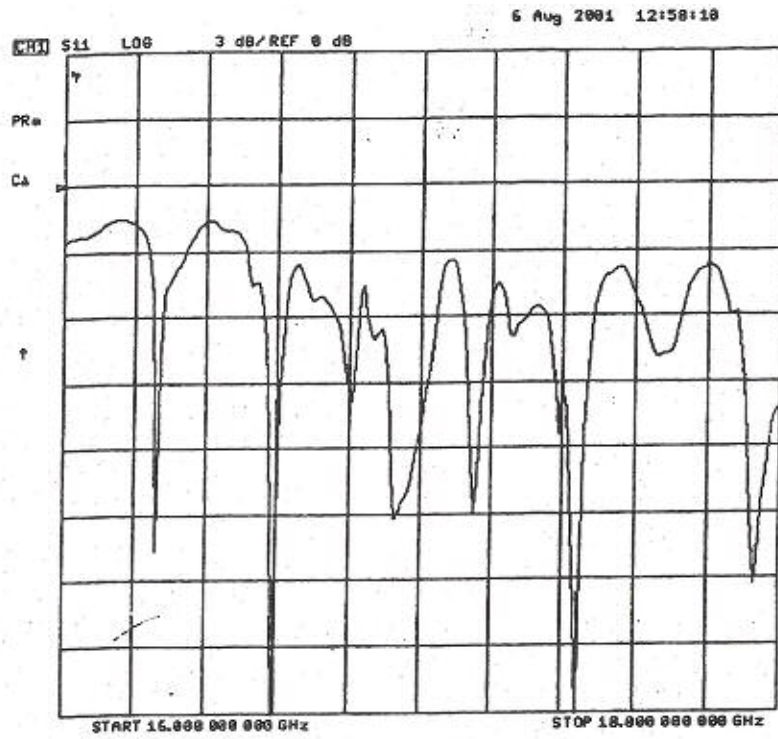
Figure 2. 28 S_{11} parameter of the new gyro-amplifier input coupler, optimized using 2 E-H tuners.

diameters are placed to attenuate non-axisymmetric modes. 2 mm thin metallic disks coated with SiC ceramic washers (0.2 mm thin) inside are also placed to avoid any periodicity. The total length of the first drift section is 11 cm and the minimum inside diameter is 1.75 cm, and the second drift section is 4 cm length and the minimum inside diameter is 1.85 cm. The honeycomb absorbers are placed at the both ends to absorb the waves in the input and output waveguides.

2.4.1.4   Output gyro-TWT section

The beam initially excites a TE_{02} mode when it enters the output section. Similarly, In the output waveguide, the mode converter/ filter with ten gradually tapered slots and vanes arranged periodically around the azimuthal direction has been employed to realize mode conversion from $TE_{02} \rightarrow TE_{03} \rightarrow TE_{04}$. To ensure the mode conversion, the diameters of the internal filter should satisfy the following condition:

$$\frac{\mu_{02}}{\mu_{03}} = \frac{\mu_{03}}{\mu_{04}} = \frac{a_{02}}{a_{03}} = \frac{a_{03}}{a_{04}}$$

where a_{02}, a_{03} and a_{03} are the insider diameters of the smooth sections from left to right, corresponding TE_{02}, TE_{03} and TE_{04} modes. Similarly, μ_{02}, μ_{03} and μ_{04} are the second, third and forth zeroes of $J_0^{'}(\mu) = 0$ and equal to 7.016, 10.175 and 13.324, respectively. The values of a_{02}, a_{03} and a_{03} are 20 mm, 29 mm and 38 mm, respectively. The total length of output waveguide is 20 cm. Figure 2.29 shows the HFSS simulation of mode pattern for the output mode-converter.

Downstream the output waveguide section is the collector of the gyro-TWT which has a taper angle of $2.9°$ in this region. In order to avoid the possibility of the electron beam hitting the output window, the magnitude of magnetic field is dramatically reduced to defocus the beam.
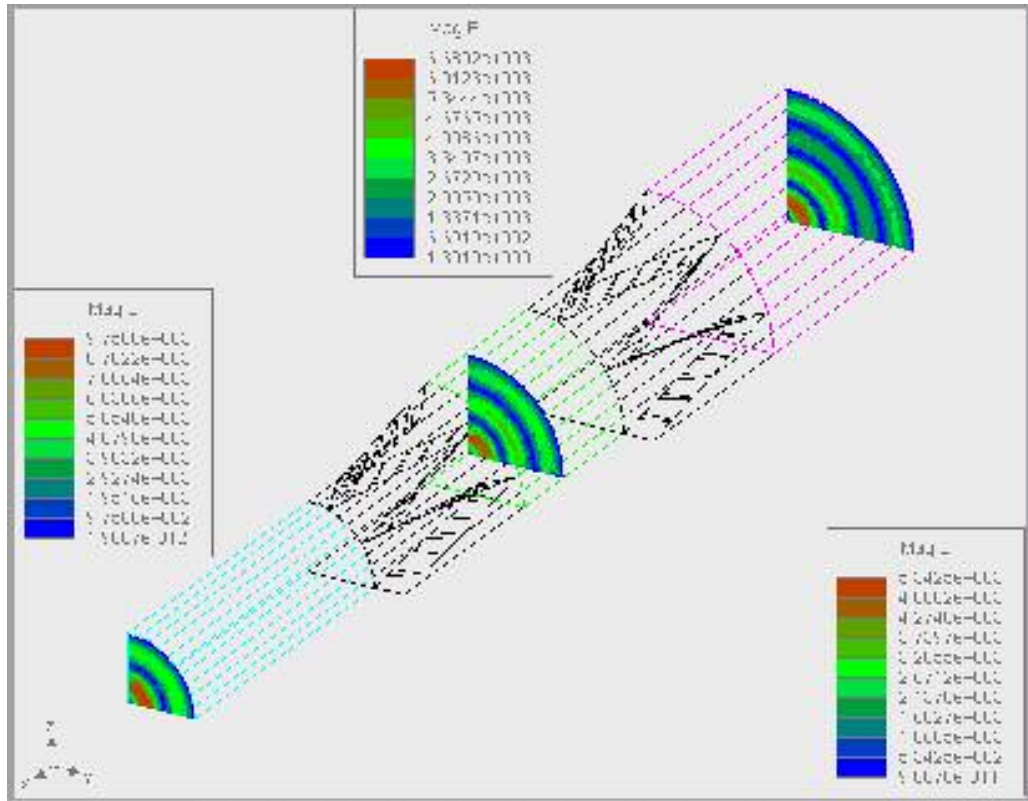
Figure 2. 29 Mode converter/filter chain of TE$_{02}$→ TE$_{03}$→ TE$_{04}$ circular waveguide mode from HFSS simulation. The input mode is TE$_{02}$ mode, and output is TE$_{04}$ mode.

2.4.1.5   Window

The output mode is TE$_{04}$ mode, and correspondingly a high-order mode output window is required. The window is designed by HFSS, as shown in Fig. 2.29. It's similar to a pillbox window, but instead using a step at each side, a gradual down-taper is adopted at both sides.   A high purity alumina (with loss tangent $\delta_l = 0.00095$ disk and relative dielectric constant $\varepsilon_r = 9.0$) is used. The thickness of ceramic disk is about ½ guide wavelength ($\lambda_g / 2$). The design parameters of the window is listed in Fig. 2.30. The frequency response of theTE$_{04}$ mode reflection coefficient S$_{11}$ parameter is plotted in Fig. 2.31. 1.5 GHz of -15 dB and 2.5 GHz of -10 dB bandwidth is achieved, which means 97% and 90%, respectively, power is transmitted.

2.4.2   Experimental results

The gyro-amplifier is powered by a pulse-line modulator (AN/FPS20) to provide a flat 25µs, 10 to 300 Hz repetition rate, and 30 to 70 kV pulsed voltage. A large current switched mode power source (Model 152L) which shortens the charging time of the Pulse Forming Network (PFN) is used to power the modulator.

The gun operating magnetic field is produced by three sets of water cooling coils each powered by a DC power supply and adjusted independently. Four sets of water cooling solenoids are used to provide the main magnetic field for the gyro-amplifier interaction, and are powered separately. Therefore, the magnetic field profile can be adjusted easily to optimize the operation condition of the new gyro-amplifier. The whole magnetic field system is separated from the test panel by fiber and connected with a computer on the test panel through a GPIB (general propose interface bus) board. Using the Hewlett Packet HPVEE code in the computer we can adjust the magnetic field profile easily and accurately. Since fiber is used to separate the
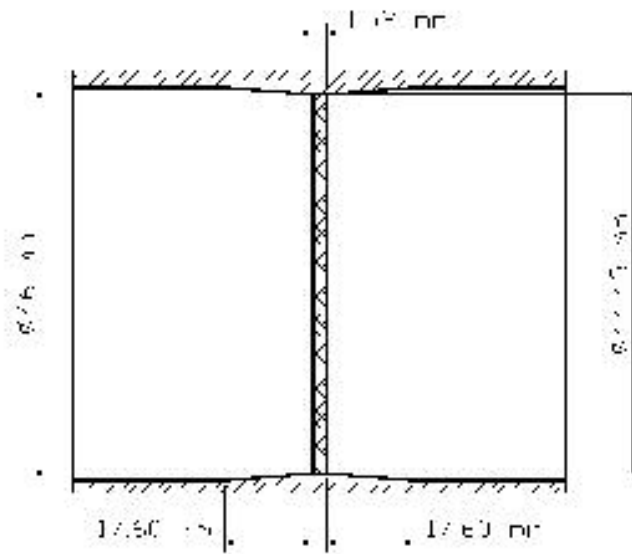
Figure 2. 30 Schematic and dimension of the TE$_{04}$ mode output window.
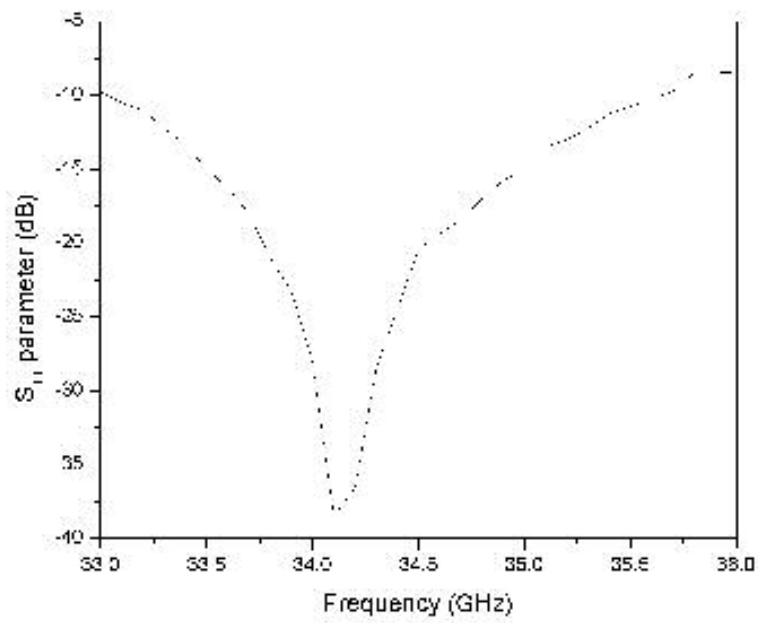
Figure 2. 31 HFSS simulation of the S$_{11}$ parameter for the output window.

magnetic system from the test panel, electrical noise can be removed from the test panel.

The Ku band input signal is provided by a high resolution Agilent 83731B synthesizer with 20 mW unleveled output power. The input is amplified by a Varian pulsed helix TWT (VTU-5192A6), which is rated at 1kW output power over the range of 8-18 GHz, to drive the gyro-amplifier. The Ka band output power of the gyro-amplfier is measured by a calorimetric power meter using a circulated water load. A small portion of phigtron output is sampled though a circular waveguide directional coupler located after the output window of the gyro-amplifier. Accurate measurement of the spectrum is conducted using a spectrum analyzer, Agilent 8564EC. The measurements agree to within 5% (0.2 dB). The phase relation between the Ku band input signal and the Ka band phigtron output radiation is measured using a double balanced mixer. A diode detector is used to observe the output pulse shape when adjustments on the beam voltage, beam current, and magnetic field are optimized. Signals for beam voltage and current are sampled by a diagnostic circuitry and connected to an oscilloscope. All the oscilloscopes in the measurement are connected to the computer through their GPIB sockets. Therefore, the beam voltage, current, RF signal and phase signal waveforms can be inputted to the computer through digital data. By HPVEE code these data are transferred to worksheets of Microsoft Excel. By this way, data acquisition becomes accurate and easy.

During hot-test of the gyro-amplifier, many parameters can be adjusted to get the optimized performance. Some of the adjustable parameter ranges are listed in Table 2.6.

The gyro-amplifier operating parameter and performance are listed in Table 2.7 [71]. With beam voltage 62 kV and current 5.0 A, 80 kW output power, 36 dB gain

and 16 % efficiency at center frequency 33.6 GHz have been achieved. Three 100 MHz bands spaced over 500 MHz have been observed. The drive curve is plotted in Fig. 2.32, which shows the output power, gain and efficiency verses drive power over a 50 dB dynamic range [71]. At small signal region, the gain shows rapid increase, which is consistent with the 2nd harmonic multiplying theoretical model $P_{out} \propto P_{in}^2$ [72].

Table 2. 6 The gyro-amplifier experimental parameter ranges

Beam Voltage	50-70 kV
Beam Current	2.5-20 A
Beam Alpha	1.0-1.5
Input Frequency	16.0-18.0 GHz
Input Power	0-1000 W
Gun Magnetic Field	1.0-1.2 kG
Main Magnetic Field	6.2-6.8 kG
Output Field Taper	0-3% down

Comparing with three-stage phigtron, which has gain of 30 dB and efficiency 35%, and two-stage gyro-TWT with gain of 27 dB and efficiency 12%, the new gyro-amplifier has higher gain of 36 dB and moderate efficiency of 16% with lower beam current 5 A. However, the bandwidth problem needs to be investigated to improve its performance.

2.4.3   MAGY Simulation results

To answer the opening question related to bandwidth of the gyro-amplifier, further studies of the gyro-amplifier have been conducted using the MAGY code
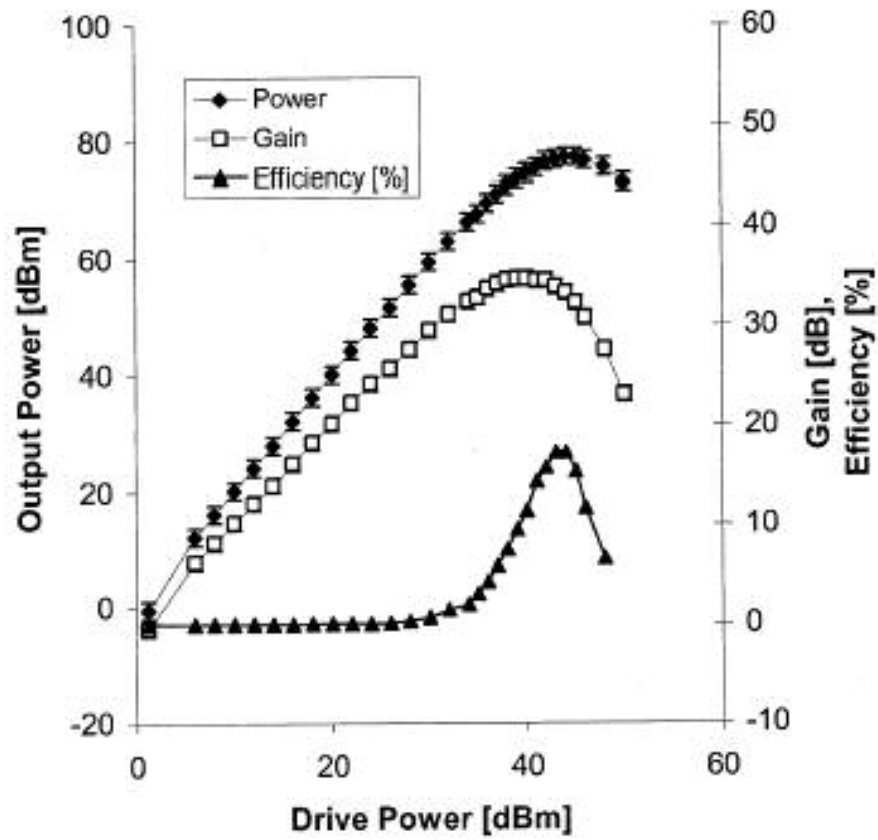
Figure 2. 32 Output power, gain, and efficiency verses input carrier power (by Rodgers et al) [71].

[61], which has been proved to be a very effective tool to interpolate the experiments. The theoretical the numerical studies in Chap. 2.2 provide very good guideline and reference for the new gyro-amplifier studies. The study shows that the bunched second harmonic beam current is proportional to the power lever in the output section. The characteristics of the gyro-amplifier can be understood by studying the source term.

Table 2. 7 Operating parameters and performance of the new gyro-amplifier.

Beam Voltage	62 kV
Beam Current	5.0 A
Input Center Frequency	16.8 GHz
Output Center Frequency	33.6 GHz
P_{out}	80 kW
RF Pulse Width	25 μs
Repetition Frequency	50 Hz
Second Harmonic Efficiency (peak)	16 %
Bandwidth	(3) 100 MHz bands spaced over 500 MHz
Gain (saturated)	36 dB
Mean Phase Deviation	0.5 °

2.4.3.1   Frequency response

Numerical studies of the gyro-amplifier are conducted by inputting the physical and geometric parameters listed in Table 2.8 into MAGY and studying the source term in the second drift space.

Table 2. 8 Physical and geometric parameters of the gyro-device

Electron beam	V = 62 kV, I = 5 A
Input gyro-TWT section	$s = 1$, TE_{01}, TE_{02} modes, length = 10 cm, radius = 11.17, 20.44 cm, B = 6.175 kG
Drift section I	radius = 8.75 mm, length = 11 cm
Clustered Buncher cavity	$s = 2$, TE_{02}, B = 6.6 kG $Q_{ohm1} = 348$, $Q_{ohm2} = 344$, $Q_{ohm3} = 340$, $Q_{ohm4} = 336$ f_{c1} = 34.78 GHz, f_{c2} = 34.38 GHz, f_{c3} = 33.98 GHz, f_{c4} = 33.59 GHz,
Drift section II	radius = 9.25 cm

The frequency response of the field voltage amplitude of the dominant TE_{02} mode of the cluster cavities is depicted in Fig. 2.33. The bandwidth of each cavity is 100 MHz. We notice that the electromagnetic field amplitudes decrease significantly with the increasing of the frequency, and the decreasing rates are 43%, 55% and 66%, respectively, comparing with the adjacent frequency band. The main reason for this phenomenon originates from the finite length of the clustered cavity. As we mentioned before, the length of each cavity is 12 mm and gap between the adjacent cavities is 6.5 mm, so the distance from the center of one cavity to the adjacent one is 18.5 mm. If we compare this length with the drift section lengths 11 cm for the first cavity and 4 cm for the second cavity, 18.5 mm is 17 % of the first one and 46 % of the second. The length of the cavity can't be ignored in this case; moreover, there are four cavities in the cluster. Different cavities see different drift space lengths, as listed in Table 2.9.
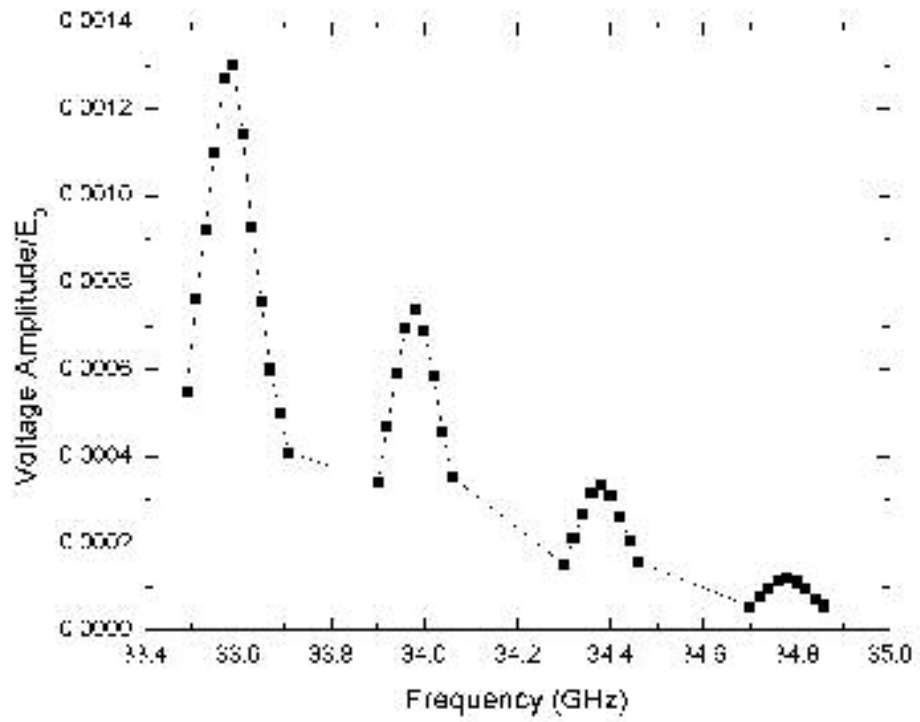
Figure 2. 33 MAGY simulation of the normalized voltage amplitude in the cluster.

Table 2. 9 Drift space lengths for cavities in the cluster.

Cavity No.	Resonant freq.	Drift space I	Drift section II	Ratio*
1	34.78	11 cm	9.4 cm	54 %
2	34.38	12.8 cm	7.6 cm	63 %
3	33.98	14.6 cm	5.8 cm	72 %
4	33.59	16.4 cm	4 cm	81 %

* Ratio = length of drift section I / length of total drift section length

From Eqs. (2.19) and (2.22a), the field amplitudes are proportional to the length of the first drift section length. In this case, the cavities are arranged, for input to output side, with decreasing of cavity resonant frequencies. So cavity 4 sees the longest first drift space, and the field amplitude should be the highest without considering other factors. Moreover, as the frequency increases, the interaction between the beam and wave become weaker. With increasing of resonant frequencies, the interaction points are further away from the cutoff, which means the group velocities become faster, so the interactions get weaker, as a result the field amplitudes are smaller. Those two reasons determine the electrical field amplitude decreasing with increasing of the cavity resonant frequencies.

Figure 2.34 shows the source term (at the end of the second drift space) versus the frequency. Comparing with the field frequency response, we notice that each peak is shifted up in frequency by about 20 MHz relative to the field response, and the first and second peaks are at the same level despite the fact that field amplitudes are different. The cluster-cavity gyroklystron study in Chap. 2.2 demonstrates that in order to have the maximum bunching of the second harmonic, the location of the
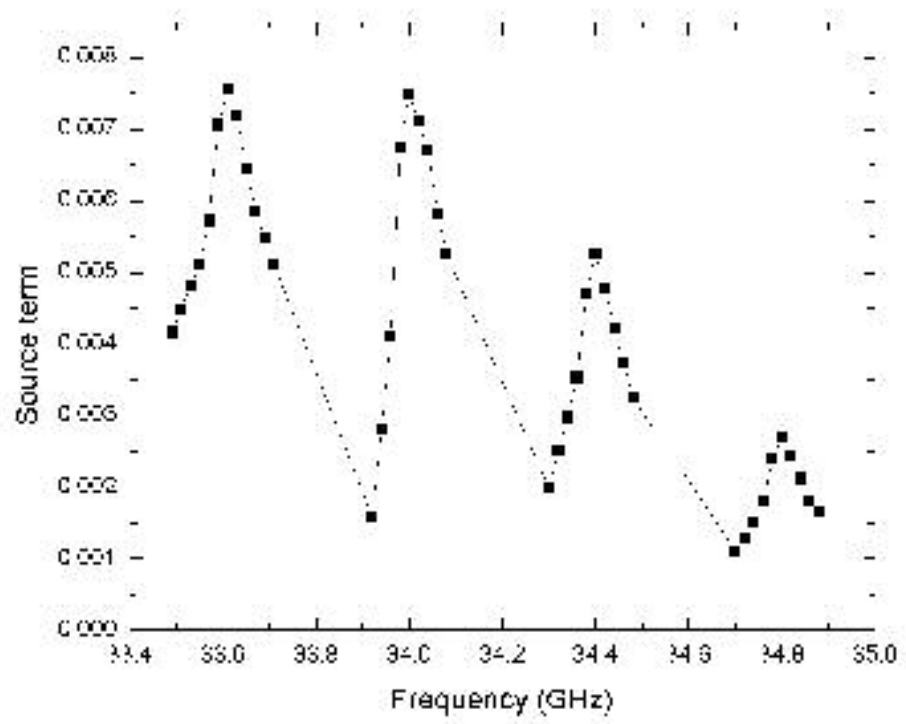
Figure 2. 34 MAGY simulation of the bandwidth of the new gyro-amplifier.

buncher cavity is critical for a given fixed total drift space length. The ratios of drift section lengths for different cavities are listed in Table 2.9. The ratio for the third cavity is close to the optimized value. Not surprisingly, the source term shows a high local maximum. The same reason also explains the lower value of source terms for the other cavities. This can also be used to explain why we couldn't observe all the cluster-cavity frequencies in the experiments.

Chapter 3

Implementation of TE_{0n} Mode-Converter for Gyrotrons in MAGY

3.1 Physical Background and TE_{0n} Mode-Converter Design

3.1.1 Applications of the mode TE_{0n} converter in gyro-amplifiers

As mentioned in the Chap. 1.2, harmonic-multiplying gyro-amplifiers, phigtron [54, 55] and gyro-TWT [42] developed at UMCP have achieved an unprecedented output power in the high-order TE_{03} mode. This is because the mode selective interaction circuits employed in those two gyro-amplifiers effectively suppress spurious competing modes, enabling stable high-order mode operation.

The configuration of the mode selective, harmonic doubling, two-stage gyro-TWT amplifier is shown in Fig.3.1. The input gyro-TWT incorporates a vaned structure which converts the coaxial TE_{02} mode from input coupler into the circular TE_{02} mode. Non-axisymmetric circular modes are suppressed because their transverse wavenumbers are varying along the z axis, and no stable interaction can be realized. Details of the mode converter mechanism will be discussed in the following section. The circular TE_{02} mode is excited in the interaction waveguide.
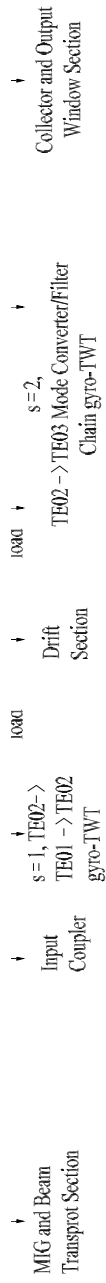
Figure 3. 1 Ka-band two-stage frequency-doubling second-harmonic gyro-TWT amplifier.

MIG and Beam Transprot Section

Input Coupler

s = 1, TE02–⟩ TE01 –⟩ TE02 gyro-TWT

LOAD

Drift Section

LOAD

TE02 –⟩ TE03 Mode Converter/Filter Chain gyro-TWT

s = 2,

Collector and Output Window Section

Back-to-back TE_{02} to TE_{01} mode-pass converter-filters are placed downstream to insure high mode purity, thus the mode competition can be minimized and parasitic oscillation can be eliminated. Details of the mode competition problem are discussed in Chap. 1.3. The radial dimension satisfies the following equation:

$$\frac{\mu_{01}}{\mu_{02}} = \frac{a_0}{b_0}$$

where a_0 and b_0 are the inside diameters of the smooth sections at the right and left ends of the structure, and μ_{01} and μ_{02} are the first and second zeroes of $J_0^{'}(\mu) = 0$ equal to 3.832 and 7.016, respectively. In the harmonic doubling gyro-TWT, the values of a_0 and b_0 are chosen as 22.34 mm and 40.88 mm, respectively. So, the cutoff frequencies of TE_{01} and TE_{02} modes are equal and thus are strongly coupled, which guarantees effective mode conversion.

Similarly, in the output section, the mode converter/ filter with gradually tapered slots and vanes arranged periodically around the azimuthal direction has been employed to realize mode conversion from TE_{02} to TE_{03}. To ensure the mode conversion, the diameters of the internal filter should satisfy the following condition:

$$\frac{\mu_{02}}{\mu_{03}} = \frac{a_0^{'}}{b_0^{'}}$$

where $a_0^{'}$ and $b_0^{'}$ are the insider diameters of the smooth sections at the right and left ends of the structure. Similarly, μ_{02} and μ_{03} are the first and second zeroes of $J_0^{'}(\mu) = 0$ and equal to 7.016 and 10.175, respectively. The values of $a_0^{'}$ and $b_0^{'}$ are 19.50 mm and 28.3 mm, respectively. The total length of output waveguide is 20 cm.

The three-stage phigtron [55], which also deployed a similar TE_{01} and TE_{02} mode converter-chain in the input gyro-TWT section, and $TE_{02} \rightarrow TE_{03}$ mode converter/filter chain in the output structure, has output peak power of 750 kW in the TE_{03} mode.

However, in the experiment of a two-stage harmonic-multiplying phigtron [73], which has a TE_{01} and TE_{02} mode converter-chain in the input gyro-TWT section, and $TE_{02} \rightarrow TE_{03}$ mode converter in the output cavity, the output power in TE_{42} mode was observed when the input drive frequency is below 16.38 GHz, which is cutoff for the designed TE_{0n} modes. That implies that the TE_{0n} mode converter won't have desired performance if the experimental condition is not in favor of the operation of designed TE_{0n} modes.

3.1.2 Design concept of the TE_{0n} mode-converter

A photograph of a $TE_{01} \rightarrow TE_{02} \rightarrow TE_{01}$ converter chain and a schematic of the cross-sectional view of a vaned $TE_{0n} \rightarrow TE_{0m}$ mode converter is shown in Fig. 3.2. The input side of the vaned structure is a smooth-wall waveguide of radius a. This smooth walled structure is gradually transformed into a vaned structure along the axis of the waveguide, as shown in Fig. 3.2. The vane slot opening increases, and it is terminated with a smooth-wall waveguide of radius b. Radii a and b satisfy the following conditions:

$$\frac{\mu_{0n}}{\mu_{0m}} = \frac{a}{b}, \qquad (3.1.1a)$$
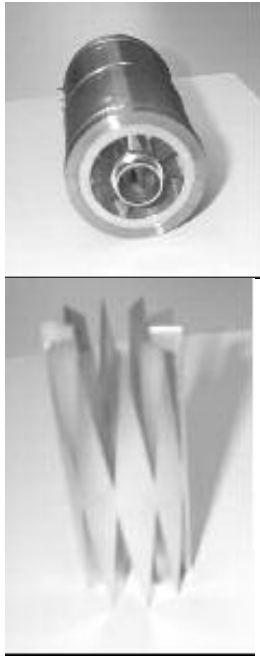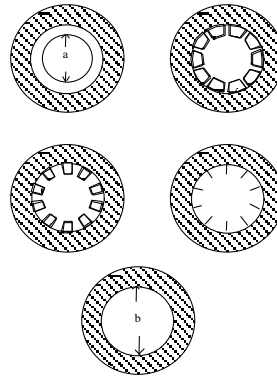
(a)   (b)

Figure 3. 2 (a) A photograph of a $TE_{01} \rightarrow TE_{02} \rightarrow TE_{01}$ converter chain. (b) A schematic of the cross-sectional view of a vaned $TE_{0n} \rightarrow TE_{0m}$ mode converter.

$$J_0^{'}(\mu_{0n}) = J_0^{'}(\mu_{0m}) = 0 \qquad (3.1.1b)$$

where n and m are integers, J_0 is zero-order Bessel function of the first kind, and the prime means derivation. For the designated TE_{0n}, TE_{0m} mode, the cutoff wavenumber k_{c0} is constant along the mode converter axis. However, for the other competing modes, the cutoff wavenumber k_{c0} keeps varying alone the mode-converter axis. So only the designated TE_{0n}, and TE_{0m} modes can realize stable interaction in the converter region, but not the competing mode with varying wavenumber. The mode converter also functions as a mode isolator because with the criterion of Eq. (3.1.1), all pairs of modes, other than the designated TE_{0n} and TE_{0m} mode pair, are suppressed.

3.1.3   Previous study on the TE_{0n} mode-converter

This type of mode converter was employed in a complex open-cavity gyro-oscillator by Guo et al [74], where an analytical theory was proposed and applied to the case of TE_{0n} $\rightarrow$ TE_{0m} mode conversion. A 35 GHz second-harmonic gyromonotron, employing this mode-converter complex cavity with TE_{03} mode output was numerically analyzed and experimentally demonstrated. Power as high as 200 kW and efficiency as high as 30% was obtained. However, in [74], the presence of non-axisymmetric azimuthal modes was ignored. These modes can have significant coupling with the electron beam, which can potentially lead to oscillations or reduce conversion efficiency.

In the present work, we included non-axisymmetric azimuthal modes along with the designated TE_{0n}, TE_{0m} mode, in developing a quasi-analytical theory. We have also incorporated these fields in the MAGY code. With this approach, it is possible to overcome the limitations of the theory developed in [74].

3.2 Quasi-Analytical Theory of the TE_{0n} Mode Converter/Filter

3.2.1   Quasi-analytical theory of TE_{0n} mode-converter

One of the approaches to describe electromagnetic fields in complex waveguides or cavities and their interaction with electron beams is based on the representation of the electromagnetic field as a sum of local eigenfunctions of the structure. This is also the key step in the derivation of the reduced description in MAGY code developed at UMCP [61]. A complete derivation of the generalized telegrapherist's equations used in the MAGY code is presented in ref. [61]. For brevity and clarity of presentation, we review the derivation related to a description of the field in the vaned TE mode converter here.

The starting point is the separation of the electromagnetic field in to a transverse and longitudinal part

$$\boldsymbol{E}(\boldsymbol{r},t) = \text{Re}\{(\boldsymbol{E}_T(\boldsymbol{r},t) + E_z(\boldsymbol{r},t)\hat{z})e^{-i\omega t}\} \qquad (3.2.1a)$$

$$\boldsymbol{B}(\boldsymbol{r},t) = \text{Re}\{(\boldsymbol{B}_T(\boldsymbol{r},t) + B_z(\boldsymbol{r},t)\hat{z})e^{-i\omega t}\} \qquad (3.2.1b)$$

where $\boldsymbol{E}_T$, $\boldsymbol{B}_T$ are complex amplitudes of the transverse fields, E_z, B_z are the longitudinal components, $\hat{z}$ is the unit vector directed along the z axis. The complex

field $\boldsymbol{E}_T$ and $\boldsymbol{B}_T$ vectors as well as E_z and B_z are assumed to be slowly varying functions of time.

The transverse fields are represented as a superpostion of waveguide modes

$$\boldsymbol{E}_T = \sum_k V_k(z,t)\boldsymbol{e}_k(\boldsymbol{r}_T,z) \tag{3.2.2a}$$

$$\boldsymbol{B}_T = \sum_k I_k(z,t)\boldsymbol{b}_k(\boldsymbol{r}_T,z) \tag{3.2.2b}$$

where V_k, I_k are the complex voltage and current amplitudes, and $\boldsymbol{e}_k$, $\boldsymbol{b}_k$ are the eigenvectors. In the MAGY code, the summations in (3.2.2) include both TM and TE modes. But here, to simplify the problem, we only consider TE modes. The eigenfunction of the local transverse cross section for TE modes are introduced as:

$$\boldsymbol{b}_k = \nabla_\perp \Psi_k \tag{3.2.3a}$$

$$\boldsymbol{e}_k = \boldsymbol{b}_k \times \hat{z} \tag{3.2.3b}$$

where

$$\nabla_\perp^2 \Psi + k_c^2 \Psi = 0 \tag{3.2.4a}$$

$$\hat{n} \cdot \nabla \Psi_k \big|_c = 0. \tag{3.2.4b}$$

Here, $\hat{n}$, $\hat{s}$ are the normal and tangential unit vectors (see Fig. 3.3).

The mode converter we are studying is a slotted waveguide with slowly varying slot opening angle from 0 to $2\pi/N$. The cross section view of the regular slotted waveguide with a certain slotting angle $2f_v\pi/N$ is shown in Fig.3.4. The dimensions r_i, r_o are the inner and outer radii of the conducting wall, and $2f_v\pi/N$ is the angle of the opening. The regular slotted waveguide can be divided into two regions: the interaction region (region I, $r \le r_i$) and the vane region (region II, $r_i \le r \le r_o$). The

103
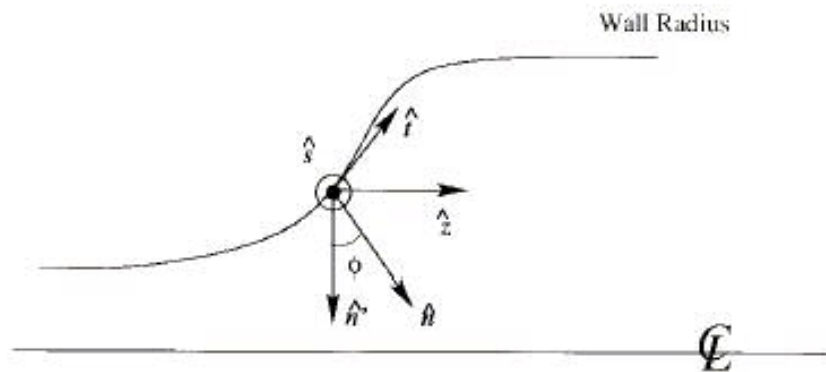
Figure 3. 3 A schematic diagram of the waveguide. The wall radius is a function of the axial position [61].
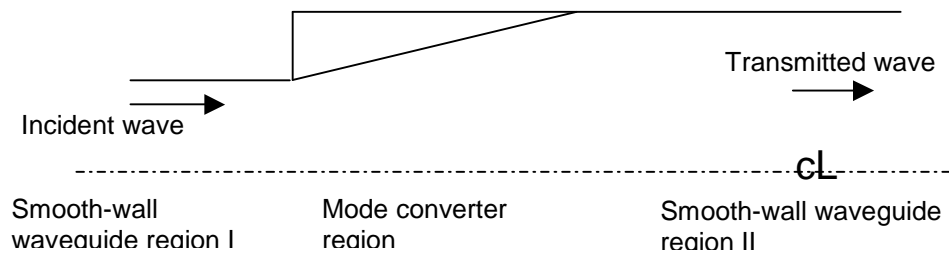
(a)
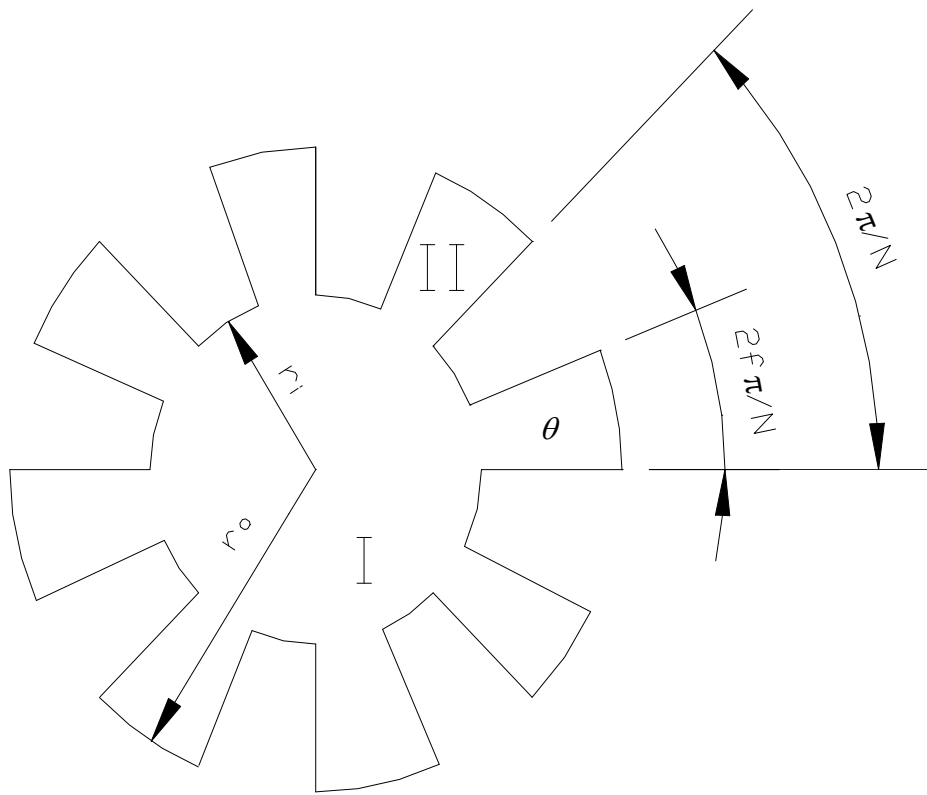
(b)

Figure 3. 4 (a) $TE_{0n} \leftrightarrow TE_{0m}$ mode converter in the form of gradually varying slotted opening waveguide. (b) Cross-section view of regular vaned waveguide with constant slotting angle $2f\pi/N$.

treatment of such a problem should account for the azimuthal periodicity of the structure, and therefore spatial harmonics should be considered inside and outside the slots.

In inner region I, the TE mode fields are given by

$$\Psi_{in} = \sum_p u_p e^{il'\phi} J_{l'}(k_c r) \tag{3.2.5}$$

where J_l is the Bessel functions of the first kind; N is the total number of slots; k_c is the characteristic wavenumber to be determined from the equations; and l is defined as

$$l' = l + pN$$

where l is an integer, and $p = 0, \pm1, \pm2, \ldots$. However, for a sufficiently large number N of slots,

$$l << N \tag{3.2.6}$$

the spatial harmonics up, $p \neq 0$ have sufficiently small amplitudes and can be ignored. Therefore, the field components of a TE mode in region I are those of the usual cylindrical waveguide

$$\Psi_{in} = u e^{il\phi} J_l(k_c r) \tag{3.2.7}$$

Under condition (3.2.6), the electric field in region II is assumed to be only in the azimuthal direction, although the phase can vary from one slot to the next. In vane region II, the TE mode fields are

$$\Psi_v = A[J_0(k_c r) - Y_0(k_c r)R] \tag{3.2.8}$$

where $R = J'_0(k_c r_o)/Y'_0(k_c r_o)$, Y_0 are the Bessel functions of the second kind.

We can apply the continuity of $\partial \Psi / \partial r$ at $r = r_i$

$$\int_0^{2\pi/N} d\phi e^{-il\phi} \partial \Psi_{in} / \partial r = \int_0^{2\pi/N} d\phi e^{-il\phi} u e^{il\phi} J_l^{'}(k_c r_i) =$$

$$\int_0^{2\pi/N} d\phi e^{-il\phi} \partial \Psi_v / \partial r =$$

$$\int_0^{f_v 2\pi/N} d\phi e^{-il\phi} A[J_0^{'}(k_c r_i) - Y_0^{'}(k_c r_i)R] + \int_{f_v 2\pi/N}^{2\pi/N} d\phi[0] =$$

$$\int_0^{f_v 2\pi/N} d\phi e^{-il\phi} A[J_0^{'}(k_c r_i) - Y_0^{'}(k_c r_i)R]$$

(3.2.9)

Rearranging this equation, we get a relation between u and A if R≠0,

$$u = \frac{Ag_l}{J_l^{'}(k_c r_i)} \left[J_0^{'}(k_c r_i) - Y_0^{'}(k_c r_i)R\right],$$

(3.2.10)

where $g_l = \dfrac{N}{2\pi} \int\limits_0^{f_v 2\pi N} d\phi e^{-il\phi}$. If R=0, u = A.

Also, we can use the continuity of Ψ for $\theta < 2 f_v \pi / N$,

$$\int_0^{f_v 2\pi/N} d\phi u e^{il\phi} J_l(k_c r_i) = \int_0^{f_v 2\pi/N} d\phi A[J_0(k_c r_i) - Y_0(k_c r_i)R]$$

(3.2.11)

From Eqs. (3.2.10) and (3.2.11), we can get the dispersion relation

$$\frac{|g_l|^2}{f_v} = \frac{J'_l(k_c r_i)[J_0(k_c r_i) - Y_0(k_c r_i)R]}{J_l(k_c r_i)[J'_0(k_c r_i) - Y'_0(k_c r_i)R]}.$$

(3.2.12)

The cut-off wavenumber k_c is obtained by solving the dispersion relation above.

The eigenfunctions are orthogonal and satisfy the following condition at each axial position

$$\int |e_l|^2 da = k_c^2 \int |\Psi|^2 da = k_c^2 \int_0^{r_i} |\Psi_{in}|^2 da + k_c^2 f_v \int_{r_i}^{r_o} |\Psi_v|^2 da = 1$$

(3.2.13)

Integrating equation (3.2.13) numerically using (3.2.7), (3.2.8) and (3.2.10), the constants A and u can be obtained.

3.2.2 The cutoff wavenumbers from theory

By solving Eq. (3.2.12), the characteristic cutoff wavenumber of the lancher modes in the mode converter can be obtained. Figure 3.5 shows the cut-off wavenumbers for different modes in a $TE_{01} \rightarrow TE_{02}$ mode-converter obtained from our quasi-analytic theory and HFSS simulation. We note that only the desired operating TE_{01} and TE_{02} modes have constant cut-off wavenumbers along the mode converter axis. For other undesired modes, the wavenumbers vary along the mode-converter axis, and this tends to suppress beam interaction with these modes because stable interaction cannot be realized with varying cutoff wavenumbers. We can easily understand this phenomenon by looking at the beam-wave dispersion relation in the mode-converter region, shown Fig 3.6, where the solid line is the designed operating TE_{0n} mode (for the present case, TE_{01} and TE_{02} modes) and the dashed lines are the competing modes. We notice that the competing mode dispersion curve gradually moves up the abscissa as the modes propagate along the axis, so either the absolute instability (point 1) or the convective instability (point 2) are affected. In this way the competing modes are suppressed. As we know, for a gyrotron operated in TE_{0n} modes, the most dangerous competing modes are TE_{2n} modes, because the cutoff wavenumbers of those two types of modes are close to each other. However, in the $TE_{01} \rightarrow TE_{02}$ mode converter region, the cutoff wavenumber for the TE_{21} mode changes from 3.05 to 3.48, which is very significant. The first vane mode in the Fig 3.5 corresponds to the cutoff wavenumber for the TE_{01} mode in the smooth-wave waveguide (region II), and the field for this mode will gradually concentrate in
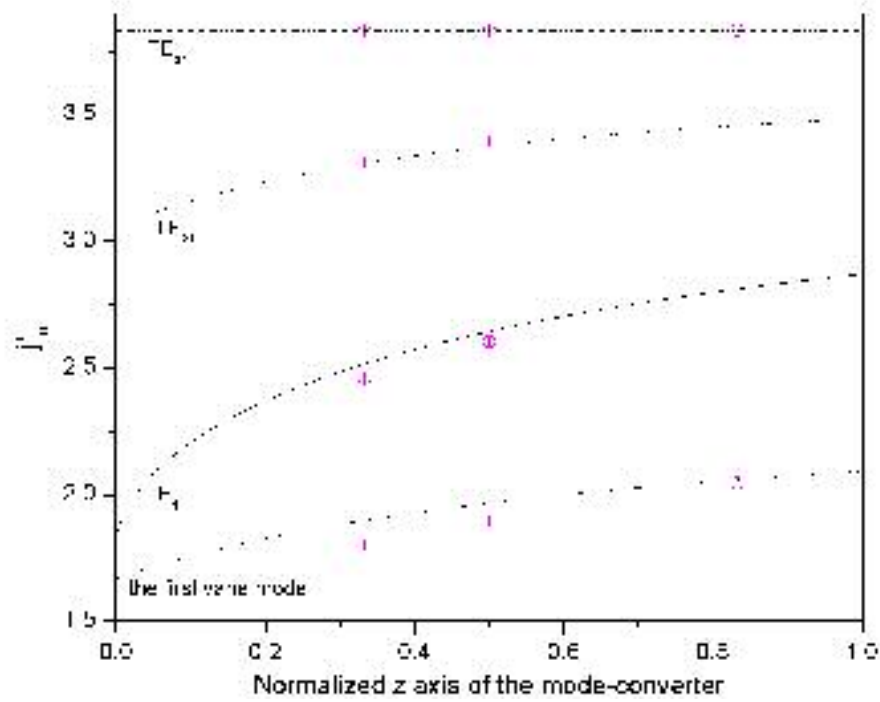
Figure 3. 5 The cut-off wavenumbers for different modes in a $TE_{01} \rightarrow TE_{02}$ mode-converter. The lines are results from the quasi-analytic theory, and the circles are simulation results from HFSS code.
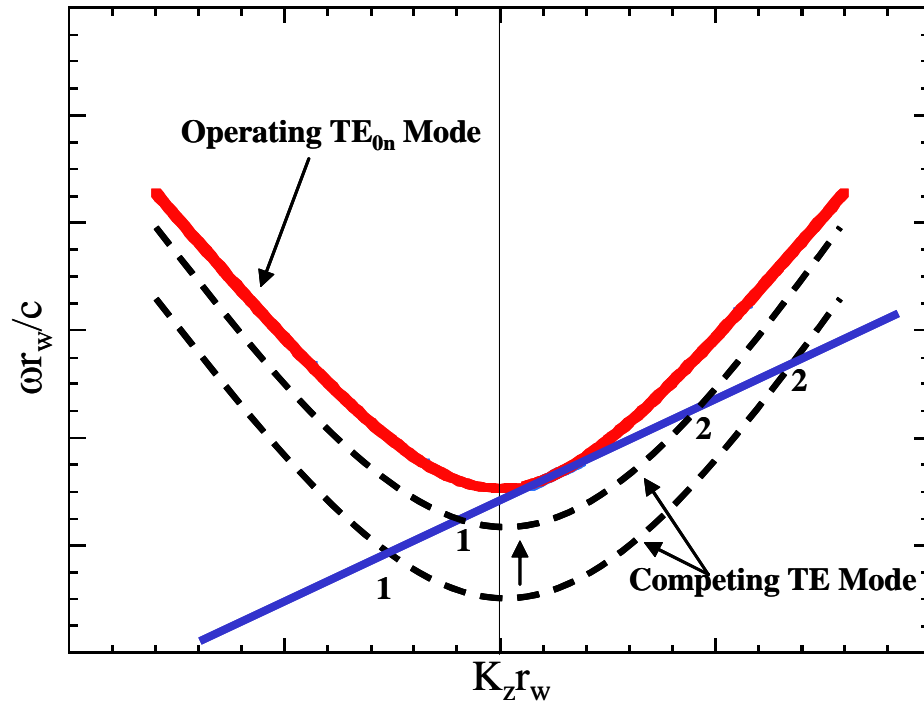
Figure 3. 6 Dispersion diagram of the interaction in a TE_{0n} mode converter. The solid line represents the operating TE_{0n} mode, and dash lines represent the competing TE modes.

the vane region II (refer to fig. 3.4). Since only the field in the region I will interact with the electron beam, this mode can be ignored.
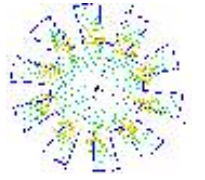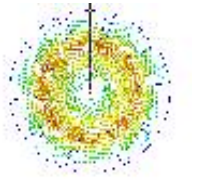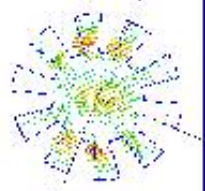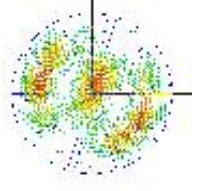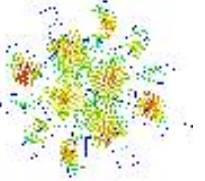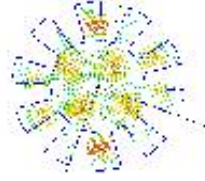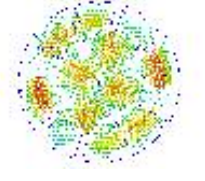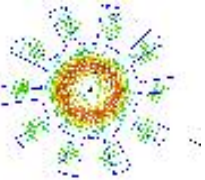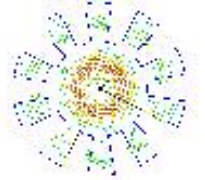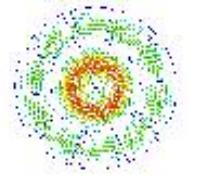
3.2.3   Comparing the results from theory and HFSS

Simulations with HFSS (High Frequency Structure Simulation), a finite element electromagnetic code that calculates field distributions and S parameters for passive three-dimensional (3-D) structures, were conducted to compare with our theory.

As we mentioned before, this kind of mode-converter is essentially a waveguide with a slowly varying slot opening. We may divide it into an infinite number of segments along its axis with length of Δz. As $\Delta z \rightarrow 0$, the field structure of each segment waveguide can be represented by that of a regular slotted waveguide. According to this, in HFSS, we set up an rf structure, which is a piece of waveguide with a slotted opening, with the cross-section as fig. 3.4 b, and the thickness of the structure is small ($\ll$ wavelength). The magnetic field is assumed to be perpendicular at the two cross-section surfaces. In this way, only TE eigenmodes can exist in this structure, and the resonance frequency is equivalent to the cutoff frequency of the infinitely long waveguide with the same cross-section. By changing the slot opening angles in the HFSS simulation, we can obtain the cutoff frequency at different axial locations in the mode-converter.

The simulation results for the $TE_{01} \rightarrow TE_{02}$ mode-converter are shown in Table 3.1. The eigenmodes at three different locations are calculated, with f_v equal to 1/3, 1/2, and 2/3, respectively; the mode pattern and the corresponding cutoff

Table 3. 1 Mode patterns and cutoff wavenumbers for a TE$_{01}$ → TE$_{02}$ mode-converter from HFSS simulation.

	$f_v = 1/3$	$f_v = 1/2$	$f_v = 2/3$
The vane mode I			
K_c	1.8014	1.8947	2.0454
TE$_{11}$			
K_c	2.4541	2.6015	2.8167
TE$_{21}$			
K_c	3.3103	3.3945	3.5138
TE$_{01}$			
K_c	3.832	3.832	3.832

wavenumbers are shown in Table 3.1. It is very clear that the addition of the vane structure in the waveguide interrupts the electric mode pattern for the competing modes, and in this way the parasitic modes are suppressed. While for the operating TE_{01}, and TE_{02} modes, with the field node at the edge of the vane region and the electric field perpendicular to the wall in the vane region, the TE_{01}, and TE_{02} modes maintain the integrity of their mode pattern.

We compare the cutoff wavenumbers obtained from our theory and HFSS, in Fig. 3.5. The theory and simulation results agree with each other very well, which proves that our quasi-analytic theory is an accurate and practical method of describing the field in the vane mode converter.

We also apply the analytic theory to the $TE_{02} \rightarrow TE_{03}$ and $TE_{03} \rightarrow TE_{04}$ mode converters. The cutoff wavenumbers for different modes in those two mode-converters are shown in Fig. 3.7, and 3.8, respectively. Similar to the results for the $TE_{01} \rightarrow TE_{02}$ mode converter, the operating TE_{0n} modes keep the cutoff wavenumber constant in the mode-converter, while the parasitic modes have varying cutoff. However, as n becomes larger, the TE_{2n}/TE_{2m} coupling mode is still likely to become a competing mode because the change of cutoff wavenumber is less significant, especially in $TE_{03} \rightarrow TE_{04}$ mode converter.

In multiple-stage gyro-amplifiers with the electron interaction with $TE_{m1,p1}$ mode at the s_1 harmonic in one stage, and with $TE_{m2,p2}$ mode at s_2 harmonic in the other stage, the condition of azimuthal synchronism,

$$s_2 m_1 = s_1 m_2 \qquad (3.2.12)$$
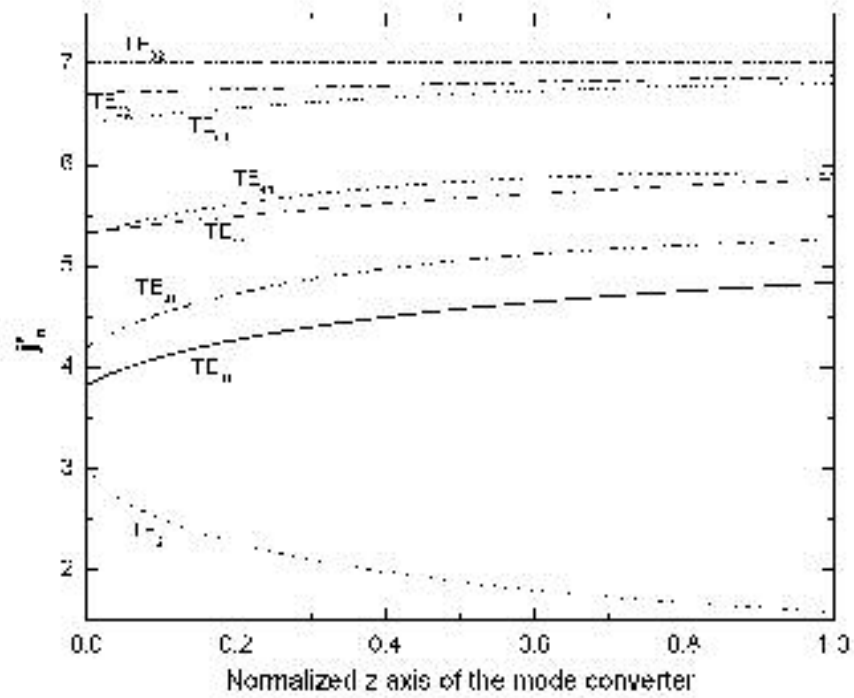
Figure 3. 7 The cut-off wavenumbers for different modes in a TE$_{02}$ $\rightarrow$ TE$_{03}$ mode-converter from the quasi-analytical theory.
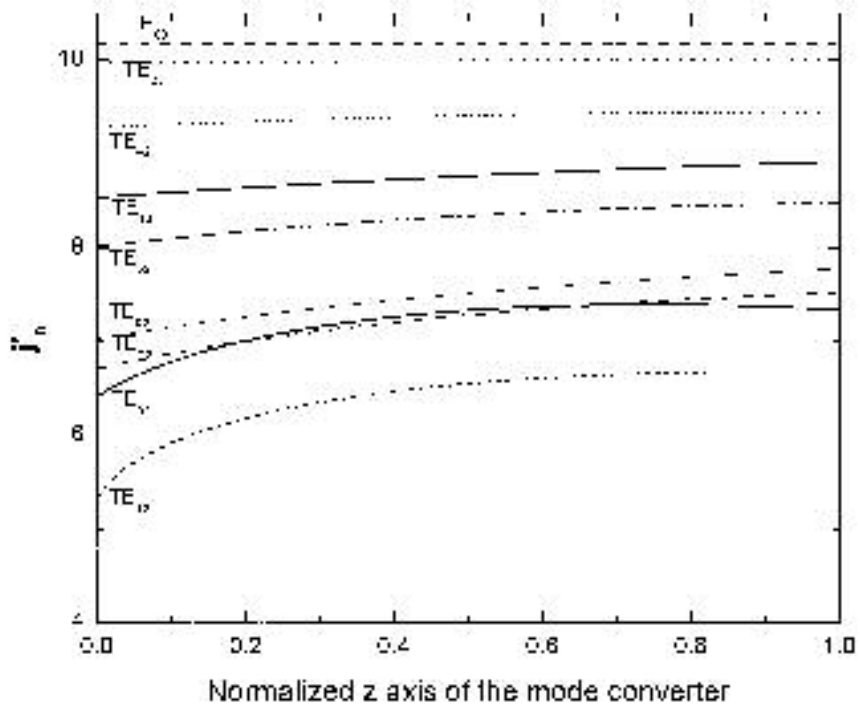
Figure 3. 8 The cut-off wavenumbers for different modes in a TE$_{03}$ → TE$_{04}$ mode-converter from the quasi-analytical theory.

applies [75]. In our case, with TE_{0n} as the operating mode, if a lower order mode-converter, such as $TE_{01} \rightarrow TE_{02}$ mode converter, is applied in the first stage, from pervious analysis, parasitic modes can successfully be suppressed. The electron beam is modulated by the $TE_{0,p1}$ mode in the input stage. At the output stage, from Eq. (3.2.12) only the $TE_{0,p2}$ mode can be amplified. Other modes with $m_2 \neq 0$ can't be amplified because their indexes don't satisfy Eq. (3.2.12). So, in the output the mode competition problem is less severe, and by applying a higher order mode-converter, both mode purity and high power capability can be achieved, which has been proven experimentally in the harmonic-multiplying gyro-TWT and phigtron. Both devices have $TE_{01} \rightarrow TE_{02}$ mode converter in the input stage, and $TE_{02} \rightarrow TE_{03}$ mode converter in the output stage [54, 42].

3.3 Applying the Quasi-Analytical Theory of TE_{0n} Mode Converter/Filter to MAGY

3.3.1   Coupling matrix and Jump matrix in the MAGY algorithm

First, we continue our description of the Telegraphist's equations from the previous section. For details of the derivations refer to [61].

Substituting Eq. 3.2.1 into Maxwell's equations, we obtain the governing equations for the transverse fields [61]

$$\frac{\partial \boldsymbol{E}_T}{\partial z} = ik_0 \boldsymbol{B}_T \times \hat{z} + \nabla_T E_z \tag{3.3.1a}$$

$$\frac{\partial \boldsymbol{B}_T}{\partial z} = ik_0 \hat{z} \times \boldsymbol{E}_T + \nabla_T B_z - \frac{4\pi}{c}(\hat{z} \times \boldsymbol{J}_T) \tag{3.3.1b}$$

and for the longitudinal components

$$E_z = -\frac{1}{ik_0}\nabla_T \cdot (\boldsymbol{B}_T \times \hat{z}) + \frac{4\pi}{i\omega}J_z \qquad (3.3.2a)$$

$$B_z = -\frac{1}{ik_0}\nabla_T \cdot (\hat{z} \times \boldsymbol{E}_T) \qquad (3.3.2b)$$

where ∇_T is the transverse derivative operator, and $\boldsymbol{J}_T$, J_z are the transverse and longitudinal components of the current source, respectively.

The transverse fields can be represented as a superposition of waveguide modes

$$\boldsymbol{E}_T = \sum_k V_k(z,t)\hat{\boldsymbol{e}}_k(r_T,z) \qquad (3.3.3a)$$

$$\boldsymbol{B}_T = \sum_k I_k(z,t)\hat{\boldsymbol{b}}_k(r_T,z) \qquad (3.3.3b)$$

where V_k, I_k are the complex voltage and current amplitudes, and $\boldsymbol{e}_k$, $\boldsymbol{b}_k$ are the eigenvectors. The eigenfunctions of the local transverse cross section are introduced as follows:

$$b_k = \nabla_\perp \Psi_k, \qquad (3.3.4a)$$

$$\boldsymbol{b}_k = \hat{z} \times \boldsymbol{e}_k \qquad (3.3.4b)$$

where

$$\Delta\Psi_k + k_k^2\Psi_k = 0, \qquad (3.3.5a)$$

$$n \cdot \nabla\Psi_k |_{onS} = 0 \qquad (3.3.5b)$$

describing TE modes. Note that they can be a function of the axial position as the waveguide geometry changes. In most cases, the change is due to the variations in the wall radius, namely tapering or discontinuities. Here, we discuss a more complex case, changing in cross sections. Nevertheless, the eigenfunctions are orthonormal and satisfy at each axial position

$$\int e_k^* \cdot e_l \, da = \delta_{kl} \qquad (3.3.6a)$$

where * represents for the complex conjugate.

We substitute Eq. (3.2.3) into Maxwell's equations (3.3.1) and (3.3.2), and apply the orthonormality of the eigenfunctions (3.3.6). We can recover at subsequent times the results for slow time variation of the amplitudes by replacing ik_0 with $ik_0 + \partial/c\partial t$. With the approximation slowly varying amplitude, we obtain the generalized telegraphist's equations for the TE modes

$$\frac{2}{c}\frac{\partial V_k}{\partial t} = \Gamma_k V_k - \frac{\partial I_K}{\partial z} - K_{kl}I_l - L_{kl}^V V_l - S_{Tk} \qquad (3.3.7a)$$

$$ik_0 I_k = \frac{\partial V_k}{\partial z} - K_{kl}V_l + L_{kl}^I I_l \qquad (3.3.7b)$$

where

$$\Gamma_k = i\frac{\omega}{c}(1 - \frac{k_k^2}{k_0^2}) \qquad (3.3.8)$$

is the longitudinal wavenumber for the kth mode. Here, we use the summation convention and sum over repeated indices.

Coefficients such as, K_{kl}, $L_{kl}^{I,V}$, and S_{Tk} describe the three different mode coupling mechanisms. First is the coupling term is due to the geometry,

$$K_{kl} = \int e_l \cdot \frac{\partial e_k^*}{\partial z} da \qquad (3.3.9)$$

The second term $L_{kl}^{I,V}$ represents coupling, due to the finite conductivity of the metallic wall, and S_{Tk} describes the coupling through the current sources (electron beam).

In the original version of MAGY, only radially symmetric devices can be simulated, so the coupling matrix K_{kl} results only from the variation wall radius. Here, we briefly review the treatment of discontinuities in wall radius in the code. It seems that the Eq. (3.3.7) and the coupling matrix (3.3.9) can correctly describe the electromagnetic field at the points where the radius changes abruptly. However, at such points, the coupling matrix will behave like a "delta" function and as a result

the voltages and currents from (3.3.7) will suffer discrete jumps with axial coordinate at those points. To insure that the jumps in voltages and currents are correct, in MAGY, we adopt the mode-matching transformation matrices at those discontinuities. Namely, the coupling matrix is replaced by a jump matrix, obtained using a CASCADE-like formulation for the jump discontinuities. It has been shown that this method works very well for gyrotron cavities [61]. Here, we briefly outline the derivation of calculating of the jump matrices by the mode-matching technique.

Starting with a simple discontinuity, referring to Fig. 3.9, we can rewrite Eq. (3.3.3), the transverse fields represented as superposition of waveguide modes, with different indices in region 1 and 2 for clarity. In region 1, we have

$$\boldsymbol{E}_T = \sum_{i1} V_{i1}(z,t)\hat{\boldsymbol{e}}_{i1}(r_T,z) \tag{3.3.10a}$$

$$\boldsymbol{B}_T = \sum_{k1} I_{k1}(z,t)\hat{\boldsymbol{b}}_{k1}(r_T,z). \tag{3.3.10b}$$

In region 2, the E and B fields are

$$\boldsymbol{E}_T = \sum_{k2} V_{k2}(z,t)\hat{\boldsymbol{e}}_{k2}(r_T,z) \tag{3.3.11a}$$

$$\boldsymbol{B}_T = \sum_{i2} I_{i2}(z,t)\hat{\boldsymbol{b}}_{i2}(r_T,z). \tag{3.3.11b}$$

where the 1, 2 are the spatial grid indexes, and i, k are mode indexes, referring to Fig. 3.9.

Applying continuity of tangential E and B across the common aperture area and enforcing zero tangential electric field on the wall of the larger guide yields the following relation for field voltage and current

$$V_{k2} = \sum V_{i1}\int_{A1} \boldsymbol{e}_{i1}\,\boldsymbol{e}_{k2}^{*}da \tag{3.3.12a}$$
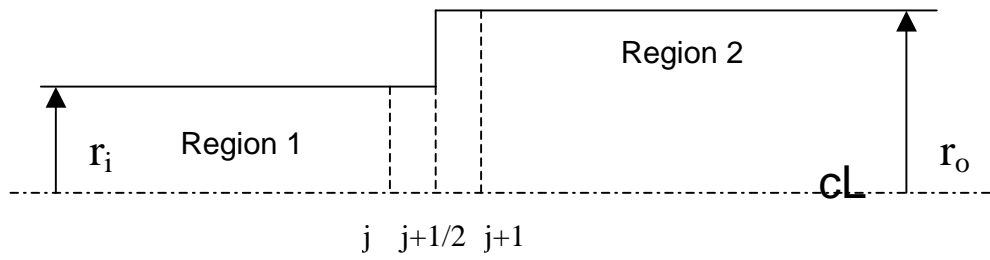
Figure 3. 9 Schematic of a typical discontinuity solving using jump matrices.

$$I_{k1} = \sum I_{i2} \int_{A1} \boldsymbol{b}_{i2} \, \boldsymbol{b}_{k1}^* da \ . \tag{3.3.12b}$$

From Eq. (3.3.4), we have

$$\int_{A1} \boldsymbol{b}_{i2} \cdot \boldsymbol{b}_{k1}^* da = \int_{A1} (\hat{z} \times \boldsymbol{e}_{i2}) \cdot (\hat{z} \times \boldsymbol{e}_{k1}^*) da =$$
$$\int_{A1} [(\hat{z} \times \boldsymbol{e}_{k1}^*) \times \hat{z}] \cdot \boldsymbol{e}_{i2} da = \int_{A1} \boldsymbol{e}_{k1}^* \cdot \boldsymbol{e}_{i2} da \tag{3.3.13}$$

Substituting Eq. (3.3.11) into (3.3.10), we can rewrite the equation as

$$V_{k2} = \sum V_{i1} \int_{A1} \boldsymbol{e}_{i1} \, \boldsymbol{e}_{k2}^* da = J_{ik} \cdot V_{i1} \ , \tag{3.3.14a}$$

$$I_{k1} = \sum I_{i2} \int_{A1} \boldsymbol{e}_{k1}^* \, \boldsymbol{e}_{i2} da = J_{ki}^* \cdot I_{i2} \ , \tag{3.3.14b}$$

where the jump matrix J is defined as

$$J_{ik} = \int_{A1} \boldsymbol{e}_{i1} \, \boldsymbol{e}_{k2}^* da \ , \tag{3.3.15a}$$

$$J_{ki}^* = \int_{A1} \boldsymbol{e}_{k1}^* \, \boldsymbol{e}_{i2} da \ . \tag{3.3.15b}$$

In MAGY, at the discontinuities, the generalized telegraphist's equations for the TE modes can be simplified to be the following

$$\frac{\partial I_K}{\partial z} - K_{kl} I_l = 0 \tag{3.3.16a}$$

$$\frac{\partial V_k}{\partial z} - K_{kl} V_l = 0 \tag{3.3.16b}$$

Other terms are neglected because the K coupling term dominates at the discontinuities.

Equation (3.3.16b) is evaluated in MAGY using

$$\frac{V_{k2} - V_{k1}}{\Delta z} = K_{ik} \frac{V_{i2} + V_{i1}}{2} \ . \tag{3.3.17}$$

Substitute Eq. (3.3.14) into (3.3.17) and using (3.3.15), we have

$$(J_{ik} - I) \cdot V_{i1} = \frac{\Delta z}{2} K_{ik} \cdot (J_{li} + I) \cdot V_{2l} \tag{3.3.18}$$

121

where I is the identity matrix.

If we write Eq. (3.3.18) in matrix form and rearrange it, we obtain the expression for the K matrix

$$\frac{\Delta z}{2} K = (J + I)^{-1} \cdot (J - I) \tag{3.3.19}$$

Here, K, J, and I all represent matrices.

By using Eq. (3.3.4) and (3.3.5), we can evaluate the jump matrix for TE mode by the following equation

$$
\begin{aligned}
J_{ik} &= \int_{A1} \boldsymbol{e}_{i1}\, \boldsymbol{e}_{k2}^{*} da = k_{i1}^{2} \int_{A1} \Psi_{i1} \Psi_{k2}^{*} da = \\
&\quad k_{i1}^{2} \int_{0}^{ri} \Psi_{in,i1} \cdot \Psi_{in,k2}^{*} da + f_{v} k_{i1}^{2} \int_{ri}^{ro} \Psi_{v,i1} \cdot \Psi_{v,k2}^{*} da
\end{aligned}
\tag{3.3.20}
$$

This equation can be integrated numerically.

We use the CASCADE-like method to treat the mode-converter problem in MAGY. The slot opening angle changes by a noninfinitesimal amount from one grid point to the next one

$$\Delta \theta = \frac{\Delta z}{L_{mc}} \cdot \frac{2\pi}{N} \tag{3.3.21}$$

where Δz is the grid size, L_{mc} is the total length of the mode-converter, and N is the vane number of the mode converter. At each grid point, the CASCADE jump matrix will be calculated and converted to the K_{kl} matrix, as shown in Fig. 3.10. In this way, the field amplitude can be correctly obtained.

3.3.2   Comparison of simulation results from MAGY and from HFSS

Using the CASCADE method, we can incorporate the vaned mode-converter into MAGY. Simulations have been conducted with the geometry of the mode-converters
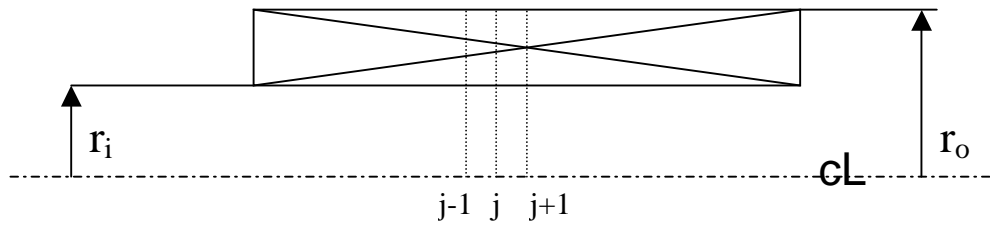
Figure 3. 10 The schematic of mode-converter for jump matrix calculations.

in the two harmonic-multiplying gyro-amplifier mentioned in the previous section, the gyro-TWT and phigtron.

Figure 3.11 shows the transmitted power (S_{21} parameter) in the TE_{01} and TE_{02} modes in a $TE_{01} \rightarrow TE_{02}$ mode-converter when a TE_{01} mode is launched from the left side. Results of MAGY simulations and HFSS simulations are shown. Generally speaking, 90% the transmitted power is in the TE_{02} mode and 10% in the TE_{01} mode. The reflected power is small, more than two-orders of magnitude lower than that of the transmitted power. Some variation in the S-parameters with frequency has been observed (Fig. 3.11). When the frequency is close to cutoff, the transmitted power in the TE_{02} mode tends to decrease, while that in the TE_{01} mode changes in the opposite direction.

The $TE_{02} \rightarrow TE_{03}$ mode-converter demonstrates behavior similar to that of the low-order mode converter, as shown in Fig. 3.12. The transmitted power is distributed in the TE_{01}, TE_{02}, and TE_{03} modes when the input power is in TE_{02} mode. We find that over 90% of the power is in TE_{03} mode, less than 5% is in TE_{01} mode, and less that 3% is in TE_{02} mode. When the frequency is close the cutoff, the power in the desired TE_{03} mode tapers down a little, and the power in low-order TE_{01}, and TE_{02} modes increases. Overall, this type of mode-converter demonstrates promising mode conversion ability.

Excellent agreement between HFSS and MAGY simulation results have been achieved with the discrepancy less than 2%.

3.3.3 Benchmarking the MAGY simulation results with experimental results for the three-stage Phigtron and the new gyro-amplifier

Inputting the parameters listed in Table 3.2, the output power-frequency response and the drive curve of the three-stage phigtron were calculated and compared with
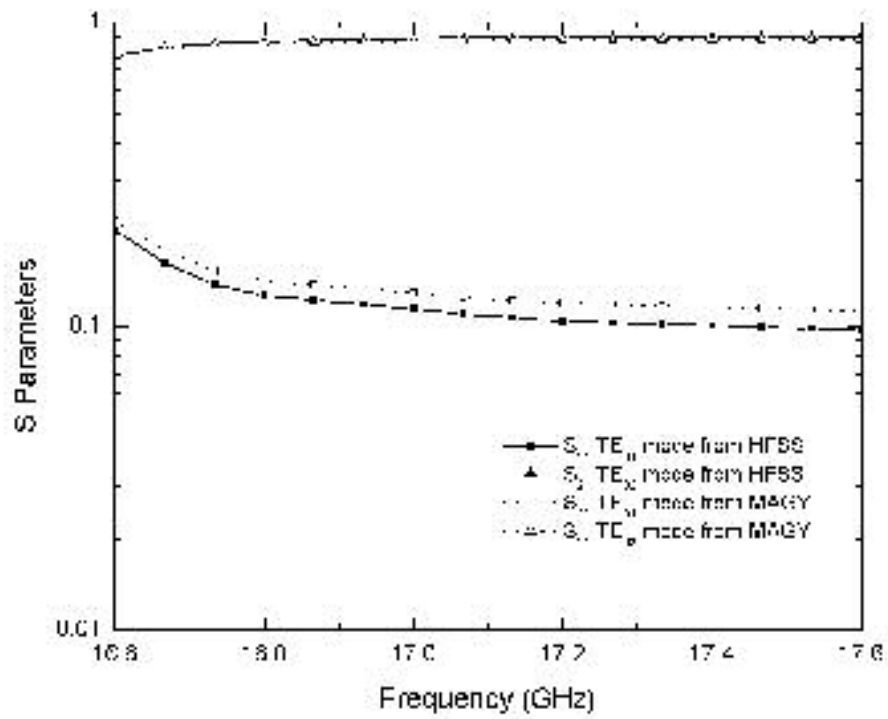
Figure 3. 11 The S parameters from HFSS and MAGY simulation for TE$_{01}$ → TE$_{02}$ mode-converter.
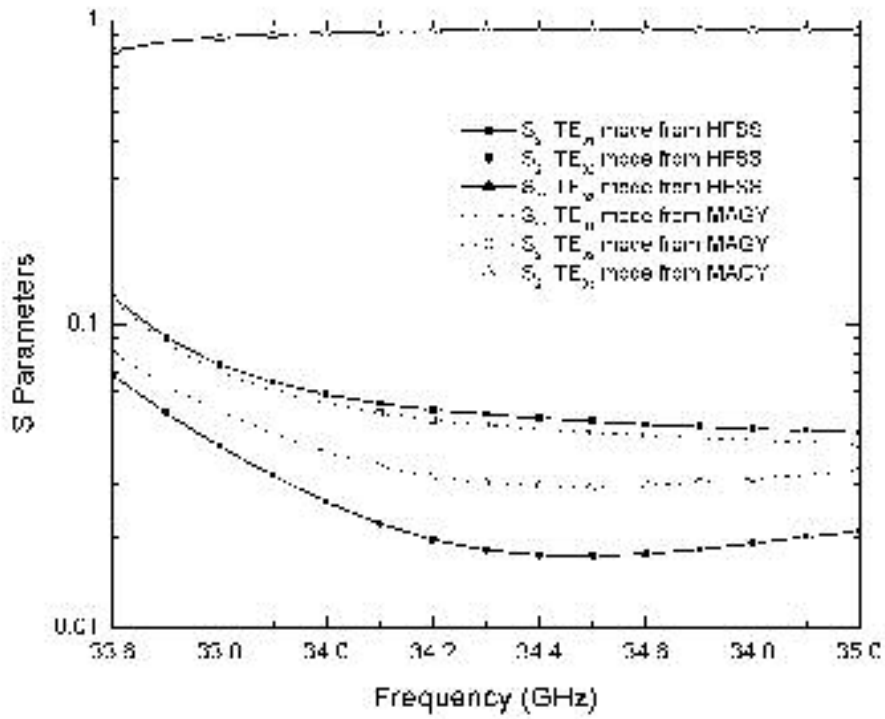
Figure 3. 12 The S parameters from HFSS and MAGY simulation for TE$_{02}$ → TE$_{03}$ mode-converter.

the data measured in corresponding experiments [55] by using the modified MAGY code. The results are shown in Fig. 3.13. From Fig. 3.13a we can see that the highest calculated efficiency of 39% is quite consistent with the highest experimental efficiency of 35% at the same operating frequency of 33.68 GHz. From Fig. 3.13a it also follows that the bandwidth of the device is about 0.3%. Fig.3.13b shows the output power as the functions of the input power P_{in}. The fact that in calculations the gain decreases with P_{in} corresponds to the nonlinear feature of harmonic multiplying gyro-amplifier. In these calculations we set the operating magnetic field $B_0 = 6175$, 6450, and 6400 Gauss for the gyro-TWT section, buncher cavity, and output cavity, respectively. This step-profile distribution of the magnetic field approximates well enough the curved experimental magnetic field profile. The agreement between measured and theoretical amplifier efficiencies is reasonable in light of the assumption of an ideal electron beam. At smaller input signal the calculated gain shows rapid decrease, which is consistent with the 2nd harmonic multiplying theoretical model $P_{out} \propto P_{in}^2$ [72].

Table 3. 2 Physical and and geometrical parameters of the phigtron version II operating at high-efficiency status [55].

Electron beam	V=50 kV, $I_b = 24A$, and $\alpha = v_\perp / v_z = 1.5$
Gyro-TWT	$s = 1$, TE_{02} mode, length=120mm, radius=20.44mm
Drift section I	Length=120mm, radius=8.75mm
Buncher cavity	Q_{ohm}=300,fc=33.9GHz, $s = 2$, TE_{02}, length=15mm, radius=10mm
Drift section II	Length=35mm, radius=9.75mm
Output cavity	Q_{dif}=400,fc=33.68GHz, $s = 2$, TE_{03},length=40mm,radius=14.5mm
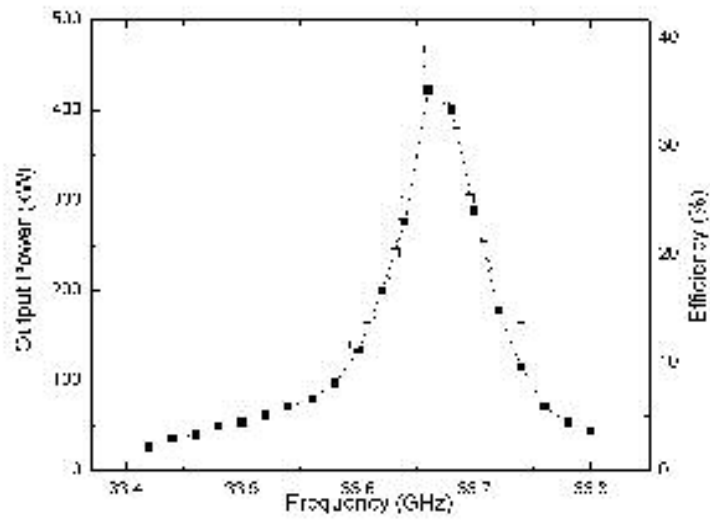
(a)
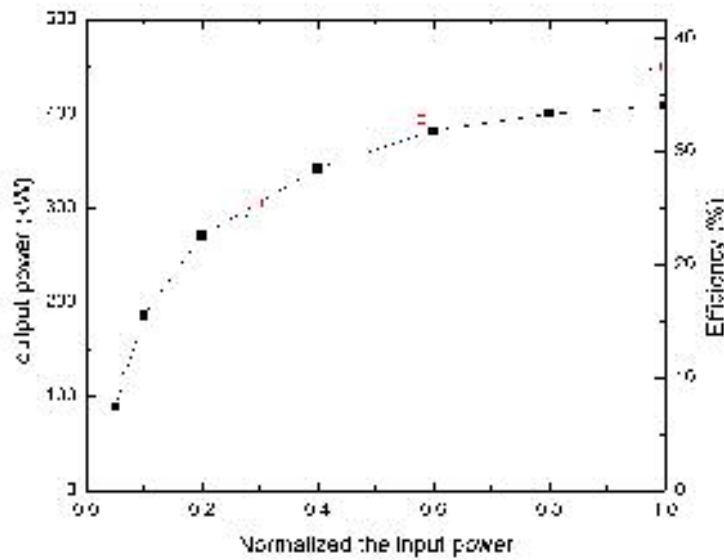
(b)

Figure 3. 13 (a) Dependence of measured and calculated saturated power and efficiency on operation frequency for a fixed beam voltage of 50 kV, and current of 24 A; (b) Experimental and calculated drive curves for beam voltage of 50 kV, current of 24 A and output frequency of 33.68 GHz (Dashed lines are calculated results, and solid lines are experimental results.).

The modified MAGY code is also used for further studying the efficiency, gain, output power and drive characteristics of the new gyro-amplifier. The output section is a TE_{0n} mode converter chain, which consists of a $TE_{02} \rightarrow TE_{03}$ and $TE_{03} \rightarrow TE_{04}$ mode converter. The output gyro-TWT operates at the second harmonic with the output mode in the TE_{04} mode. The length of the structure is 13 cm and magnetic field applied is 6.4 kG. Here, the beam parameters are the same as listed in Table 2.8. Distributed loss is applied in the input section, and strong lossy material is used in the drift spaces.

Figure 3.14a is the drive curve, the output power P_{out} as the function of the input power P_{in}. In the small signal region, the calculated output power is proportional to the square of the input power $P_{out} \propto P_{in}^2$, which is consistent with the 2nd harmonic multiplying theoretical model [72]. Figure 2.14b shows the gain and efficiency as function of input power, which shows that the calculated saturation gain is about 45 dB and saturation efficiency is about 30 %. We have the experimental saturation gain is about 36 dB and efficiency is 16 %. The main reason for this difference is the velocity spread, which has not been considered in our calculation, can decrease the gain. Further numerical simulations show that with 3% velocity spread, the efficiency is down to 16%. The fact that in calculations the gain decreases with P_{in} corresponds to the nonlinear feature of harmonic multiplying gyro-amplifier.

3.4 The Power Capability of the TE_{0n} Mode-Converter

We now address two concerns for implementing the vaned mode-converter in a high power gyrotron. The first is the vacuum breakdown problem. One of the advantages of the gyrotron is high-order mode operation, so the size of the device is large and the breakdown problem is less severe compared with a conventional microwave tube. However, a concern of breakdown in the mode-converter is raised
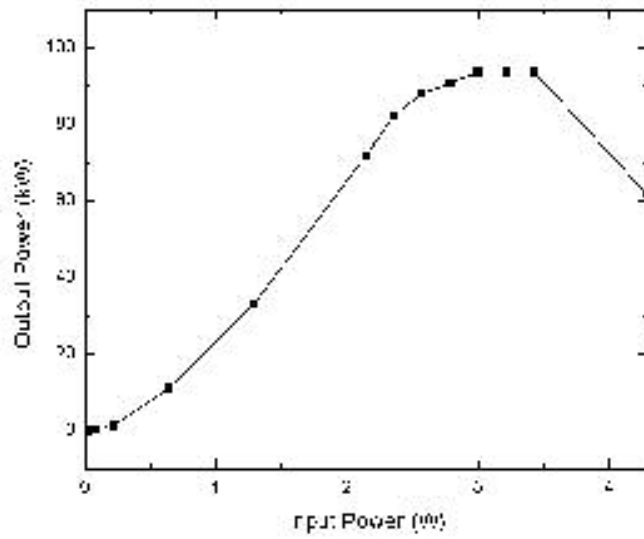
(a)
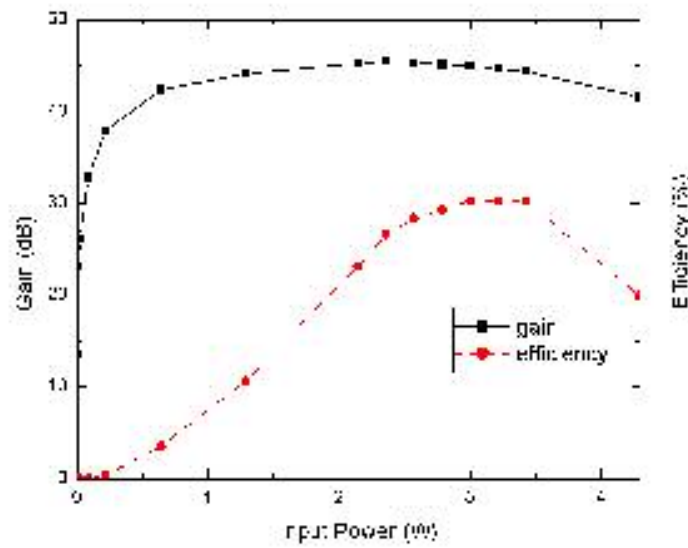
(b)

Figure 3. 14 (a) Simulated drive curve for the new gyro-amplifier from MAGY; (b) Simulated gain and efficiency drive characteristics for MAGY for beam voltage of 62 kV, current of 5 A and output frequency of 33.6 GHz.

130

because the electromagnetic field may be concentrated at the tip of a vane. From the E field plot in Fig. 3.15, we can clearly see that the field has maxima at the vane tip. In vacuum, the field breakdown threshold is $\sim 3 \times 10^5 V/cm$. Using this figure, we find that for a TE$_{01}$ → TE$_{02}$ mode-converter, breakdown occurs when the power level is above 20 MW. It's expected that for a high-order mode-converter, the power capability will be higher.

For the same reason, the high electromagnetic field in the vane tip region, the heat deposited on the surface of the gyrotron may cause cooling problems. The amplitude of the magnetic field on the surface of the mode-converter is shown in Fig. 3.16. Generally speaking, the maximum heat dissipation capability in a vacuum device is $\sim 2kW/cm^2$. It is found using HFSS that the gyrotron power should not exceed 100 MW to remain within the maximum heat dissipation limit. For high-order mode-converter, the threshed power would be higher.

Considering both the breakdown and cooling problem, the power capability of the mode-converter is about 20 MW, which is sufficient for most gyro-amplifier applications.
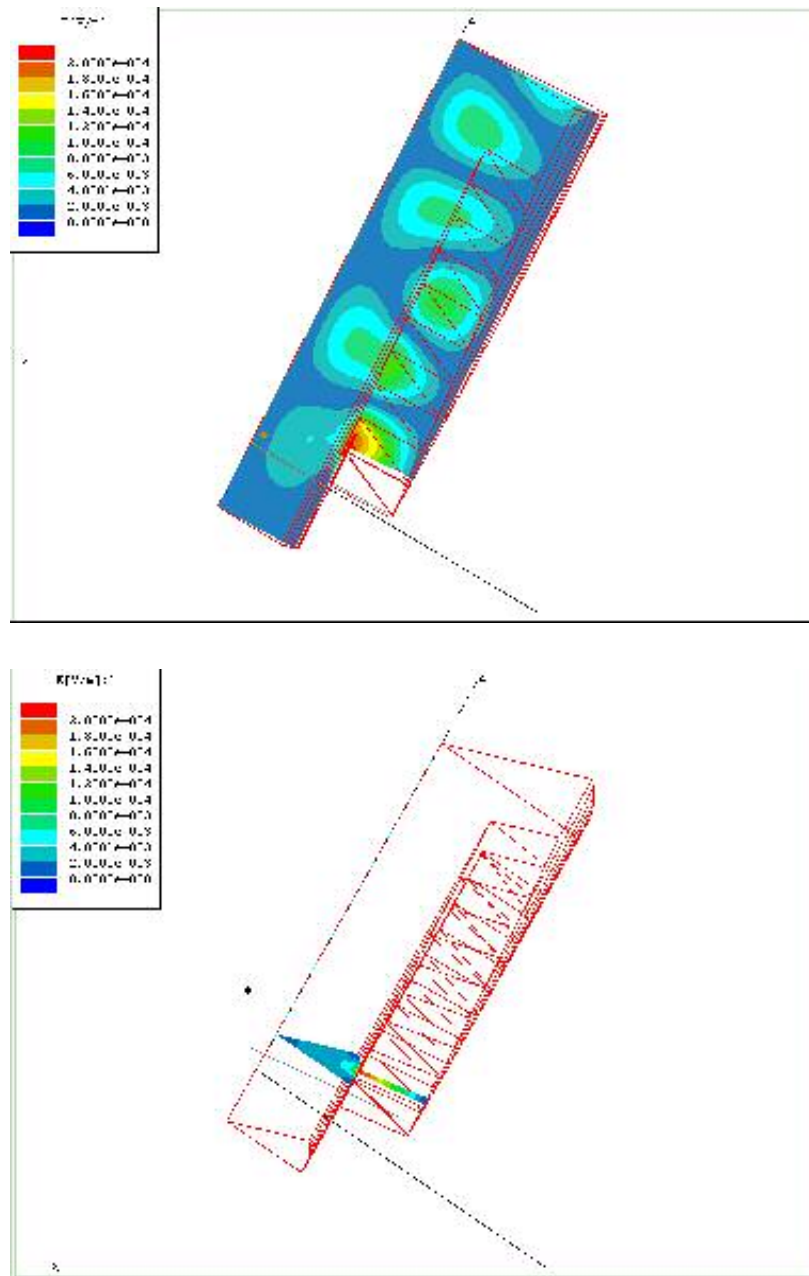
Figure 3. 15 The electric field in the vane region for a $TE_{01} \rightarrow TE_{02}$ mode-converter.
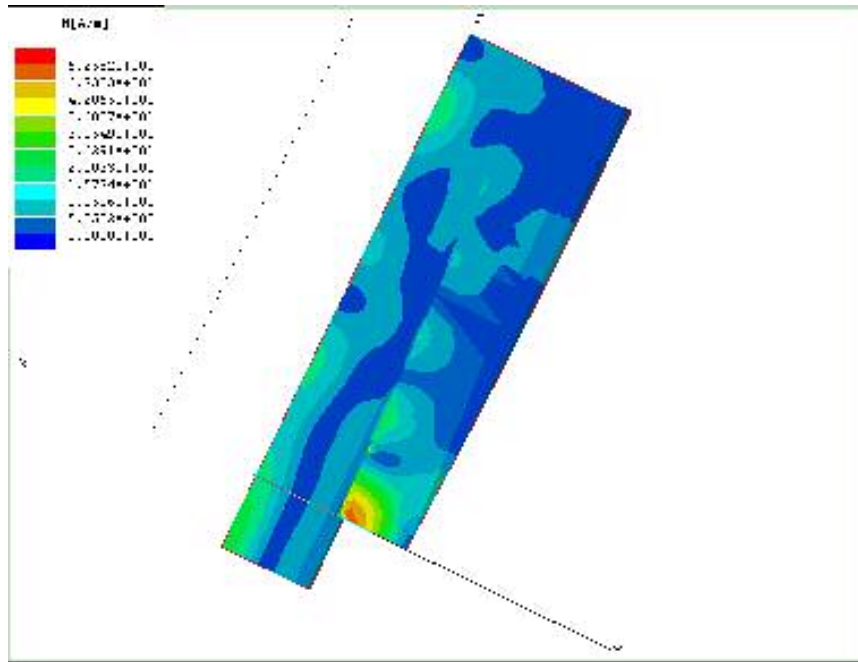
Figure 3. 16 The surface magnetic field for a TE$_{01}$ → TE$_{02}$ mode-converter.

Chapter 4

Summary

An analytical theory of frequency doubling gyroklystrons with cluster-cavity bunchers has been developed with the aim of maximizing the second harmonic current by optimizing the drift section length. MAGY simulations have been conducted to compare with the analytical results and further study the efficiency, bandwidth and output power. The analytical results and MAGY simulations largely agree with each other. In the small signal regime, the bandwidth of the cluster-cavity (with a pair of cavities) is twice that of a single cavity, while both have the same peak bunching. For the case of an amplifier with two-cavity cluster buncher and a gyro-TWT output section, a peak power of 247 kW, efficiency of 24.2% and bandwidth of 1.08% have been calculated. The gain-bandwidth product for this design is 1.1×10^4 dB×MHz, which approximately doubles the single cavity buncher power-bandwidth product. The investigation of the effect of coupling between the cavities of a cluster shows that coupling between the cavities significant lowers the second harmonic bunching strength, so effort has to be made to lower the coupling to an acceptable level. The performance of a three-cavity cluster has also been studied, and still wider bandwidth has been achieved.

A stagger-tuned four-cavity cluster has been designed and tested by the author. In a cold test, more than –30 dB isolation was achieved between adjacent cavities in the cluster. Upon completion of the cold test, the TE clustered cavities were installed in

a new gyro-amplifier tube as a second harmonic buncher cavity and results were reported by Rodgers et al [71, 76, 77]. The device consists of a short Ku-band gyro-TWT input stage to modulate the beam at the $s_1=1$ cyclotron harmonic, the four-unit stagger-tuned clustered-cavity as intermediate stage to bunch the beam at the $s_2=2$ cyclotron harmonic and a Ka-band longer gyro-TWT output stage to extract energy from the bunched beam at the $s_3=2$ cyclotron harmonic. This amplifier achieved 80 kW output power centered at 33.6 GHz with a bandwidth of 0.3 %, efficiency of 16 % and gain of 36 dB in the high order TE_{04} mode [71]. The device did not perform to expectations because parameters such as beam current were not achieved. MAGY simulations have been carried out and compared with the experimental data. The simulations demonstrate that the finite length of the clustered cavities has great influence on the second harmonic bunching current, and it should be taken into account in the design in order to have good performance.

The theoretical study focused on the optimization of a cluster of equal-frequency cavities. It was found that this configuration has the potential to significantly increase the bandwidth of a frequency doubling gyro-amplifier. An appropriate experiment at this point would test this concept. Additional theoretical studies would compare the relative merits of staggered tuned cavities relative to equal frequency cavities. This work will be left future investigations.

In the second part of this dissertation, the mode competition problem and one possible solution, the vaned TE_{0n} mode converter, are studied. The mode converter has been proved to be effective at converting one designated TE_{0n} mode into another designated TE_{0m} mode while suppressing unwanted modes. A quasi-analytical theory

has been developed to describe the electromagnetic field in the mode converter, and eigenmodes have been calculated and compared with HFSS simulations. Excellent agreement has been obtained. By using the CASCADE technique, the nonsymmetric field has been incorporated in MAGY code for the first time. The calculated power from modified MAGY agree with HFSS simulation to 2%. The calculations also show that the TE_{0n} mode converter can be employed in very high power gyro-devices with power capability being limited by breakdown up to 20 MW.

Bibliography

[1].   Victor L. Granatstein and Igor Alexeff, editors, "High-Power Microwave Sources," Artech House, Boston, 1987.

[2].   J. Beiford and J. Swegle, "High-Power Microwave," Artech House, Cambridge, 1987.

[3].   A. S. Gilmour, "Microwave Tubes". Artech House, Inc., copyright 1986.

[4].   Andre V. Gaponov-Grekhov and Victor L. Granatstein, editors, "Applications of High-Power Microwave," Artech House, Boston, 1994.

[5].   A. Straprans, E. W. McCune, and J. A. Ruetz, "High-Power Linear-Beam Tubes," Proc. of IEEE, vol. 61, No. 3, pp. 299-330, March1973.

[6].   C. J. Edgcombe. "Gyrotron Oscillators: Their Principles and Practice," Taylor & Francis Ltd, London, 1993.

[7].   G. S. Nusinovich, T. A. Antonsen Jr., V. L Bratman, and N. S. Ginzburg, "Princeples and capabilities of high-power microwave generators," in Application of High-power Microwave, A. V. Gaponov-Grekhov and V. L. Granatstein, Eds. Norwood, MA: Artech House, 1994, ch. 2, pp. 25-110.

[8].   B. G. James and M. Kreutzer, "High power millitron TWT's in W band," in Conf. Dig. 20th Int. Conf. Infrared and Millimeter Waves, Orlando, Fl, 1995, pp. 13-14.

[9].   R. O. Twiss. "Radiation transfer and the possibility of negative absorption in radio astronomy," Aust. J. Phys., vol. 11, pp567-579, 1958.

[10]. J. Schneider, "Stimulation emission of radiation by relativistic electrons in a magnetic field," Phys. Rev. Lett., vol. 2, pp. 504-505, 1959.

[11]. A. V. Gaponov, "Interaction between irrectilinear electron beams and electromagnetic waves in transmission lines," Izv. VUZov. Radiofiz, vol. 2, pp. 836-837, 1959.

[12]. K. K. Chow and R. H. Pantell, "The cyclotron resonance backward wave oscillator," Proc. IRE, vol. 48, pp. 1865-1870, 1960.

[13]. J. L. Hirshfield and J. M. Wachtell, "Electron cyclotron maser," Phys. Rev. Lett., vol. 12, pp. 533-536, 1964.

[14]. A. V. Gaponov, M. I. Petelin, and V. K. Yulpatov, "The induced radiation of excited classical oscillators and its use in high frequency electronics," Radiophys. Quantum Electron., vol. 10, pp. 794-813, 1967.

[15]. V. L. Granatstein, M. Herndon, R. K. Parker, and P. Sprangle. "Coherent synchrotron radiation from an intense relativistic electron beam," IEEE J. Quantum Electron., vol. QE-10. P. 651, 1974.

[16]. V. L. Granatstein, P. Sprangle, M. Herndon, R. K. Parker, and S. P. Schlesinger, "Microwave amplification with an intense relativistic electron beam," J. Appl. Phys., vol. 46, pp. 3800-3805, 1975.

[17]. V. L. Granatstein, M. Herndon, P. Sprangle, Y. Carmel, and J. A. Nation, "Gigawatt microwave emission from an intense relativistic electron beam," Plasma Phys. Control. Fusion, vol. 17, pp. 23-28, 1975.

[18]. A. V. Gaponov, A. L. Goldenberg, M. I. Petelin, and V. K. Yulpatov, "A device for cm, mm, and submm wave generation," Official Bull. KDIO of SM USSR, np. 11, pp. 200, 1976.

[19]. V. L. Granatstein, Baruch Levush, B. G. Danly, and R. K. Parker, "A Quarter Century of Gyrotron Research and Development," IEEE Trans. Plasma Sci. vol. 25, pp. 1322-1335, Dec. 1997.

[20]. V. V. Alikaev, G. A. Bobrovskii, M. M. Ofitserov, V. I. Poznyak, and K. A. Razumova, "Electron-cyclotron heating on the Tokamok TM-s," JETP Lett., vol. 15, pp27-31, 1972.

[21]. M. E. Read, R. M. Gilgenbach, R. Lucey, K. R. Chu, A. T. Drobot, and V. L. Granatstein, IEEE Trans. Microwave Theory Tech., vol. MTT-28, pp. 875-878, 1980.

[22]. R. M. Gilgenbach, M. E. Read, K. E Hachett, R. Lucey, B. Hui, V. L. Granatstein, and K. R. Chu, et al, Phy. Rev. Lett., vol. 44, pp. 647-650, 1980.

[23]. R. J. Barker, E. Schamiloglu, "High-Power Microwave Sources and Technologies." Chap. 6, Gyrotron Oscillators and Amplifiers. P182-186, 2001.

[24]. V. V. Alikaev, and E. V. Suvorov, "Electron-cyclotron resonance plasma heating and current drive in toroidal devices," in Applications of High Power Microwaves, A. V. Gaponov-Grekhov and V. L. Granatstein, Eds. Boston, MA: Artech House, 1994, pp. 111-114.

[25]. S. Y. Park, R. H. Kyser, C. M. Armstrong, R. K. Parker, and V. L. Granatstein, "Experimental study of a Ka-band gyrotron backward wave oscillator, "IEEE Trans. Plasma Sci., vol. 18, pp. 321-325, 1990.

[26]. M. A. Basten, W. C. Guss, K. E. Kreischer, R. J. Temkin, M. Caplan, and B. Kulke, "Operation of a 140 GHz gyrotron backward wave oscillator," in Proc. 15th Int. Conf. Infrared and Millimeter waves, Orlando, FL, 1990, pp. 575-577.

[27]. H. Liebe, Int. J. Infrared and Millimeter Waves, vol. 10, p. 631, 1989.

[28]. D. R. Lohrmann, "Millimeter wave radars tracking approaching sea-skimming targets," in Proc. 22nd Int. Conf. Infrared and Millimeter Waves, 1997, pp. 39-41.

[29]. R. L'Hermitte, Gerophsical Res. Lett., vol. 14, no. 3, p. 707, 1987.

[30]. W. M. Manheimer, G. Mesyats, and M. I. Petelin, "Applications of high power microwave souces to enhanced radar systems,", in Applications of High-Power Microwaves, A. V. Gaponov-Grekhov and V. L. Granatstein, Eds. Norwood, MA: Artech House, 1994, ch. 5, pp. 169-207.

[31]. A. A. Tolkachev, "Gyroklystron-based 35 GHz radar for observation of space objects," in Proc. 22nd Conf. Infrared and Millimeter Waves, 1997, pp. 37-38.

[32]. M. I. Skolnik, "An introduction to radar," in Radar Handbook, M. I. Skolnik, Ed. New York: McGraw-Hill, 1990, ch. 1.

[33]. J. L. Seftor, V. L. Granatstein, K. R. Chu, P. Sprangle, and M. E. Read, " The electron cyclotron maser as a high power traveling-wave amplifier of millimeter waves," IEEE J. Quantum Electron., vol. QE-15, pp. 848-853, 1979.

[34]. L. R. Barnett, K. R. Chu, J. M. Baird, V. L. Granatstein, and A. T. Drobot, "Gain, saturation, and bandwidth measurements of the NRL gyrotron traveling wave amplifier," in IEDM Tech. Dig., 1979, pp. 164-167.

[35]. K. R. Chu, H. Y. Chen. C. L. Hung, T. H. Chang, L. R. Barnett, S. H. Chen, and T. T. Yang, "Ultra high gain gyrotron traveling wave amplifier," Phys. Rev. Lett., vol. 81, pp. 4760-4763, 1998.

[36]. K. R. Chu, H. Y. Chen. C. L. Hung, T. H. Chang, L. R. Barnett, S. H. Chen, T. T. Yang, and D. Dialetis, "Theory and experiment of ultra high gan gyrotron traveling wave amplifier," IEEE Trans. Plasma Sci., vol. 27, pp. 391-404, 1999.

[37]. Q. S. Wang, D.B. McDermott, and N.C. Luhmann,Jr., "Demonstration of Marginal Stability Theory by a 200kW Second-Harmonic Gyro-TWT Amplifier", Phys. Rev. Lett., vol. 75, pp. 4322-4325, 1995.

[38]. Q. S. Wang, D.B. McDermott, and N.C. Luhmann,Jr., "Operation of a stable 200kW Second-Harmonic Gyro-TWT Amplifier", IEEE Trans. Plasma Sci., vol. 24, pp. 700-706, 1996.

[39]. G. S. Park, S. Y. Park, R. H. Kyser, A. K. Ganguly, and C. M. Armstrong, "Gain broadening in an inhomogeneous gyrotron traveling wave amplifier," in IEDM Tech. Dig., 1991, pp. 779-781

[40]. G. S. Park, S. Y. Park, R. H. Kyser, C. M. Armstrong, A. K. Ganguly, and R. K. Parker, "Broadband operation of a Ka-band tapered gyro-traveling wave amplifier," IEEE Trans. Plasma Sci., vol. 22, pp. 536-543, 1994.

[41]. G. S. Park, J. J. Choi, S. Y. Park, C. M. Armstrong, A. K. Ganguly, R. H. Kyser, and R. K. Parker, "Gain broadening of tow-stage papered gyrotron traveling wave amplifier," Phys. Rev. Lett., vol. 74, p. 2399-2402, 1995.

[42]. H. Guo, Y. Miao et al, "Latest Progress in Studies of Harmonic Multiplying Gyro-Amplifiers", 25th International conference on infrared and millimeter waves conference, TH-F2, Sept, 2000, Beijing, IEEE Press.

[43]. M. Garven, J. P. Calame, B. G. Danly, K. T. Nguyen, B. Levush, F. N. Wood, and D. E. Pershing, "A gyrotron-traveling-wave tube amplifier experiment with a ceramic loaded interaction region," IEEE Trans. Plasma Sci., vol. 30, pp. 885-893, 2002.

[44]. H. R. Jory, F. Friedlander, S. J. Hegji, J. f. Shively, and R. S. Simmons, "Gyrotron for high-power millimeter wave generation," in Proc. Int. Electron Devices Meeting, pp. 234-237, 1977.

[45]. H. R. Jory, "Development of gyrotron power sources in the millimeter wavelength range," in Joint Varenna-Grenoble Int. Symp. Heating in Toroidal Plasma, vol. 2, pp. 351-362, 1978.

[46]. I. I. Antakov, E. V. Zasypkin, E. V. Sokolov, and V. K. Yuplatov, "35 GHz radar gyroklystron," in Proc. 18th Int. Conf. Infrared and Millimeter Waves, Sept. 1993, pp. 386-382.

[47]. E. V. Sokolov, I. G. Gachev, E. V. Zasypkin, and I. I. Antakov, "Experimental study of high-power Ka-band second harmonic gyroklystron amplifier," in Proc. Intense Microwave Pulse III, SPIE 2557, pp. 386-392, 1995.

[48]. I. I. Antakov, E. V. Sokolov, and E. V. Zasypkin, "Design and performance of 94 GHz high power multicavity gyroklystron amplifier," in Proc. Int. Workshop Strong Microwave in Plasmas, pp. 754-758, 1993.

[49]. M. Blank, B. G. Danly, K. T. Nguyen, B. Levush, and D. E. Pershing, "Experimental investigation of W-band (93 GHz) gyroklystron amplifier," IEEE Trans. Plasma Sci., vol. 26, pp. 409-415, 2002.

[50]. M. Blank, K. Felch, B. G. James, P. Borchard, P. Cahalan, T. S. Chu, H. Jory, B. G. Danly, B. Levush, J. P. Calame, K. T. Nguyen and D. E. Pershing, "Development and demonstration of high-average power W-band gyro-amplifiers for radar applications," IEEE Trans. Plasma Sci., vol. 30, pp. 865-875, 2002.

[51]. V. Gregers-Hensen, G. J. Linde, W.-J. Cheung, B. G. Danly, M. T. Ngo, and R. Myers, "WARLOC: A New 94 GHz High-Power Coherent Radar," 2001 NRL Review, Electronics and Electromagnetics, p. 107, 2001.

[52]. P. M. Malouf, V. L. Granatstein, S. Y. Park, G. S. Park, and C. M. Armstrong, "Performance of a wideband, three-stage, mixed geometer gyrotwystron amplifier," IEEE Trans. Electron Devices, Vol. 42, pp. 1681-1685, 1995.

[53]. G. S. Park, P. M. Malouf, V. L. Granatstein, C. M. Armstrong, and A. K. Ganguly. "Realization of improved efficiency in a gyroklystron amplifier," part. Accel., vol. 43, pp. 92-105, 1993.

[54]. H. Guo, J. Rodgers, V. L. Granatstein, G. Nusinovich, M. Walter, and J. Zhao. "Operation of a High Performance, Three Stage, Harmonic-Multiplying Inverted Gyrotwystron," 23rd International Conference on Infrared and Millimeter Waves, Sept. 1998. Univ. of Essex Colchester, Essex, U. K. Conf. Digest, pp. 362.

[55]. J. Zhao, H. Guo, G. S. Nusinovch, J. C. Rodgers, and V. L. Granatstein, "Studies of a Three-Stage Inverted Gyrotwystron", IEEE Trans. Plasma Sci., vol. 28, pp657-664, Jun. 2000.

[56]. Felch, K., B. G. Danly, H.R. Jory, K. E. Kreischer, W. Lawson, B. Levush, and R. J. Temkin. "Characteristics and applications of fast-wave gyrodevices." Proc. IEEE 87, vol. 87, no. 5, pp. 752-781, 1999.

[57]. H. Guo, Y. Miao et al, "Cluster Cavity Gyroklystron and Related Gyro-amplifiers," http://www.glue.umd.edu/~guo/MURIteleconf.htm, MURI'99 teleconference, Mar. 20, 2000.

[58]. R. S. Symons , J. R.M. Vaughan, "The Linear Theory of the Clustered-Cavity TM Klystron," IEEE *Trans. Plasma Sci.* vol. 22, p. 713, 1994.

[59]. K. R. Chu, "Overview of research on the gyrotron traveling-wave amplifier," IEEE *Trans. Plasma Sci.* vol. 30, pp. 903-908, 2002.

[60]. L. R. Barnett, L. H. Chang, H. K. Chen, K. R. Chu, Y. K. Lau, and C. C. Tu, "Absolute instability competition and suppression in millimeter-wave gyrotron traveling-wave tube," Phys. Rev. Lett., vol. 63, p. 1062-1065, 1989.

[61]. M. Botton, T. M. Antonsen, Jr, B. Levush, K. T. Nguyen, and A. N. Vlasov, "MAGY: A Time-Dependent Code for Simulation of Slow and Fast Microwave Sources," *IEEE Trans. Plasma Sci.* vol. 26, p. 882, 1998.

[62]. S. Y. Cai, T. M. Antonsen, Jr, G. Saraph, and B. Levush, "Multifrequnecy theory of high power gyrotron oscillators," Int. J. Electron., vol. 61, pp. 823-854, 1984.

[63]. K. T. Nuyen, B. Laruch, T. M. Antonsen, M. Botton, M. Blank, J. P. Calame, B. G. Danly, "Modeling of gyroklystron with MAGY," *IEEE Trans. Plasma Sci.* vol. 28, pp. 867-886, 2000.

[64]. R. S. Symons, "Broadband klystron cavity arrangement," U.S. Patent # 4,800,322, Jan 24,1989.

[65]. R. S. Symons, B. Arfin, R. E. Boesenberg, P. E. Ferguson, M. Kirshner and J. R. M. Vaughan, "An experimental clustered-cavity klystron," Proceedings of the International electron devices meeting, Washington DC, Dec 1987.

[66]. R. S. Symons, "Scaling lows and power limits for klystrons," Proceeding of the International electron devices meeting, L. A., CA, Dec 1986.

[67]. J. G. Siambis, R.S. Symons, "Ultrawideband clustered-cavity klystron," Ultra-wideband, short-pulse electromagnetics, Edited by H. Bertoni el al., Plenum Press, pp. 121-127, 1993.

[68]. G. S. Nusinovich, T. M. Antonsen, H. Guo, and V. L. Granatstein, "Theory of Clustered-Cavity Gyroklystron," *Phys. Plasmas*, vol. 9, p. 4032, 2002.

[69]. G. S. Nusinovich and O. Dumbrajs, "Two-Harmonic Prebunching of Electrons in Multicavity Gyrodevices," *Phys. Plasmas*, vol. 2, p. 568, 1995.

[70]. Y. Miao, M.S. Thesis, "TE_{0n} Mode Clustered-Cavity for Wideband Gyro-Amplifier," p. 32, ECE Dept., University of Maryland, College Park, 2002.

[71]. J. C. Rodgers, T. M. Antonsen, V. L. Granatstein, "Harmonic gain and noise in a frequency-doubling gyro-amplifier," *IEEE Trans. Elec. Devices,* vol. 50, pp. 1785-1792, 2003.

[72]. D. J. Bates and E. L. Ginzton, "A Traveling-Wave Frequency Multiplier". *Proceedings of the IRE*, pp. 938-944.1957.

[73]. S. Chen, "A two stage, phase-coherent, harmonic-multiplying, inverted gyrotwystron," Ph. D dissertation, University of Maryland, College Park, 1997.

[74]. H. Guo, D. Wu, G. Liu, Y. Miao, S. Qian, and W. Qin, "Special complex open-cavity and low-magnetic-field high-power gyrotron," *IEEE Trans. Plasma Sci.* vol. 18, pp. 326-333, 1990.

[75]. J. L. Hirshfield, "Coherent radiation from spatiotemporaly modelated gyrating electron beams," *Phy. Rev. A* vol. 44, pp. 6845-6853, 1991.

[76]. C.S. Kou, S. H. Chen, L. R. Barnett, H. Y. Chen, and K. R. Chu, **"**Experimental study of an injection-locked gyrotron backward-wave oscillator," *Phy. Rev. Letters*, vol. 70, no. 7, p. 924-7, 1993.

[77]. Hezhong Guo, Yingyu Miao, and et al, "A new triplet gyrotron amplifier". The 3rd IEEE International Vacuum Electronics Conference, 2002.

[78]. Hezhong Guo, Yingyu Miao, and et al, "Initial experimental results of a new triplet harmonic-multiplying gyrotron amplifier," The 27th International Conference on Infrared and Millimeter Waves, 2002.